

ABSTRACT

Title of Thesis: IMMOBILIZED SEED-MEDIATED GROWTH
OF TWO DIMENSIONAL ARRAYS OF
SHAPED METALLIC NANOCRYSTALS

Maria Teresa Perez Cardenas, Doctor of
Philosophy, 2017

Thesis Directed By: Dr. Zhihong Nie, Department of Chemistry and
Biochemistry

Acknowledging that the optical properties of noble metal nanocrystals (NMNCs) are largely determined by their size, composition, and shape, the demand for NMNCs with controlled shapes is expected to increase. To expand the property discovery and application development of polyhedral NMNCs, it is pivotal to understand the key factors involve in the nucleation and growth processes of NMNCs for better control over the crystal facets. Furthermore, to implement polyhedral NMNCs into functional devices for applications in such as chemical sensors, photovoltaics, and catalysis, it is essential to design cost-effective methods to assemble NMNCs into two-dimensional arrays with controlled orientation and particle distance.

This dissertation describes the stability and interaction of molecular species formed during the reduction of gold metal precursor, as well as factors that influence the formation of nanocrystals with different shapes. This study suggests that during

the Au reduction step, an intermediate complex is formed. Over time the complex degrades decreasing the concentration of gold ions and subsequently slowing down or inhibiting the nucleation; thereby, affecting the reproducibility of synthetic methods. These findings will provide guidance for the development of more simple, reliable methods to control the shapes of the nanocrystals. Additionally, I developed an immobilized seed-mediated growth strategy for the fabrication of two-dimensional arrays of mono- and bi-metallic polyhedral nanocrystals with well-defined shapes and orientations on a substrate. This method relies on the controlled solution-phase deposition of gold and palladium metals on a selectively exposed surface of self-assembled seed nanoparticles that are immobilized on a substrate through collapsed polymer brushes. This synthetic approach presents an important addition to current tools for the fabrication of substrate-supported functional nanocrystals as new materials and devices.

IMMOBILIZED SEED-MEDIATED GROWTH OF TWO DIMENSIONAL
ARRAYS OF SHAPED METALLIC NANOCRYSTALS

by

Maria Teresa Perez Cardenas

Thesis submitted to the Faculty of the Graduate School of the
University of Maryland, College Park, in partial fulfillment
of the requirements for the degree of
Doctor of Philosophy
2017

Advisory Committee:
Professor Zhihong Nie, Chair
Professor YuHuang Wang
Professor Efrain Rodriguez
Professor Alice Mignerey
Professor John Cumings

© Copyright by
Maria Teresa Perez Cardenas
2017

Dedication

I would like to dedicate this dissertation to my parents, Jorge Alberto Perez and Maria Teresa Cardenas, and my sister Lorena Perez.

Acknowledgements

I would like to thank my advisor, Prof. Zhihong Nie, for his continuous research support and guidance. Over the course of my graduate study, he was very understanding of the challenges I encountered. He believed in my capabilities and helped me to excel in my research. Moreover, I would like to thank Prof. Zhihong Nie for permitting me to participate in extra-curricular activities with a variety of organization on and off campus such as the University of Maryland Senate, Chemistry & Biochemistry Graduate Student Organization (Chem & Biochem GSO), Association for Women in Science (AWIS), among others. Volunteering with all of these organizations were not only fulfilling for me, but they were also important for my career development, as I was building a career path toward science policy.

I would like to thank my lab-mates, Marcus Carter, Shaoyi Zhang, Kuikun Yang , Hongyu Guo, Qian Zhang, Dr. Zhiqi Huang, Dr. Peng Zhang, Dr. Lei Wang, Dr. Jie He, Dr. Yijing Liu, Dr. Yang Yang, Dr. Chuncai Kong, and Dr. Chenglin Yi for their research guidance, moral support, and for teaching me the value of cultural diversity, collaboration, and resilience.

I would like to thank my friends from graduate school, Dulith Abeykoon, Shahnawaz Zaheer, Romina Heymann, Dr. Urszula Nowicka, Dr. Aaron Geller, and Dr. Karina Herrera-Guzman, Dr. Apurva Chaturvedi for your companionship and all the enjoyable times we spent together. While I was completing my Ph.D. studies, away from my family, your friendship brought love and happiness to my life. Special thanks to Dr. Apurva Chaturvedi, friend, and partner, who was with me in the last and

hard weeks of finalizing the thesis. You gave me strength and motivated me to finish writing the thesis.

I would like to thank my family for their love, care, and moral support through my Ph.D. studies. Dad, thank you, for sharing with me your knowledge and admiration for science. You inspired me to pursue a career in chemistry. Mom, thank you, for all your prayers for my well-being and career success (*Spanish translation: Mami, gracias por todas tus oraciones por mi bienestar y exitos en mi carrera*). Special thanks to my ‘little’ brothers Jorge Alberto and Juan Camilo, for cheering me up from distance, and most importantly for taking care of our parents, while ‘big’ sister was away from home pursuing a Ph.D. Knowing that you were taking care of our parents, I could concentrate on my Ph.D. studies without any concerns. I knew our parents were in great care. Thanks to my sister Gloria Patricia, who, toward the last days prior my Ph.D. defense, lifted-up my spirit and helped me to gain confidence in myself and my work. Finally, special thanks to, my ‘go-to’ person, my soul-mate, my ‘orange-socks’ (*Spanish translation: media naranja*), my sister, Lorena Perez, with whom I shared the sad and happy moments of the Ph.D. journey. Thank you, Lore, for your love and unconditional moral support. Despite we lived a thousand miles away from each other, I never felt alone. Through our phone conversations and your frequent visits, you filled my heart with hope and my mind with confidence. From the beginning to the end, you gave me the strength to keep going and complete my Ph.D. studies. This career achievement would not have been possible without your love and support.

Table of Contents

Dedication	ii
Acknowledgements	iii
Table of Contents	v
List of Tables	vii
List of Figures	viii
List of Abbreviations	xii
Chapter 1: Synthesis, Properties and Applications of Noble Metal Nanoparticles	1
1. Noble Metal Nanoparticles	1
2. Shapes of Noble Metal Nanoparticles	3
3. Synthesis of Noble Metal Nanocrystals	7
4. Properties and Applications of Noble Metal Nanocrystals Ensembles	10
5. Methodologies for Fabrication of Two-dimensional Arrays of Nanocrystals	14
Chapter 2: One-pot Synthesis of Au Polyhedral Nanocrystals	19
2.1. Introduction	19
2.2. Experimental Methods	22
2.2.1. <i>Materials</i>	22
2.2.2. <i>Synthesis of Au Cubes, Octahedrons and Cuboctahedrons</i>	22
2.2.3. <i>Formation of [AuBr₄]⁻ Complex</i>	24
2.2.4. <i>Reduction of [AuBr₄]⁻ Complex with AA</i>	24
2.2.5. <i>Nucleation with Different Salts and Bases</i>	25
2.2.6. <i>Characterization</i>	25
2.3. Results and Discussion	25
2.3.1. <i>The Effect of Temperature on Shape Transformation of Nanocrystals</i>	26
2.3.2. <i>Formation of [AuBr₄]⁻ Complex</i>	28
2.3.3. <i>Reduction of [AuBr₄]⁻ Complex with AA</i>	30
2.3.4. <i>Nucleation with Different Bases and Salts</i>	35
2.3.5. <i>Au(I) Ions Incubation Time</i>	37
2.4 Conclusion	38
Chapter 3: Immobilized Seed-mediated Growth of Two Dimensional Array of Au Octahedrons with Defined Orientations	40
3.1. Introduction	40
3.2. Experimental Methods	42
3.2.1. <i>Materials</i>	42
3.2.2. <i>Surface Modification of Shaped Au Seeds</i>	42
3.2.3. <i>Self-assembly of Polystyrene-grafted Au Nanocrystals into 2D Arrays</i> ...	43
3.2.4. <i>Removal of Polystyrene from the Top Surface of Au Nanocrystals</i>	44
3.2.5. <i>Au Deposition on Exposed Surface of Au Nanocrystals Arrays</i>	44
3.2.6. <i>Characterization</i>	45
3.3. Results and Discussion	45
3.3.1. <i>Self-assembly of Polystyrene-grafted Au Nanocrystals into 2D Arrays</i> ...	46
3.3.2. <i>Removal of Polystyrene from the Top Surface of Au Nanocrystals</i>	47
3.3.3. <i>Array of Truncated Octahedrons with <110> Orientation</i>	48

3.3.4. <i>Array of Au Octahedrons with <100> Orientation</i>	54
3.3.5. <i>Array of Au Octahedrons with <111> Orientation</i>	58
3.4. Conclusion	61
Chapter 4: Growth of Two-dimensional Array of Au@Pd Asymmetrical Polyhedrons with Defined Orientations	63
4.1. Introduction	63
4.2. Experimental Methods	65
4.2.1. <i>Materials</i>	65
4.2.2. <i>Pd Deposition on Exposed Surface of Au Nanocrystal Arrays</i>	66
4.2.3. <i>Characterization and Sample Preparation</i>	66
4.3. Results and Discussion	67
4.3.1. <i>Array of Asymmetric Nanocrystals with Au Cuboctahedral Core and Pd Cubic Shell Nanocrystals</i>	68
4.3.2. <i>Array of Asymmetric Au Cubic Core and Pd Cubic Shell Nanocrystals</i> ..	71
4.4. Conclusion	73
Chapter 5: Conclusion and Future Work	74
Bibliography	88

List of Tables

Table 1-1. Characteristics of some lithography methods.

Table 2-1. Reagents for one-pot synthesis of Au polyhedral NCs.

Table 2-2. The effect of reaction temperature on the onset of nucleation.

Table 2-3. List of salt and bases used to induce nucleation.

List of Figures

Figure 1-1. Schematic illustration of localized surface plasmon.

Figure 1-2. Schematic illustrating light trapping by scattering from metal NPs in a solar cell.

Figure 1-3. 3D models showing the crystal facets of Au cuboctahedron in three different orientations.

Figure 1-4. Schematic illustrating the Raman spectra for methylene blue bound to Au cubes, spheres, and trisoctahedrons.

Figure 1-5. Schematic showing the difference between homogeneous and heterogeneous nucleation.

Figure 1-6. Schematic showing the proposed reaction pathways for enhanced H₂ production from Au@Pd NCs supported on metal organic framework.

Figure 1-7. Schematics of Au NPs vesicles for cancer therapy.

Figure 1-8. Schematics of Ag cubes dimers placed over different substrates exposed to x-polarized plane wave of light.

Figure 1-9. Schematic illustrating the magnified view of single Au bow-tie element interacting with incident light pulse.

Figure 1-10. Schematic and SEM image of the hydrogen cell composed of Au nanorods coated with TiO₂.

Figure 1-11. Schematic illustrating the two commonly used self-assembly methods to fabricate 2D array of NPs.

Figure 2-1. Schematic illustrating the two steps of seed mediated growth synthesis for Au NCs.

Figure 2-2. SEM images of the Au polyhedrons obtained at different reaction temperatures.

Figure 2-3. UV-Vis spectrum of Au-CTAB solution showing the absorption bands of [AuBr₄]⁻ complex.

Figure 2-4. UV-Vis spectra of (Au-CTAB)-AA solution showing the reduction of [AuBr₄]⁻ complex with different mole ratio of Au and AA.

Figure 2-5. UV-Vis absorbance plot of (Au-CTAB)-AA solution as a function of incubation time.

Figure 2-6. Proposed structure of the Au-AA complex.

Figure 2-7. ^1H NMR spectra of Au-AA complex and pristine L-ascorbic acid (AA).

Figure 2-8. ^1H - ^{13}C HSQC spectrum of Au-AA complex.

Figure 2-9. SEM images of nanocrystals obtained when (Au-CTAB)-AA solution was incubated at different periods of time.

Figure 3-1. Schematic of immobilized seed-mediated growth method to fabricate 2D arrays of asymmetric NCs with specific orientation.

Figure 3-2. Photo showing the set-up for the self-assembly of polystyrene-grafted Au seeds into 2D monolayer arrays.

Figure 3-3. SEM image of 2D array of Au NPs with and without being treated with oxygen plasma.

Figure 3-4. SEM images and 3D models illustrating the shape transformation of Au cuboctahedra seeds with $\langle 110 \rangle$, $\langle 100 \rangle$, $\langle 111 \rangle$ orientation along the substrate.

Figure 3-5. SEM image of 2D array of spherical Au seed NPs before and after Au deposition.

Figure 3-6. SEM images and 3D models of cuboctahedral seeds and asymmetrical truncated octahedrons.

Figure 3-7. SEM images, 3D, and 2D models illustrating the time-dependent shape evolution of Au cuboctahedral seeds along the $\langle 110 \rangle$ orientation.

Figure 3-8. SEM images and 3D models illustrating the shape transformation of Au truncated cubic seeds with $\langle 110 \rangle$, $\langle 100 \rangle$, $\langle 111 \rangle$ orientation along the substrate.

Figure 3-9. SEM images, 3D, and 2D models illustrating the time-dependent shape evolution of Au truncated cubic seeds along the $\langle 100 \rangle$ orientation.

Figure 3-10. SEM images and 3D models of asymmetric Au cuboctahedrons and Au octahedron along the $\langle 100 \rangle$ orientation.

Figure 3-11. SEM images and 2D projections of resulting asymmetric cuboctahedron and octahedrons.

Figure 3-12. SEM images and 3D models showing the shape transformation of Au octahedral seeds with $\langle 110 \rangle$ and $\langle 111 \rangle$ orientation along the substrate.

Figure 3-13. SEM images and 3D models of octahedrons with $\langle 111 \rangle$ orientation

Figure 3-14 SEM images, 3D, and 2D models illustrating the time-dependent shape evolution of Au octahedral seeds along the $\langle 111 \rangle$ orientation.

Figure 4-1. Schematic showing Au@Pd core-shell NCs capability to detect H_2 and transform to Au@PdH.

Figure 4-2. Schematic illustration of immobilized seed-mediated growth of 2D array of asymmetric Au@Pd polyhedral NCs.

Figure 4-3. SEM and TEM images of 2D array of asymmetrical Au cuboctahedral core with Pd cubic shell NCs.

Figure 4-4. 3D models showing shape transformation of Au cuboctahedral seeds into Au cuboctahedral core with Pd cubic shell with $\langle 110 \rangle$ $\langle 100 \rangle$ $\langle 111 \rangle$ orientation along the substrate.

Figure 4-5. SEM images, 3D, and 2D models illustrating the shape transformation of Au cuboctahedral seeds into Au@Pd core-cubic shell with $\langle 110 \rangle$ orientation.

Figure 4-6. SEM and TEM images of 2D array Au cubic core with Pd cubic shell NCs.

Figure 4-7 EDS line scans of a single Au cubic core with Pd cubic shell NC.

Figures from Appendix

A.1. UV-VIS spectrum of CTAC surfactant and KBr.

A.2. UV-VIS absorption of 1:2 mole equivalent of Au and Br⁻ sources.

A.3. UV-Vis spectra showing the $[AuBr_4]^-$ complex reduction with) 1:1 and 1:4 mole equivalent of Au and AA.

A.4 1H - 1H COSY of Au-AA complex showing proton coupling.

A.5. 1H NMR full spectra of Au-AA complex and AA.

A.6. ^{13}C NMR spectra of Au-AA complex and AA.

A.7. 1H - ^{13}C HSQC of AA.

A.8. Experimental conditions for shape transformation of Au cuboctahedral seeds into truncated octahedrons with $\langle 110 \rangle$ orientation.

A.9. Experimental conditions for shape transformation of truncated cubic seeds into cuboctahedrons, truncated octahedrons, and octahedrons with $\langle 100 \rangle$ orientation.

A.10. Experimental conditions for growth of Au octahedral seeds with $\langle 111 \rangle$ orientation.

A.11. Schematics illustrating drop casting method to fabricate 2D array of shaped Au NPs seeds.

A.12. Dimensions of Au NCs in the course of shape evolution from Au cuboctahedrons to octahedrons.

A.13. Dimensions of Au NCs in the course of shape evolution from Au truncated cubes to octahedrons.

A.14. Dimensions of Au octahedral seeds in the course of Au deposition.

A.15. Experimental conditions for shape transformation of Au cuboctahedral seeds into Au@Pd cubic polyhedrons with $\langle 100 \rangle$ orientation.

A.16. Dimensions of Au cuboctahedrons in the course of shape evolution to Au@Pd core-cubic Shell

List of Abbreviations

Au-CTAB.....	Au and Hexadecyltrimethylammonium bromide solution
AA.....	L-Ascorbic acid
(Au-CTAB)AA.....	Au hexadecyltrimethylammonium bromide and L-Ascorbic acid
BCP.....	Block Copolymer
CTAB.....	Hexadecyltrimethylammonium bromide surfactant solution
CTAC.....	Hexadecyltrimethyl ammonium chloride surfactant solution
fcc.....	face-centered cubic
FEM.....	Finite Element Simulation
LB.....	Langmuir Blodgett
LED.....	Light-emitting diodes
LSPR.....	Localized Surface Plasmon Resonance
NCs.....	Nanocrystals
NPs.....	Nanoparticles
PS-SH.....	Thiol terminated Polystyrene
SEM.....	Scanning Electron Microscope
SERS.....	Surface-enhanced Raman Spectroscopy
SLL.....	Solid-state lighting
TEM.....	Transmission Electron Microscope
2D.....	Two dimension

Chapter 1: Synthesis, Properties and Applications of Noble Metal Nanoparticles

“Nanotechnology is the way of ingeniously controlling the building of small and large structures, with intricate properties; it is the way of the future, a way of precise, building with incidentally, environmental benignness built in by design.”

Dr. Roald Hoffman
Nobel Prize in Chemistry
1981

1. Noble Metal Nanoparticles

Noble metal nanoparticles (NPs) have unique physical and chemical properties that are dependent on their size¹, composition², and shape³. Upon interaction with electromagnetic field, the conduction band electrons of these NPs (i.e. Au, Ag,) collectively oscillate, thus exhibiting the so-called localized surface plasmon resonance⁴⁻⁶ (LSPR) (Figure1-1). The coupling between light and NPs surface plasmons results in optical force enhancement, and localization and manipulation of light.

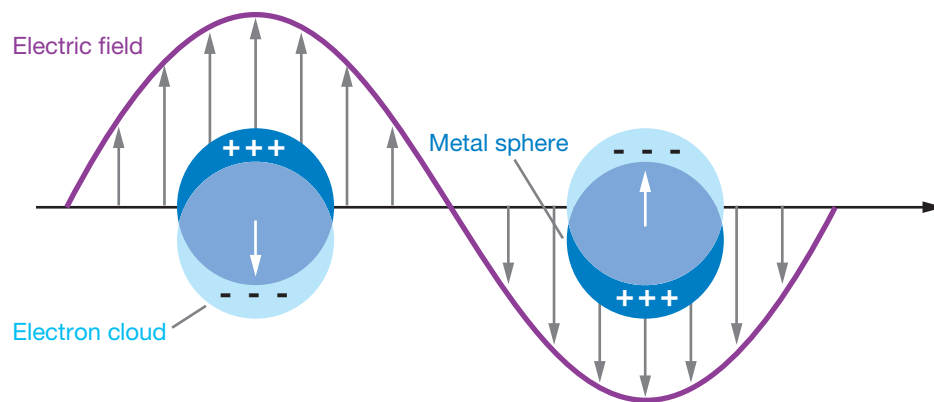


Figure 1-1. Schematic illustration of localized surface plasmon resonance. When NPs are excited by an electric field (E_0), the free electrons are displaced from the lattice and oscillate in resonance with the electric field. Figure adapted with permission from Annual Reviews [Ref 6], Copyright 2007.

The LSPR of noble metal NPs has enabled a broad range of their applications in different fields such as, photovoltaics⁷⁻⁸, catalysis⁹⁻¹⁰, sensing¹¹⁻¹² and therapeutics¹³⁻¹⁵. In the field of photovoltaics, Atwater *et al.*¹⁶⁻¹⁷ conducted a study of light coupling to a silicon substrate coated with Ag NPs. Ag NPs coated in absorber layers scatter and trap sunlight in the photovoltaic cell. Therefore, the increase in the effective path of light passing through the semiconductor allows the reduction of photovoltaic layer thickness while keeping the optical absorption efficient (Figure 1-2). Stuart and Hall *et al.*¹⁸⁻¹⁹ reported that dense arrays of plasmonic metal NPs can be used to scatter light into Si insulator photodetectors. A 20-fold increase in the infrared photocurrent was achieved using such NP arrays. Furthermore, NPs of size comparable to the wavelength of light are suitable for enhancing light-matter interaction in solid-state lighting (SLL) and hence the efficiency of light-emitting diodes²⁰ (LEDs). In this case, NPs arrays serve as optical antennas providing resonant amplification and directional radiation. The process can be explained in two steps: transfer of energy from an emitter to plasmon modes, and radiative plasmon coupling which produces radiation enhancement.

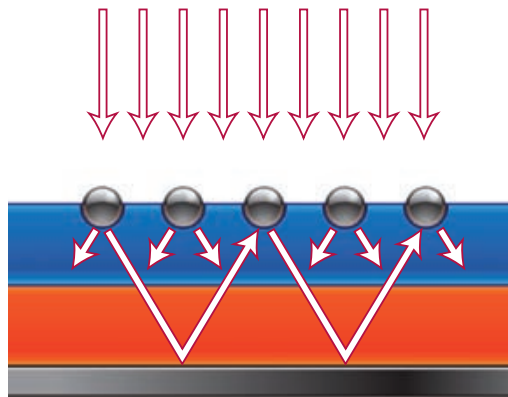


Figure 1-2. Schematic illustrating light trapping by scattering from metal NPs in a solar cell. Figure adapted with permission from Macmillan Publishers Ltd: Nature Materials [Ref 17], copyright 2010.

2. Shapes of Noble Metal Nanoparticles

The allure of noble metal NPs arises from the tunability of optical properties by varying geometric shapes.²¹⁻²³ The shapes of noble metal NPs are largely dependent on two major structural factors: crystallinity and surface facets²⁴⁻²⁶. Take Au and Ag noble metal NPs as an example, the crystallinity of NPs is determined at the nucleation stage, where seeds acquire face-centered cubic (fcc) lattice, which can be single-crystalline, poly-crystalline, or multiply-twinned (i.e crystal twin defects). In a single-crystalline NP, the atoms are arranged in a periodic manner throughout the entire NP, without grain boundaries. On the contrary, NPs with multiple twin defects are composed of two or more inter-grown crystals with mirror symmetry to each other. Depending on growth conditions, seed NPs with the same internal structure (i.e single-crystalline or multiply-twinned) can evolve into nanocrystals (NCs) with different polyhedral shapes (e.g., cubic, octahedral, or cuboctahedral polyhedrons).

Like conventional crystals, NCs have an internal regular lattice by which atoms organize based on the unit cell forming the facets of NCs²⁷⁻²⁸. The crystal facets are described in terms of the orientation of the facet with respect to the unit cell, $\{h,k,l\}$, known as Miller Indices. The three main low-index facets in fcc are $\{100\}$, $\{111\}$, and $\{110\}$. These three crystal facets constitute the faces, which bounded together give NCs specific polyhedral shape. For instance, cuboctahedral NCs are composed of eight triangular $\{111\}$ facets and six square $\{100\}$ crystal facets (Figure 1-3).

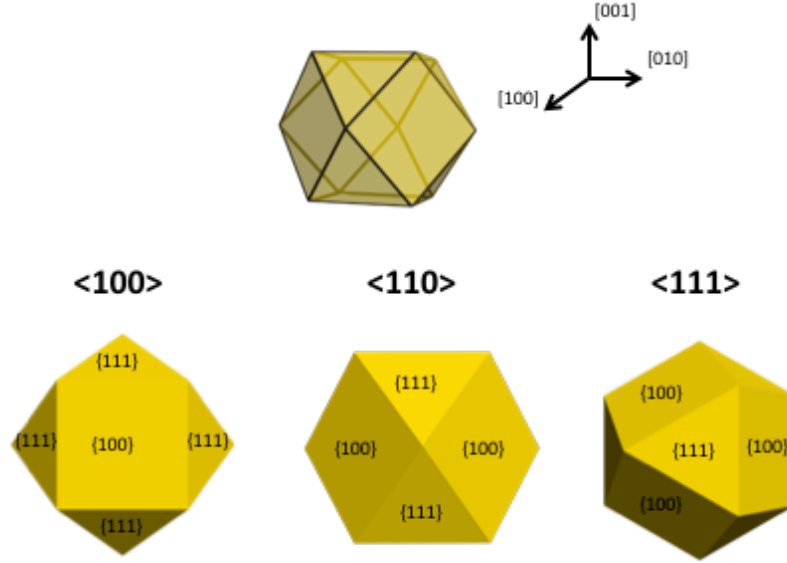


Figure 1-3. 3D models showing the eight triangular $\{111\}$ and six square $\{100\}$ crystal facets of a Au cuboctahedron in three different orientations.

The polyhedral shape of NCs is commonly attributed to the relative growth rate of the faces²⁹ (Equation 1.1).

$$R = A (\Delta\mu/kT)^2 \quad \text{Eq. 1.1}$$

where R is the growth rate of a crystal facet, A is a constant, μ is the difference in the chemical potential of solution and solid phase, k is the Boltzmann constant, and T is temperature. Crystal facets of large R disappear, while those facets with small R increase in size to reach an equilibrium state with minimal surface energy (γ). According to Wulff's surface energy theory, the combination of all crystal facets should be considered to determine the total minimum surface energy of the crystal³⁰. For Au single crystalline seeds, depending on the growth conditions, the rate of growth can favor either $\{100\}$, $\{111\}$, or reach equilibrium between both crystal facets to produce octahedrons, cubes, and cuboctahedrons, respectively.

A classic example about the optical properties of noble metal NPs is the enhanced local electromagnetic field, which enables sensitive surface-enhanced Raman spectroscopy (SERS) detection of Raman active molecules. The enhancement of SERS signals is strongly dependent on the shape of plasmonic NPs. Au cubes can enhance the localized electromagnetic field at the eight vertices.³¹⁻³³ Murphy *et al.*³⁴ investigated the edge corner effect of shaped Au NCs on their performance in surface-enhanced Raman spectroscopy (SERS) detection. Au NCs with cubic, spherical, and trisoctahedral shapes were used to trap methylene blue, a Raman-active molecule, by coating the surface with polyelectrolytes (Figure 1-4). Experimental study of these NP suspensions revealed that Au cubes and spheres exhibited the SERS signal intensity of $5.63 \pm 0.56 \times 10^3$ and $0.87 \pm 0.52 \times 10^3$ counts, respectively. Finite Element Simulation (FEM) was performed to correlate the SERS signal intensity to the morphology of NCs. A comparison between experimental and computational studies suggests that the largest enhancement in Au cubes arises from electromagnetic enhancement at the sharp corners.

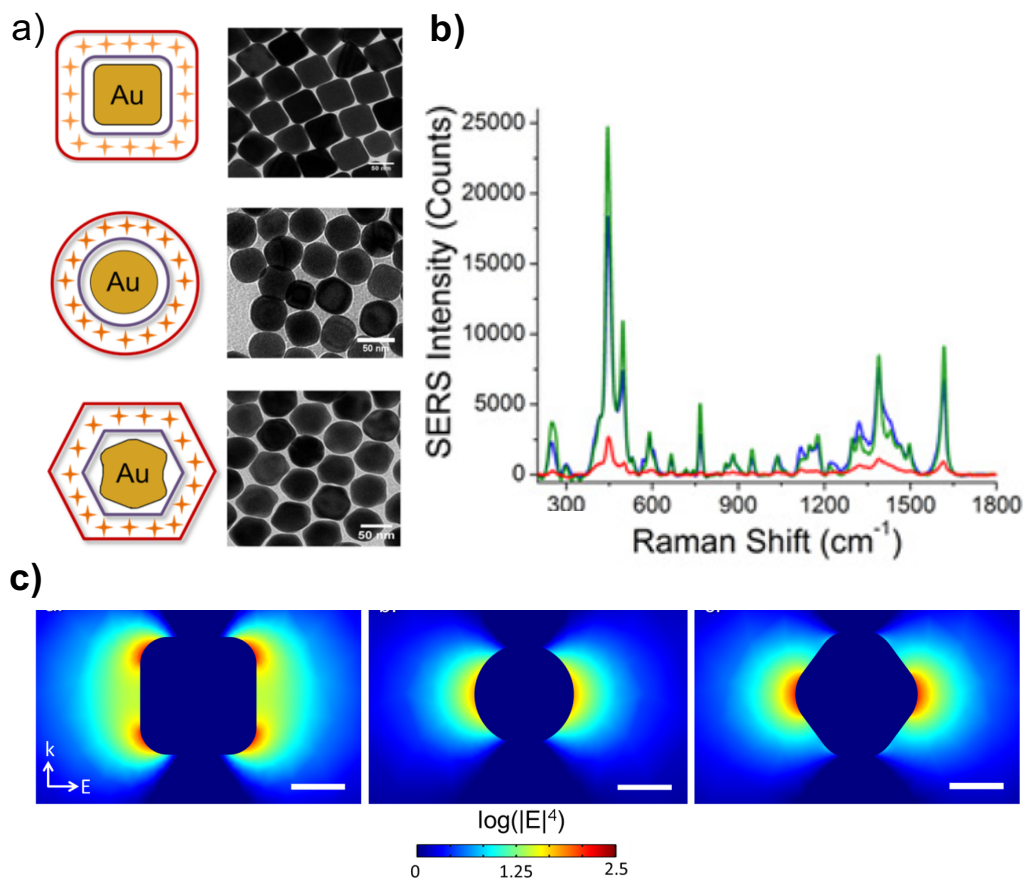


Figure 1-4 a) Schematic illustrating the loading of methylene blue (orange crosses) around Au cubes, spheres, trisoctahedrons coated with polyelectrolytes (purple and red lines) and their corresponding SEM images. b) Raman spectra for methylene blue bound to Au cubes (green line), spheres (red line), trisoctahedron (blue line). c) From left to right, electric field distribution of cube, sphere, trisoctahedron. Figure adapted with permission from American Chemical Society [Ref 34], Copyright 2013.

Concurrently, the crystal facets of NCs determine their catalytic properties due to their facet surface energies. For instance, Wang *et al.*³⁵ studied the effect of crystal facets of Au NCs on their performance as cathode catalysts in lithium-oxygen batteries. Au cubic NCs enclosed by {100} facets, truncated octahedral NCs enclosed by {100} and {111} facets, and trisoctahedral NCs enclosed by 24 high-index {441} facets showed catalytic performance toward oxygen reduction and oxygen evolution

reaction in lithium-oxygen batteries. The Au NCs with different crystal facets {100}, {111} and {441} reduced the reaction energy of Li and O atoms by 4.00, 3.81, and 1.63 J m⁻², respectively. The {411} crystal plane had the highest surface energy of 2.55 J m⁻² and provided more reactive sites for interaction with Li and O atoms, thus resulting in the lowest charge overpotential (~0.9 V) and the highest reversible capacity (~ 20,298 mA h g⁻¹).

3. Synthesis of Noble Metal Nanocrystals

Wet-chemical synthesis of NCs relies on the reduction of metal precursor in solution phase³⁶. The synthesis of NCs is commonly divided in two main steps: nucleation and growth. Experimentally, nucleation and growth can take place independently (i.e., in different reaction media), or consecutively (i.e., in the same reaction medium). When the nucleation and growth occurs in different reaction medium, the synthetic method is known as seed-mediated growth³⁷⁻³⁸. This method is based on heterogeneous nucleation, where growth of metal occurs on top of pre-synthesized seeds. By isolating the nucleation phase from the growth phase, multiple nucleations are avoided during the growth step. This is because heterogeneous nucleation has lower energy barrier than homogeneous nucleation³⁹. Solutions with seeds and high concentration of metal precursor, atoms will prefer to deposit on the seeds rather than forming new nuclei (Figure 1-5a). Therefore, in a growth solution, all the metal precursor will be used for the growth of the pre-existing seeds. Seed-mediated growth method is commonly used to fabricate NCs of different shapes like Au nanorods⁴⁰ (This method is explained in detail in chapter 2). Another traditional method is the one-pot synthesis method, which relies on homogeneous nucleation⁴¹⁻⁴².

In this method, nucleation and growth occur consecutively in the same reaction medium. In the case of homogeneous nucleation, the nucleation depends on the concentration of the reduced metal to be used to form the seeds. This concept is supported by LaMer's nucleation study⁴³⁻⁴⁴. According to LaMer's nucleation mechanism, the experimental conditions to obtain monodisperse nucleation is to achieve a high rate of nucleation to burst of nuclei formation by reaching supersaturation of ions or atoms (Figure 1-5b). Homogeneous nucleation is commonly used in the one-pot synthesis to fabricate Au nanoparticles with spherical shapes⁴⁵⁻⁴⁶.

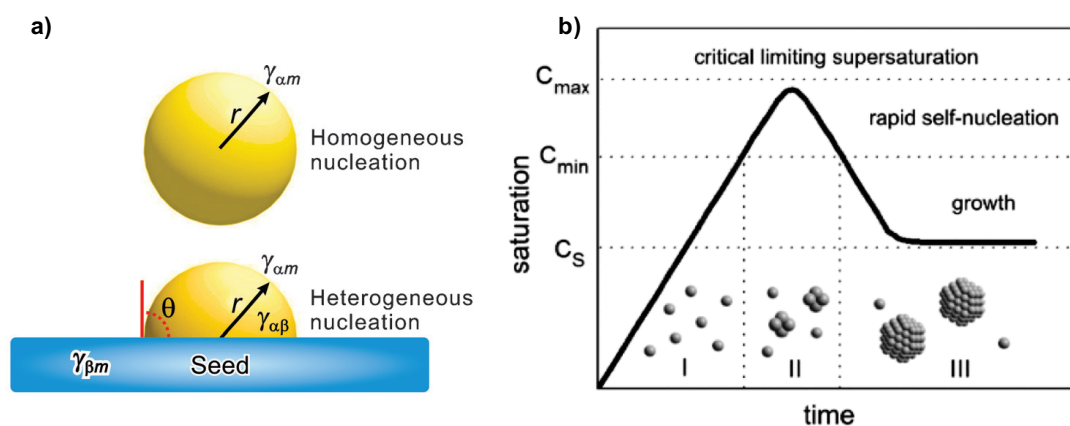


Figure 1-5. (a) Schematic showing the difference between homogeneous and heterogeneous nucleation. (b) Plot of monomer concentration as function of time showing the critical supersaturation that can lead to nucleation and subsequently growth of NCs. Figure (a) adapted with permission from John Wiley and Sons [Ref 39], Copyright 2017. Figure (b) adapted from Ref [44] Open Access figure under a Creative Commons Attribution 3.0 International License.

Mono-metallic NCs (e.g., Au and Ag) have been extensively studied for developing plasmonic-based materials⁴⁷⁻⁴⁹. In contrast, bimetallic NCs composed of two distinct metals exhibit enhanced photocatalytic properties⁵⁰⁻⁵². The enhancement could be due to the coupling between the catalytic and optical properties of different compositions within such NCs. Bimetallic NCs can exist in different forms, such as

core-shell, dumbbell-like, etc. As in the core-shell form, the inner core metal (M_1) is coated with a shell made of (M_2) and the resulting NCs is typically denoted by $M_1@M_2$.

Core-shell NCs have shown broad applications in catalysis, light harvesting, and sensing.^{51, 53} For instance, Au@Pd core-shell nanospheres are attractive for catalysis. Yamashita *et al.*⁵⁴ designed Au@Pd NCs supported on a metal organic framework to catalyze the dehydrogenation of formic acid to produce H_2 gas under visible light irradiation and room temperature (Figure 1-6). In this system, constituent Au islands absorb visible light and create hot electrons that are transferred to Pd, thus enhancing the catalytic property of Pd.

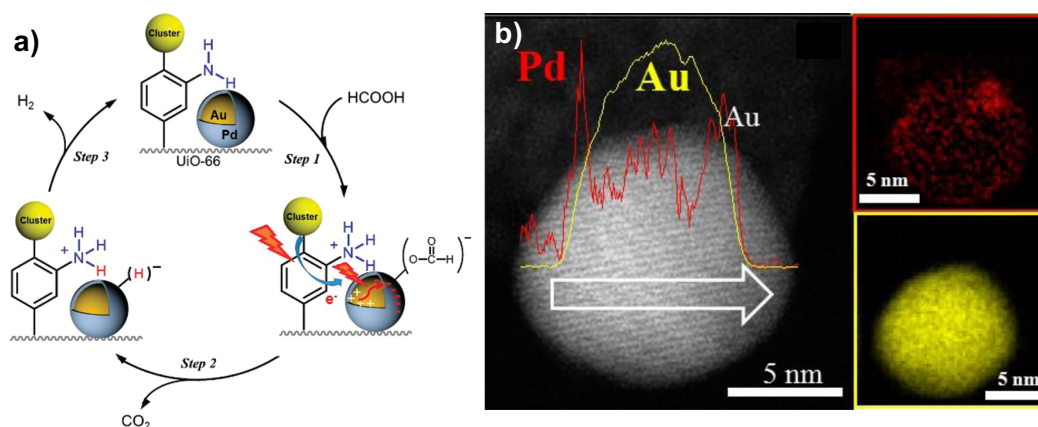


Figure 1-6. Schematic showing the proposed reaction pathways for enhanced H_2 production from Au@Pd NCs supported on metal organic framework. (b) High-magnification EDX spectra of Au@Pd NCs with elemental mapping for Pd and Au. Figure adapted with permission from American Chemical Society [Ref 54], Copyright 2017.

The shape, size, and composition of noble metal NCs are crucial to their properties and applications. In the past decade, great progress has been achieved in the fabrication of monodisperse Au polyhedral NCs with controlled shape⁵⁵⁻⁶⁰. However, it is a notorious method since the outcome of the synthesis varies

drastically from one laboratory to another. This is largely due to the lack of a comprehensive understanding of the synergic reaction between reagents, which can negatively impact the nucleation and growth of NCs. Therefore, there is an urgent need to further improve the existing solution-based methodologies, in order to fabricate high-quality Au polyhedral NCs in a reproducible manner.

In chapter 2, we discuss experimental parameters that influence the nucleation and crystal growth in the one-pot method to fabricate Au NCs with cubic, octahedral, and cuboctahedral shapes. We propose that a Au complex intermediate is formed during the reduction of Au metal precursor and the deprotonation of the complex leads to onset of nucleation. This finding offers new insights into the one-pot and seed mediated growth methods of shaped NCs.

4. Properties and Applications of Noble Metal Nanocrystals Ensembles

Controlling the organization of noble metal NCs in one, two, or three dimensions (i.e., 1D, 2D, 3D) is important for creating novel functional materials with applications in photonics, catalysis, and medical diagnosis and therapy.^{32, 61-62} The organization of Au NCs leads to new or collective optical properties due to the strong surface plasmon coupling between neighboring NCs.⁶³⁻⁶⁵ When two or more Au NCs are in proximity to each other, the plasmonic modes of the NCs couple and enhanced optical fields. For instance, the plasmonic coupling arising from 3D hierarchical assemblies have received great attention to design medical diagnostic and therapeutic treatments of tumors.^{57, 66-68} Nie *et al.*⁶⁹ designed a multifunctional theranostic platform based on photosensitizer-loaded vesicular assemblies of Au NPs for cancer imaging and treatment (Figure 1-7). The Au NPs modified with thio-

terminated block copolymer self-assembled into photosensitizer Ce6-loaded vesicles composed of a monolayer membrane of Au NPs. The vesicles showed a strong absorbance in the NIR range of 650-800 nm due to the plasmonic coupling between NPs, facilitating their biomedical applications. The Ce6-loaded Au vesicles were injected in a tumor and irradiated with 671 nm laser. Heat was produced and Au NP vesicles dissociated to release the payload. Cancer cells were killed through the heat and reactive species generated by reacting photosensitizer Ce6 with oxygen in tissues.

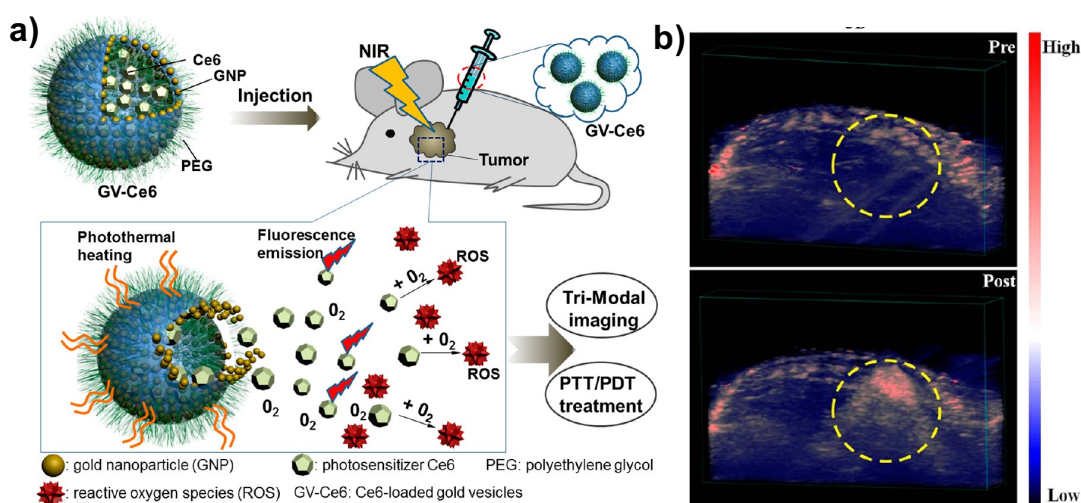


Figure 1-7. (a) Schematics of photosensitizer (Ce6)-loaded Au NPs vesicles for fluorescence, thermal, and photoacoustic imaging and photodynamic cancer therapy b) *In vivo* photoacoustic image pre- and post- injection of (Ce6)-loaded Au NPs vesicles (Yellow circles indicate the injection location). Figure adapted with permission from American Chemical Society [REF 69], Copyright 2013.

In solid phase, noble NCs embedded in substrate and in close proximity to each other also show tunable plasmon modes. Ding *et al.*⁷⁰ showed modification in the resonance modes for Ag cubes dimers on glass, Si, and Ag substrate. Upon irradiation, Ag cubes dimers placed on Ag substrate depicted well-defined resonance peak extinction at 627 nm and 966 nm due to the surface plasmon polarization mode propagating on the silver-air interface of the substrate; while Ag cubes dimers placed

on glass and Si substrates showed blue shift on the resonance peaks extinctions and strong scattering effect (Figure 1-8).

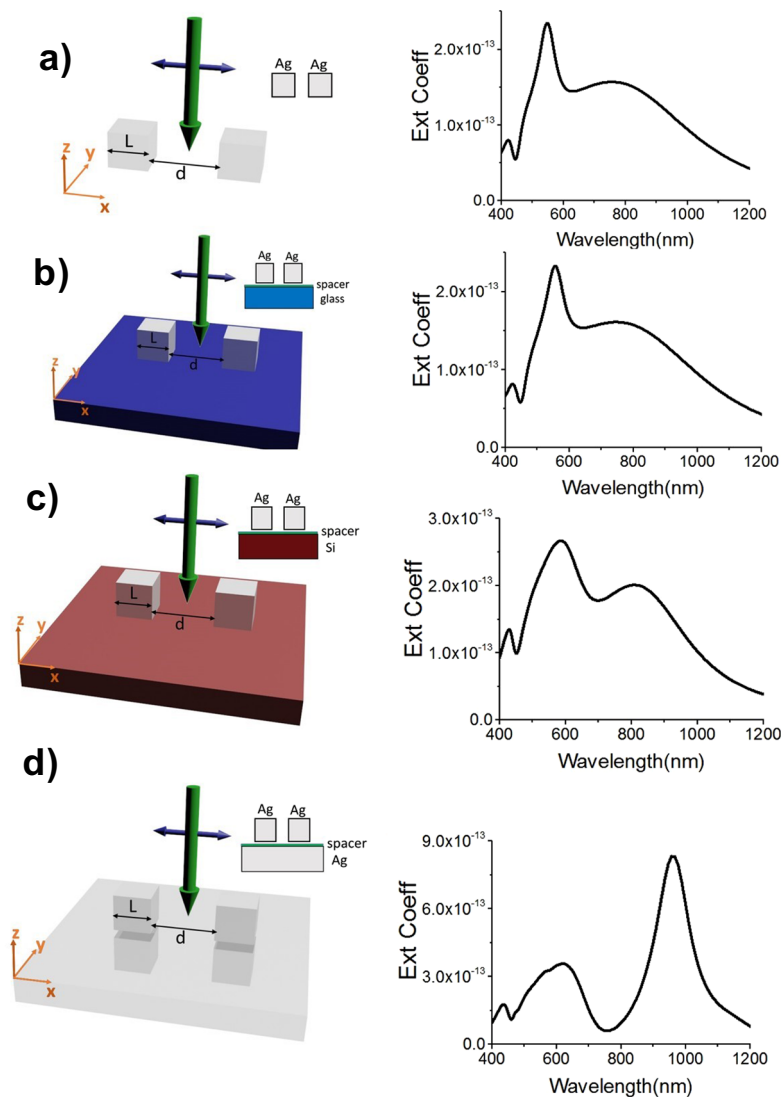


Figure 1-8. Schematics of Ag cubes dimers placed over different substrates (a) no substrate (b) glass, (c) Si, and (d) Ag, exposed to x-polarized plane wave of light including their corresponding extinction coefficient spectra. Figure adapted from [REF 70] open Access figure under a Creative Commons Attribution 4.0 International License.

Among different assembly configurations, 2D arrays of NCs on substrates are of great interest in applications for chemical sensors⁷¹, high-resolution imaging,⁷²⁻⁷³

spectroscopy, and renewable energy devices.²¹ For instance, Woo Kim *et al.*⁷⁴ reported a method to produce high-harmonic generation (i.e. a process that generates coherent extreme ultraviolet) by exploiting the local field enhancement induced by 2D array of Au bow-tie elements on a sapphire substrate (Figure 1-9). The method consisted of emitting a beam from a femtosecond oscillator directly on to the array of Au bow-tie-shaped structures. The pulse intensity was enhanced by a factor of 20-40 dB, which is good to produce harmonics. This method is useful for advancing high resolution imaging and spectroscopy.

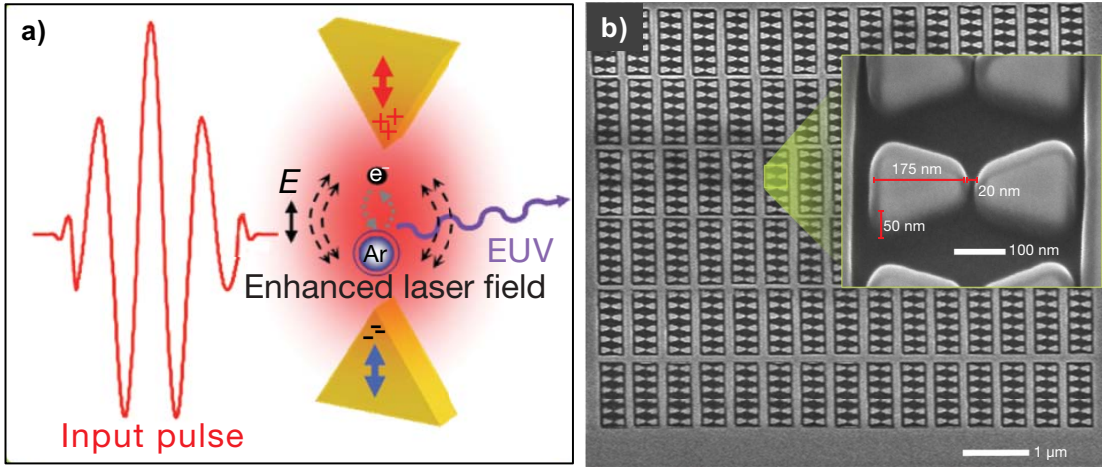


Figure 1-9. (a) Schematic illustrating the magnified view of single Au bow-tie element interacting with incident light pulse. (b) Scanning electron microscope image of Au nanostructures. Inset shows the magnified image of a single bow-tie element with the dimensions marked. Figure adapted with permission from Macmillan Publishers Ltd: Nature [REF 74], Copyright 2008.

In renewable energy, Moskovits *et al.*⁷⁵ fabricated a plasmonic water splitting cell to produce H_2 gas using visible light irradiation. The plasmonic cell was made of Au nanorods capped with TiO_2 vertically assembled into 2D array on an indium tin oxide (ITO glass) conductive substrate (Figure 1-10). Au nanorods array interspacing distance is close for generating surface plasmon coupling and increase visible light absorption. Therefore, illuminating the Au nanorods with visible light excited surface

plasmons producing hot electrons that are then transferred to the TiO_2 . This plasmonic water splitting cell system reported 95% effective charge carriers from surface plasmon to hot electrons.

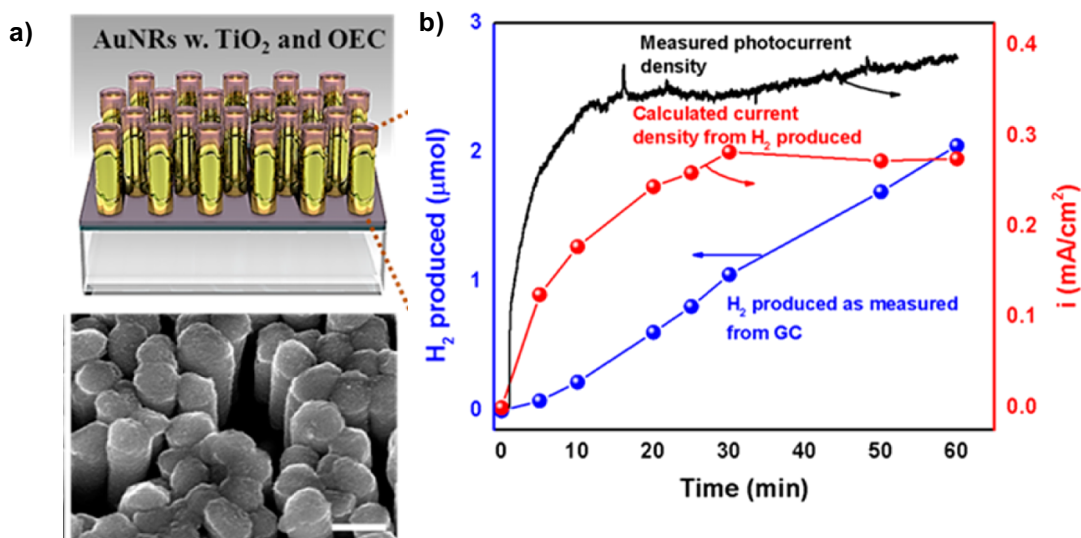


Figure 1-10. (a) Schematic and SEM image of the hydrogen cell composed of Au nanorods coated with TiO_2 (b) Quantitative graph of the hydrogen evolved over time (blue curve), photocurrent produced with visible light illumination (black curve), Photocurrent calculated from the evolved hydrogen (red trace). Figure adapted with permission from American Chemical Society [REF 75], Copyright 2012.

5. Methodologies for Fabrication of Two-dimensional Arrays of Nanocrystals

Approaches for the fabrication of 2D arrays of NCs can be generally divided into two categories: top-down and bottom-up methods. Top-down approach consists of creating geometrical pattern on a substrate from films of bulk material, while bottom-up approach relies on solution phase self-assembly of as-synthesized NCs as building blocks into 2D arrays.⁷⁶⁻⁷⁷

Top-down approach involves lithography techniques to pattern nanostructures directly on a substrate via photolithography⁷⁸⁻⁸⁰ (i.e., patterns are created with electromagnetic radiation) or soft lithography⁸¹⁻⁸² (i.e., patterns are created with

elastomers molds). Table 1-1. illustrates the main characteristics of some lithography methods. Photolithography techniques such as electron beam lithography, ion beam lithography, and UV lithography are capable of generating features with sizes below 50 nm⁸³. However, these techniques require expensive instrumentation, complicated operation and maintenance. On the other hand, soft lithography and nanoprinting lithography use elastomeric or plastic stamps to make patterns.^{81-82, 84} These techniques are low in capital cost and easy to operate. They can generate structures from ~30 nm to 500 μ m and can be used to pattern other substrates different from photoresist materials. Some of the drawbacks of soft lithography are low resolution, deformation of elastomeric stamp, especially for small patterning features, and density defects. Last but not least, colloidal lithography emerged as an unconventional lithography method for fabricating 2D arrays of plasmonic nanostructures.⁸⁵⁻⁸⁶ It uses monolayer of spherical colloidal particles as a mask for etching and metal sputtering process. This technique can generate 2D and 3D structures ranging from 50 to 200 nm in size. Generally, colloidal lithography generates triangles and spheres. To generate other shapes (e.g., nanopillars and rings), it is necessary to adjust the sputtering conditions and etching exposure time, which can be an elaborate procedure. Some of the drawbacks of this technique include defects arising from colloidal arrays, elevated temperatures for modification of colloids, procedures with reactive ion etching, and limited shapes that can be produced.

Table 1-1. Characteristics of some lithography methods.

<i>Top-down Techniques</i>	<i>Patterning Materials</i>	<i>Patterns</i>	<i>Shapes</i>	<i>Size</i>	<i>Cost</i>
Photolithography	Photon radiation	2D	Spheres Rods Rings	5-90 nm	High
	Photoresists material				
Soft Lithography	Elastomeric stamp	2D 3D	Posts Spheres	100nm -500μm	Medium/Low
Colloidal Lithography	Colloids	2D 3D	Spheres Triangles Pillars Rings	50-200 nm	Low
	Sputtering instruments				
	Reactive ion etching				

Bottom-up approach for fabricating 2D NC arrays entails assembling NCs as building blocks. This approach can be classified in two categories: 1) liquid interface-mediated assembly and 2) direct assembly on solid substrate. Figure 1-11 illustrates the two bottom-up techniques. In liquid interface-mediated process, capillary forces stabilize as-prepared NPs at the air-liquid or liquid-liquid interface⁸⁷⁻⁸⁹. A commonly used interface-mediated method is Langmuir Blodgett⁹⁰⁻⁹¹ (LB), which involves dispersion of NPs at the air-water interface, and compression of NPs with movable barriers to bring NPs together and assemble them into close pack. Once the monolayer is formed, they can be transferred to a substrate by manually immersing the substrate or mechanically using LB transfer device. Though this method can generate tens of cm² monolayer arrays, transferring the monolayer arrays without breakage to a substrate can become a challenge. To circumvent transferring the

monolayer array from solution to a substrate, direct assembly on a substrate offers a better and faster technique without the usage of any specialized equipment. Direct assembly methods are based on solvent evaporation of NP solution to control the self-assembly process directly on the substrate.⁹²⁻⁹³ One of the commonly used direct assembly methods is drop casting, in which NPs solution is injected into a water droplet on top of a substrate and allowed to evaporate.⁹⁴ By controlling evaporation conditions, and concentration of the NPs solution, NPs can self-assemble into 2D arrays with different packing modes, such as hexagonal close packing of NCs.

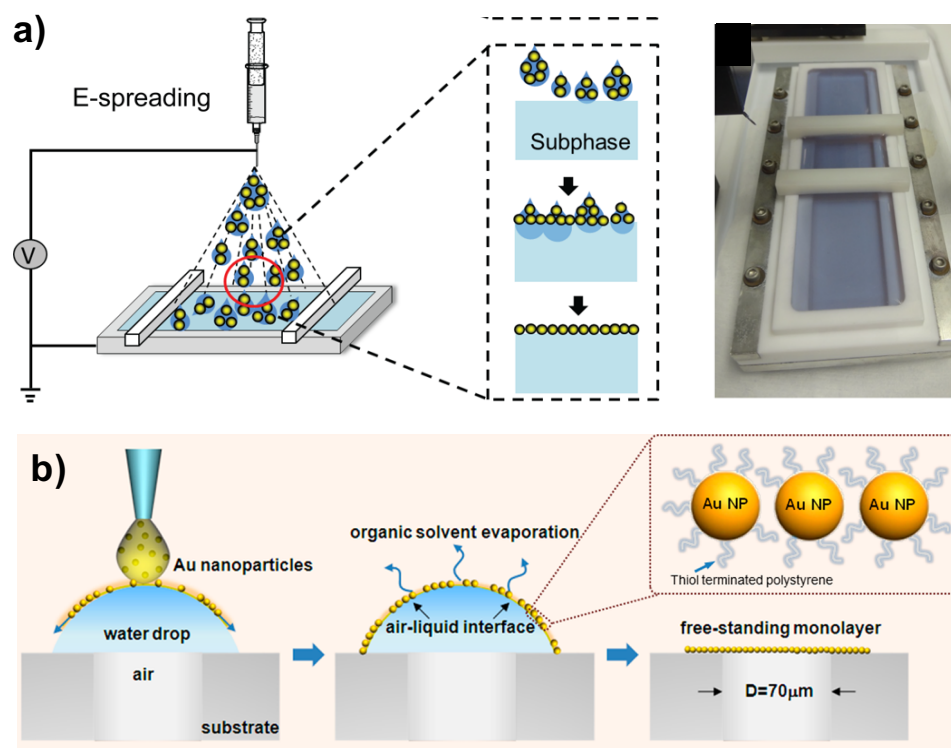


Figure 1-11. Schematic illustrating the two commonly used self-assembly methods to fabricate 2D array of NPs (a) Langmuir-Blodgett and (b) drop casting. Figures adapted with permission from American Chemical Society [REF 90,94], Copyright 2015.

Both liquid interface-mediated assembly and direct assembly on solid substrate work well for assembly of spherical NPs, but usually not for polyhedral

NPs. Spherical NPs arrange into 2D array without preference for orientation. However, polyhedral NCs exhibit different symmetry axis, which makes it challenging to assemble them directly into structures with both positional and orientational ordering. Acknowledging that the optical properties of noble metal NCs arise from their shape and organization, it is desired to develop a cost-efficient method for fabrication of defined 2D array of polyhedral NCs with controlled orientation.

In chapter 3 and 4, we report an immobilized seed-mediated growth strategy for the fabrication of 2D arrays of mono- and bi-metallic polyhedral NCs with well-defined shapes and orientations on a substrate. This method relies on the controlled solution-phase deposition of metals (i.e., Au and Pd) on selectively exposed surface of self-assembled seed nanoparticles that are immobilized on a substrate. The shape evolution of seeds to final NCs was monitored and evaluated by electron microscopic imaging. The synthetic approach developed presents an important addition to current tools for the fabrication of substrate-supported functional nanostructures as new materials and devices.

Chapter 2: One-pot Synthesis of Au Polyhedral Nanocrystals

“Research is to see what everybody else has seen,
and to think what nobody else has thought.”

Dr. Albert Szent-Györgyi
Nobel Prize in Physiology or Medicine
1937

2.1. Introduction

For the last decade, optical properties of shaped Au NCs (e.g., nanorods and nanospheres) have been extensively studied and employed in many applications, such as chemical sensors⁹⁵⁻⁹⁷, photovoltaic devices¹⁶⁻¹⁷, and biomedical imaging and diagnosis^{13, 98}. Acknowledging that the properties of nanomaterials are largely determined by their size, composition, and shape, the demand on plasmonic NCs with controlled shapes is expected to increase. Currently, seed-mediated growth method has been commonly adapted to synthesize shaped Au NCs⁹⁹⁻¹⁰³ (e.g., cubes, octahedrons). This method consists of two phases: nucleation and growth phase. In the nucleation phase, Au precursor of HAuCl_4 is reduced by NaBH_4 to form Au seeds in presence of a surfactant hexadecyltrimethylammonium bromide (CTAB) or hexadecyltrimethylammonium chloride (CTAC). Separately, a growth solution is prepared containing HAuCl_4 , CTAB, and a mild reducing agent, *L*-Ascorbic acid (AA). In the growth solution, Au precursor is reduced from Au(III) to Au(I) ions by AA. The subsequent addition of Au seeds into the growth solution leads to the reduction of Au(I) ions to Au(0). The Au(0) atoms auto-catalytically deposit on the Au seed surface to eventually produce Au NCs. The role of CTAB is believed to be two folds: prevent the aggregation of NCs and serve as a capping agent to modulate the NC morphology (Figure 2-1).

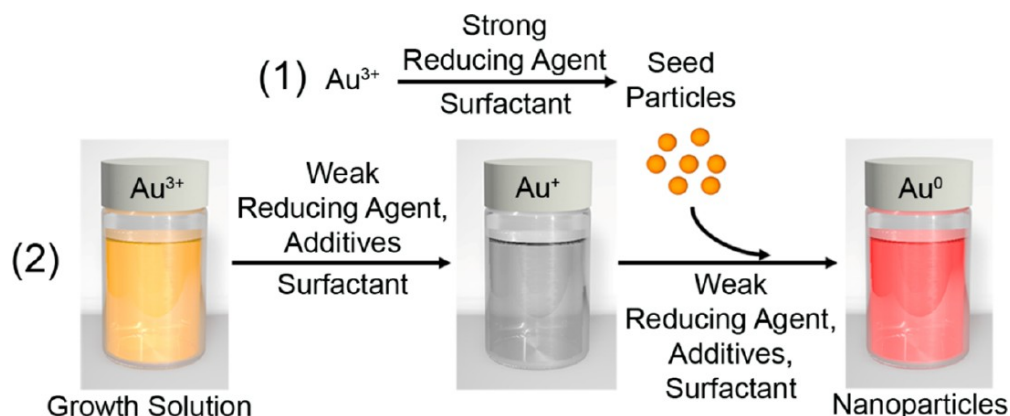


Figure 2-1. Schematic illustrating the two steps of seed mediated growth synthesis for Au NCs. First step: Au precursor is reduced from Au(III) to Au(0) ions by AA to form seeds. Second step: Au precursor is reduced from Au(III) to Au(I) and Au seeds from the first step are added to the Au(I) solution; then seeds growth into NCs. Figure adapted with permission from American Chemical Society [REF 103], Copyright 2013.

In this method, control over the shape of NCs is achieved by varying the concentration and type of surfactants and reducing agents, as well as introducing additives such as KI, AgNO_3 , and NaBr. Many hypotheses have been proposed to explain the correlation between the shape of NCs and experimental parameters. For instance, Murphy's research group suggested that growth solutions with low concentration of AA and small quantities of AgNO_3 could produce ~ 90 nm cubes¹⁰⁴. Teranishi *et al.*⁵⁸ suggested that low concentration of AA produced Au octahedrons, while higher concentration of AA led to faster growth of seeds and hence production of Au cubes and trisoctahedrons, which are the least thermodynamically stable structure. Huang *et al.*¹⁰⁵ reported that cubic NCs were obtained by adding small quantities of NaBr and replacing CTAB with CTAC in the growth solution. The addition of NaBr allowed for the control over the concentration of Br^- ions without changing the concentration of surfactants. Overall, it is believed that the Au(I)

reduction rate increases with increasing the concentration of AA, while Br⁻ ions slow down the reduction of Au (I). Additionally, it is believed that Br⁻ ions from the CTAB surfactant, can influence the shape of the NCs by selectively adsorbing on the {100} crystal facet and directing the deposition of Au ions on the other available crystal facets.^{52, 106}

Seed-mediated growth method has fairly low reproducibility for fabricating polyhedral NCs. The quality of NCs varies drastically from one research group to another, as well as chemicals from different companies or even different batch numbers from the same company.¹⁰⁷ For example, Korgel *et al.*¹⁰⁸ reported that the yield of Au nanorods varied depending on the CTAB used. Based on their findings CTAB might contain iodide impurities which negatively impact the yield of Au nanorods. Iodide ions could slow down the Au deposition rate and absorption onto Au {100} facets, preventing Au nanorods growth. Nevertheless, the low reproducibility for fabricating polyhedral NCs is largely due to the lack of sufficient understanding of i) the chemical reactions that drives nucleation, ii) the thermodynamic and kinetic process that influence NCs growth process, and iii) the synergic association between nucleation and growth process. Therefore, there is an urgent need for a better understanding of the exact role of each reagent and the associated reaction mechanism, in order to produce high quality shaped Au NCs in a reproducible, reliable and scalable manner.

This Chapter describes a systematic analysis of the one-pot synthesis method reported by Han and Yu *et al.*^{57, 109} I investigated the effect of reaction temperature and Au(I) ion stability as possible factors that might influence the shape of NCs.

Additionally, using UV-Vis and ^1H NMR spectroscopy techniques, I evaluated the stability and interaction of the molecular species formed in the three stages: 1) Formation of $[\text{AuBr}_4]^-$ complex, 2) Reduction of $[\text{AuBr}_4]^-$ complex with AA, and 3) Nucleation with different salts and bases. Our results suggest that during the Au reduction step an intermediate complex is formed, affecting the nucleation rate. We propose a mechanism of substitution in $[\text{AuBr}_4]^-$ complex by AA to reduce Au from (III) to (I). The findings in this study will provide guidance for the development of more simple, reliable methods to control the shapes of the NCs.

2.2. Experimental Methods

2.2.1. Materials

Gold (III) chloride trihydrate ($\text{HAuCl}_4 \cdot 3\text{H}_2\text{O}$, 99.99%+), hexadecyltrimethylammonium bromide (CTAB, 99%+), L-ascorbic acid (AA, 99%+), hexadecyltrimethylammonium chloride (CTAC, 99%+), sodium hydroxide (NaOH , $\geq 98\%$) dimethylsulfoxide- d_6 anhydrous, (DMSO-d_6 99.9%). All the chemicals listed above were used as received without further processing. Deionized water (Millipore Milli-Q grade) with resistivity of $18.0 \text{ M}\Omega$ was used in all aqueous experiments.

2.2.2. Synthesis of Au Cubes, Octahedrons and Cuboctahedrons

In a 20 mL vial, 19.75 mL solution of 10 mM CTAB was prepared in water, and placed in a water bath at 42°C . When the temperature of CTAB solution stabilized, 250 μL of 10 mM HAuCl_4 was added and stirred at 550 rpm for 30 seconds to obtain a transparent-yellow solution. Subsequently, 100 μL of 100 mM

AA was added, under stirring for 30 seconds, to form a colorless solution. The (Au-CTAB)-AA solution was kept steady (i.e. incubated at constant temperature and without stirring) for 0-5 minutes. Then, 100 μ L of 100 mM NaOH aqueous solution was quickly added under stirring at 550 rpm, for 2 minutes. The solution turned fuchsia in color in approximately 20-30 seconds, indicating the nucleation and formation of *Au cuboctahedrons*. *Au cuboctahedrons* were obtained by incubating the reaction in a water bath at 42 $^{\circ}$ C without stirring for 2 hours. The production of Au cubes and octahedrons was achieved by controlling incubation time of (Au-CTAB)-AA solution and the reaction temperature. Specifically, *Au cubes* were obtained by incubating the (Au-CTAB)-AA solution at 42 $^{\circ}$ C, for 10-15 minutes before the addition of NaOH, while all other experimental conditions were the same as described above. *Au octahedrons* were synthesized by elevating the reaction temperature to 50 $^{\circ}$ C, while all other experimental conditions were the same as the synthesis of Au cuboctahedrons. After the formation of desired Au NCs, the solution was centrifuged at 3,000 rpm and the precipitate were dispersed in deionized water, to remove excess precursors and hence stop the further proceeding of the reaction. Table 2-1 shows the mole equivalents of the reagents used in the synthesis of Au polyhedral NCs.

Table 2-1. Reagents for one-pot synthesis of Au polyhedral NCs.

	Metal Precursor	Reducing Agent	Nucleation Agent	Capping Agent/ Surfactant
Reagents	HAuCl ₄	C ₆ H ₈ O ₆ AA	NaOH	CH ₃ (CH ₂) ₁₅ N (Br)(CH ₃) ₃ CTAB
Molarity	10mM	100mM	100mM	10mM
Moles	2.5x10 ⁻⁶	1.0 x10 ⁻⁵	1.0 x 10 ⁻⁵	1.98 x10 ⁻⁴
Mole Equivalents	1	4	4	80

2.2.3. Formation of [AuBr₄]⁻ Complex

Au-CTAB solution was prepared by mixing 19.75 mL of 10 mM CTAB and 250 μ L of 10 mM HAuCl₄. UV-Vis spectrometry was used to identify the molecular species present in the (Au-CTAB) solution.

2.2.4. Reduction of [AuBr₄]⁻ Complex with AA

Utilizing UV-Vis spectrometry, (Au-CTAB)-AA solutions of different mole equivalent ratio of Au and AA were analyzed. Au-CTAB solution was prepared by mixing 19.75 mL of 10 mM CTAB and 250 μ L of 10 mM HAuCl₄. Then 12.5, 18.5, 25, 37.5, 50, 75, and 100 μ L of 100 mM AA were added into the Au-CTAB solution to prepare solutions with 1:1/2, 1:3/4, 1:1, 1:2, 1:3, and 1:4 ratio of Au and AA mole equivalent, respectively.

¹H NMR, HSQC, COSY experiments were conducted to analyze [AuBr₄]⁻ complex reduction with 1:1 and 1:4 mole equivalent ratio of Au and AA. [AuBr₄]⁻ complex was prepared by combining 22.4 mg of HAuCl₄ and 22.6 mg of NaBr in 0.5 mL of DMSO. Then, 10.7 mg and of AA was dissolved in 0.5 mL of DMSO. The [AuBr₄]⁻ complex solution and AA were mixed and analyzed.

2.2.5. Nucleation with Different Salts and Bases

Nucleation was studied by evaluating the effect of different salts and bases as reactants to induce nucleation in the (Au-CTAB)-AA solution. The (Au-CTAB)-AA solution was prepared by placing a vial containing 19.75 mL of 10 mM CTAB in a 42 °C water bath and adding 250 µL of 10 mM HAuCl₄. Au-CTAB solution was stirred at 550 rpm for 30 seconds; then, 100 µL of 100 mM AA were added. After 5 minutes of incubation, the solution was stirred at 550 rpm and 100 µL of 100 mM of the following salts and bases KOH, K₂CO₃, NaHCO₃, Na₂CO₃, NaCl, NaCN, NaI, C₂H₃NaO₂Na, and KCl) were added. The pH of each solution was measured, and the time taken for the solution to change color was recorded.

2.2.6. Characterization

The morphology of the NCs was evaluated by means of SEM Hitachi SU-70 Schottky Field Emission Gun Scanning Electron Microscope (FEG-SEM). The molecular species during [AuBr₄]⁻ complex reduction were analyzed by means of PerkinElmer Lambda 40 UV/VIS spectrometer and Bruker AVIII- 600 MHz NMR.

2.3. Results and Discussion

The one-pot synthesis of Au polyhedral NCs was evaluated to identify the key factors that influence the shape of NCs. Specifically, it was investigated the effect of: i) reaction temperature, ii) the formation of [AuBr₄]⁻ complex, iii) reduction of [AuBr₄]⁻ complex with AA, iv) nucleation of NCs with different salts and bases, and v) Au(I) ions incubation time.

2.3.1. The Effect of Temperature on Shape Transformation of Nanocrystals

The one-pot synthesis method allows for control over the morphology of NCs by adjusting the reaction temperature. It was found that the reaction temperature had a direct effect over the nucleation rate, thus leading to the production of Au octahedrons at 50 °C, Au cuboctahedrons and cubes at 42 °C, and irregular Au structures at 30 °C (Figure 2-2). The average length of Au octahedrons, cuboctahedrons, and cubes are 57.3 ± 4.4 , 67.5 ± 3.1 and 71.5 ± 3.7 nm, respectively.

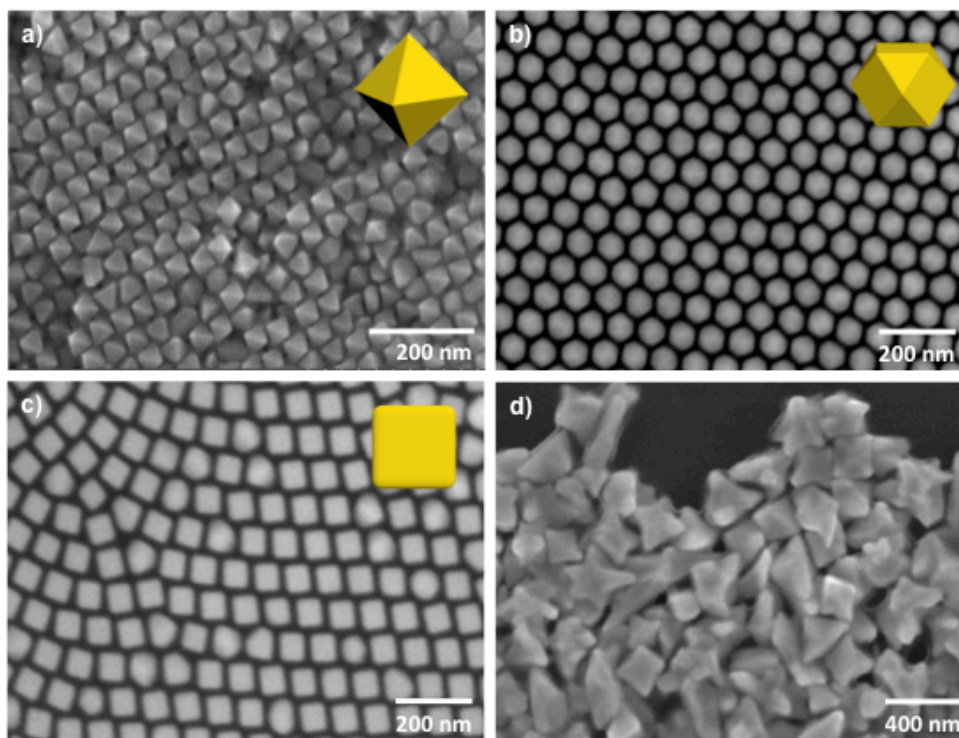






Figure 2-2. SEM images of the Au polyhedrons obtained at different reaction temperatures: a) 50°C, octahedrons; b) 42°C, cuboctahedrons; c) 42°C, cubes, and d) 30 °C, irregular shapes.

In this one-pot synthesis, NaOH is added to initiate nucleation to form NC seeds, after the reduction of HAuCl_4 by AA in presence of CTAB (Experimental conditions can be found in section 2.2.2). This method relies on a precise control of the reaction temperature to achieve an effective homogeneous nucleation. The

nucleation process was assessed by recording the time taken by the solution to change in color from colorless to pink and purple upon the addition of NaOH. It was found that as the reaction temperature increased from 30 to 42 to 50 °C, the nucleation rate increased from 360 to 90 to 50, and eventually to 20 seconds, as reflected by the more rapid color change in the solution (Table 2-2).

Table 2-2. The effect of reaction temperature on the onset of nucleation and the shape of corresponding NCs synthesized.

Nanocrystals Morphology	Reaction Temperature	Nucleation Time	Solution color
Octahedrons	50 °C	10-20 sec	
Cuboctahedrons	42 °C	30-50 sec	
Cubes	42 °C	60-90 sec	
Amorphous	30 °C	360 sec	

A rate of nucleation equation derived from Arrhenius equation is given as (Equation 2.1):

$$N = A \cdot \exp \left[- \frac{16\pi\sigma^3 M^2}{3R^3T^3\rho^2 (\ln S)^2} \right] \quad (\text{Eq. 2.1})$$

Where A is a constant of proportionality. M is molecular weight of metal precursor, S the degree of supersaturation of metal precursor ions, σ surface energy, R the gas constant, ρ density, and T the absolute temperature. This equation clearly states that the three main variables affecting the nucleation rate are: temperature, degree of saturation, and interfacial tension. It is inferred that temperature is the main factor that affects the morphology of NCs by influencing the nucleation rate of polyhedral NCs in our system.

2.3.2. Formation of $[\text{AuBr}_4]^-$ Complex

When HAuCl_4 is added to the CTAB solution (i.e., Au-CTAB solution), Br^- ions substitute the four Cl^- from HAuCl_4 to produce $[\text{AuBr}_4]^-$ complex¹¹⁰⁻¹¹¹. The stability for tetrahaloaurates (III) increases as follows $\text{Cl} > \text{Br} > \text{I}$. Recent studies have confirmed the presence of $[\text{AuBr}_4]^-$ complexes in Au growth solution by means of UV-Vis spectrometer and X-ray absorption near-edge structure (XANES)¹¹²⁻¹¹³. $[\text{AuBr}_4]^-$ is a square-planar complex ion. It has an absorption band at 395nm, which gives the transparent-yellow color to the Au-CTAB solution (Figure 2-3). A full UV-Vis spectrum of Au-CTAB solution reveals two more absorption bands located at 219 and 260 nm.

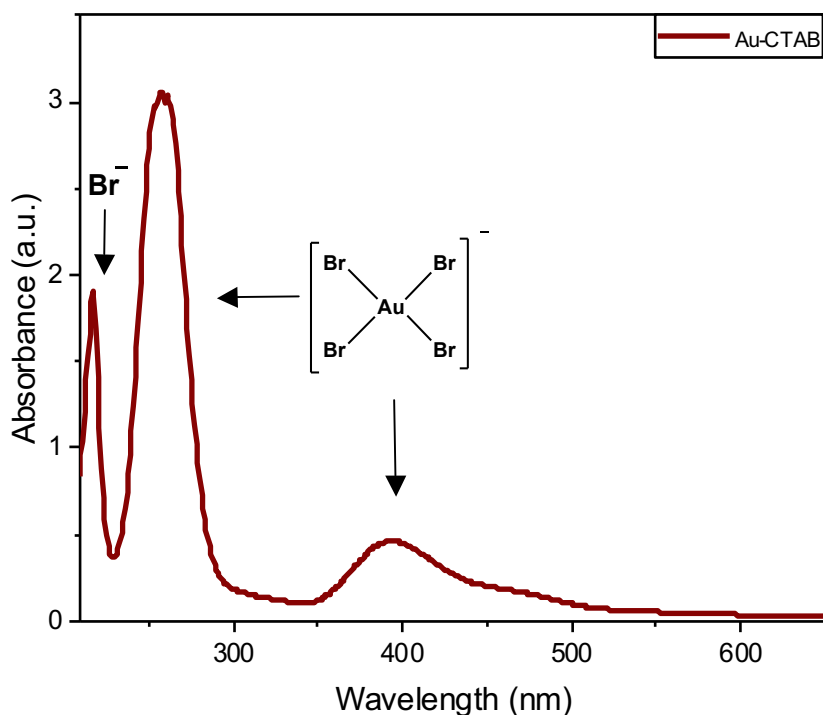
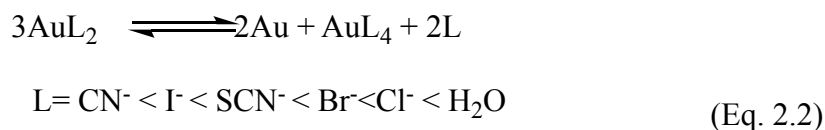


Figure 2-3. UV-Vis spectrum of Au-CTAB solution, the first step of the Au NC synthesis, showing the 395 nm and 260 nm absorption bands of $[\text{AuBr}_4]^-$ complex and the 219 nm absorption band of excess of Br^- ions.

The UV-Vis band at 219 nm corresponds to the excess of Br^- ions. As shown in Table 2-1, Au is 1:80 mole equivalent with respect to CTAB. The absorption of Br^- ions at 219 nm was experimentally confirmed by comparing the UV-Vis spectra of the following three solutions: Au-CTAB, KBr, and CTAC. The UV-Vis spectra of both Au-CTAB and KBr solutions showed the same absorption band at 219 nm, while UV-Vis spectrum of CTAC did not have any absorption over all wavelengths (Appendix A.1.).

The absorption band at 260 nm could be associated with either $[\text{AuBr}_4]^-$ or $[\text{AuBr}_2]^-$. Metal ligand coordination compounds such as $[\text{AuBr}_x]^-$ exhibit strong charge transfer absorption in the ultraviolet and visible region. The transfer of

electrons from ligand to metal molecular orbitals, or vice versa is known as ligand to metal charge transfer (LMCT) or charge transfer to metal¹¹⁴ (CTTM). Tetrahaloaurates (III) electronic spectra can have one or two weak and low energy bands, as well as one high energy band corresponding to LMCT.¹¹⁵⁻¹¹⁶ It has been theoretically reported that $[\text{AuBr}_2]^-$ could have a high energy band due to the low oxidation state of Au(I). However, $[\text{AuBr}_2]^-$ complex is unstable. In aqueous solutions, AuL_2 compounds (i.e., Au(I) with ligands (L)) is subjected to disproportionation (Eq. 2.2) depending on the type of ligands¹¹⁵.



To examine whether the 260 nm absorption band originated from $[\text{AuBr}_2]^-$ complex, the UV-Vis spectra of 1:2 mole equivalent of HAuCl_4 and KBr solution was analyzed. The UV-Vis spectra of the as-prepared solution showed a 243 nm absorption band and a shoulder absorption band near 350 nm (Appendix A.2.). Thus, the result was not sufficient to support that the 260 nm absorption band corresponded to $[\text{AuBr}_2]^-$ complex. Under this premise, it is assumed that $[\text{AuBr}_4]^-$ is the only complex formed in the Au-CTAB solution. The 260 nm and 395 nm UV-Vis absorption bands might come from $[\text{AuBr}_4]^-$ complex.

2.3.3. Reduction of $[\text{AuBr}_4]^-$ Complex with AA

Previous studies suggest that Au NCs are obtained through a reduction of Au ions from Au(III) to Au(I) via a simple redox reaction of $[\text{AuBr}_4]^-$ with AA. Nevertheless, it was hypothesized that AA could form a complex with Au ions through a mechanism of substitution. This could be possible because studies

involving chemical reaction of AA have shown that AA forms chelates with Cu¹¹⁷⁻¹¹⁸, Fe¹¹⁹⁻¹²⁰, Pt¹²¹⁻¹²³, and Ru¹²⁴. Also, reduced metal ions are often surrounded by shields of ligands. Specifically, Au is bound to ligands to prevents Au disproportionation^{57, 125-126}.

To monitor $[\text{AuBr}_4]^-$ reduction, series of $[\text{AuBr}_4]^-$ reductions with different mole equivalent ratios of AA and $[\text{AuBr}_4]^-$ were conducted. They were analyzed via UV-Vis and ¹H NMR spectroscopy techniques. The UV-Vis analysis of the reduction of $[\text{AuBr}_4]^-$ indicated that one mole of AA reduced completely $[\text{AuBr}_4]^-$ complex as the LMCT band from Au-Br bonds vanished. Figure 2-4 shows that both LMCT bands (i.e. 260 and 395 nm) gradually decreased and eventually vanished by increasing the Au to AA mole equivalent ratio from 1:1/2, to 1:1. Additionally, the results suggested that the band at 246 nm is excess of AA. (Figure 2-4b) shows that as the number of AA mole equivalents increased from 1:2 to 1:4, the 246 nm band emerged and its absorption intensity increased.

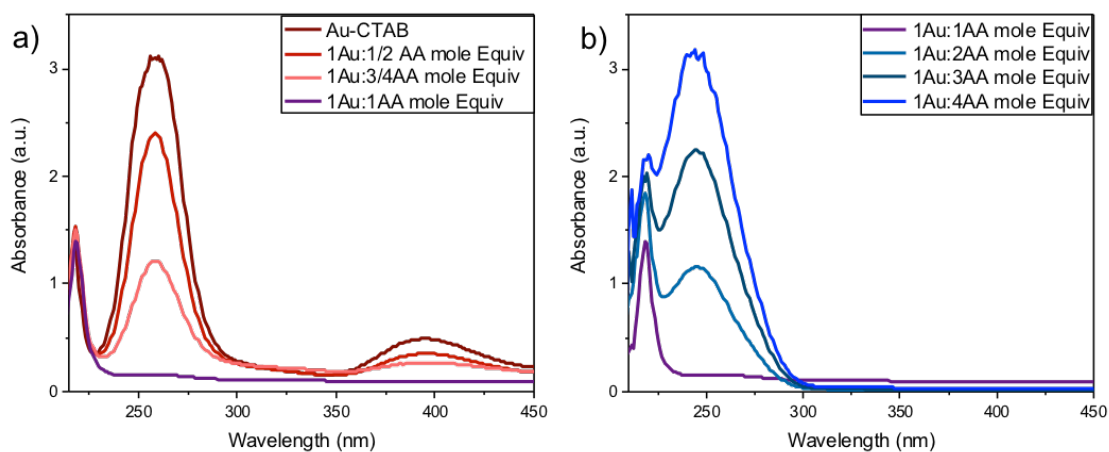


Figure 2-4. UV-Vis spectra of (Au-CTAB)-AA solution showing the reduction of $[\text{AuBr}_4]^-$ complex with different mole ratio of Au and AA a) 0:1, 1:1/2, 1:3/4, 1:1 mole equivalent, and b) 1:1, 1:2, 1:3, 1:4 mole equivalent.

Additionally, the UV absorption of 1:4 mole ratio of Au and AA solution was monitored over time at 42 °C. The 246 nm absorption band corresponding to AA in excess decreased over time (Figure 2-5). This implies that after Au is reduced, excess of AA present in the (Au-CTAB)-AA solution is still reacting with other molecular species in excess (e.g., Br⁻, and Cl⁻ ions) in the solution. Therefore, 1:4 mole equivalent of Au and AA are necessary to obtain monodisperse Au polyhedral NCs (Appendix A.3).

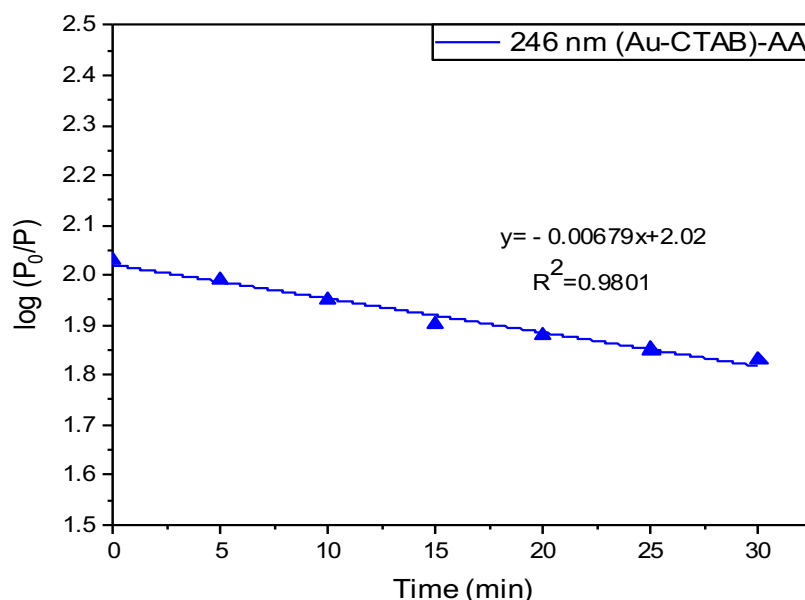


Figure 2-5. UV-Vis absorbance plot of (Au-CTAB)-AA solution as a function of incubation time, showing the slow oxidation of unreacted AA over time in the solution.

Based on the analysis of ¹H and ¹³C NMR spectra for pristine AA and a solution of 1:1 mole equivalent of [AuBr₄]⁻ and AA, three intermediate complex structures are proposed in Figure 2-6. In presence of Au, AA protons have different chemical shifts and signal splitting suggesting that Au is attached to AA molecule exposing the protons to different chemical environment.

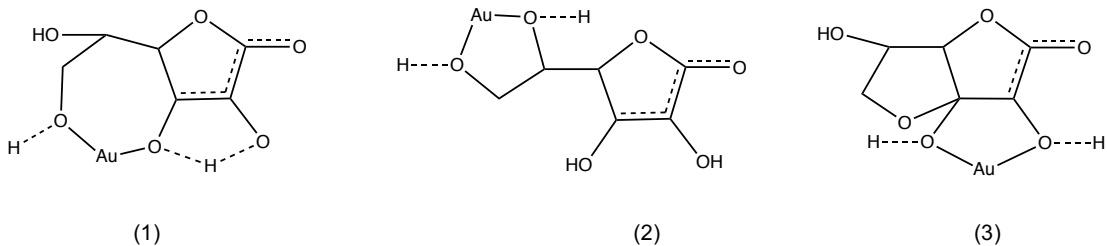


Figure 2-6. Proposed structure of the Au-AA complex formed during the $[\text{AuBr}_4]^-$ reduction with AA.

Figure 2.7 shows that the magnetic field of ^4H in AA is affected by magnetic moment of ^5H , the proton on the adjacent carbon, causing a signal splitting into doublet, δ 4.7. However, ^4H signal δ 4.4 is a singlet in presence of Au, because it not affected by ^5H magnetic moment. This suggests that there is a carbon rotation restriction due to the formation of a ring, which separates ^4H and ^5H protons from each other, inhibiting the magnetic moment of ^5H . Other change in signal splitting occurs for the two ^6H from AA. These protons are normally equivalent protons. They have the same chemical shift and their signal splitting is a multiplet; however, when Au is present in AA solution, the ^6H signal showed two different chemical shifts δ 3.8 and 4.1 ppm with splitting patterns, double of double and triplet, respectively. This indicates that the two ^6H signals are not equivalent anymore. They experience different chemical environment, likely due to a ring formation, suggesting that Au might be attached to the OH bonded to carbon 6. In presence of Au, proton ^5H in AA, experiences a down field chemical shift from δ 3.7 to 4.2 ppm. It preserves its triplet signal splitting partner with and without Au. In the absence of Au, the magnetic field of proton ^5H is affected by the magnetic moment of ^4H ; but when Au is present, ^5H is affected by the magnetic moment of one ^6H also, due to the formation of a ring

structure with Au. Correlation Spectroscopy, COSY, further confirms the ^1H - ^1H connectivity between the protons of Au-AA complex (Appendix A.4.).

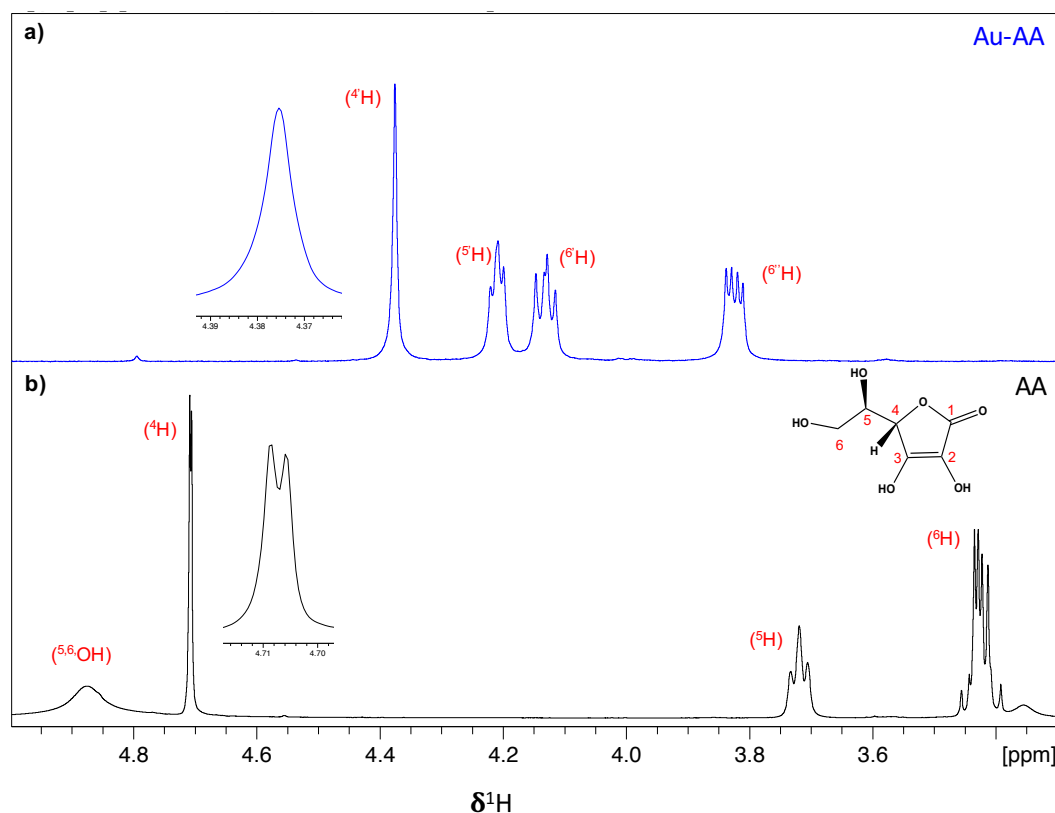


Figure 2-7. ^1H NMR spectrum of a) gold and L-ascorbic acid 1:1 mole equivalent (Au-AA) and b) pristine L-ascorbic acid (AA) showing the signal splitting.

In the ^1H NMR spectra of the Au-AA complex, it was observed that AA hydroxyl groups ^3OH and ^2OH with chemical shift (δ) 8.3 and 11.0 ppm vanished, indicating that the hydroxyl groups could be deprotonated or bounded to Au (Appendix A.5. shows the ^1H NMR full spectrum). ^{13}C NMR spectra of Au-AA sample shows that there is only one carbonyl signal, δ 171.6 corresponding to ^{13}C from AA. Since dehydroascorbic acid structure has three carbonyls, this result disregards the possibility that AA was oxidized and formed dehydroascorbic acid (Appendix A.6).

To confirm proton assignment and elucidate the structure of Au-AA complex, heteronuclear single quantum coherence spectroscopy (^1H - ^{13}C HSQC) of Au-AA complex was analyzed. ^1H - ^{13}C HSQC of Au-AA complex (Figure 2-8) shows that ^6C of Au-AA, δ 75.3 ppm, correlates with two proton signals $6''\text{H}$ and $6'\text{H}$ corresponding to δ 3.82, 4.13 ppm, respectively. Additionally, ^4C , and ^5C with chemical shift, δ 88.3 and δ 73.7 ppm, correlate with one single proton, δ 4.21, and 4.38 ppm, respectively. HSQC of AA demonstrates that carbon 4,5,6 individually correlate with only one ^1H signal (Appendix A.7.).

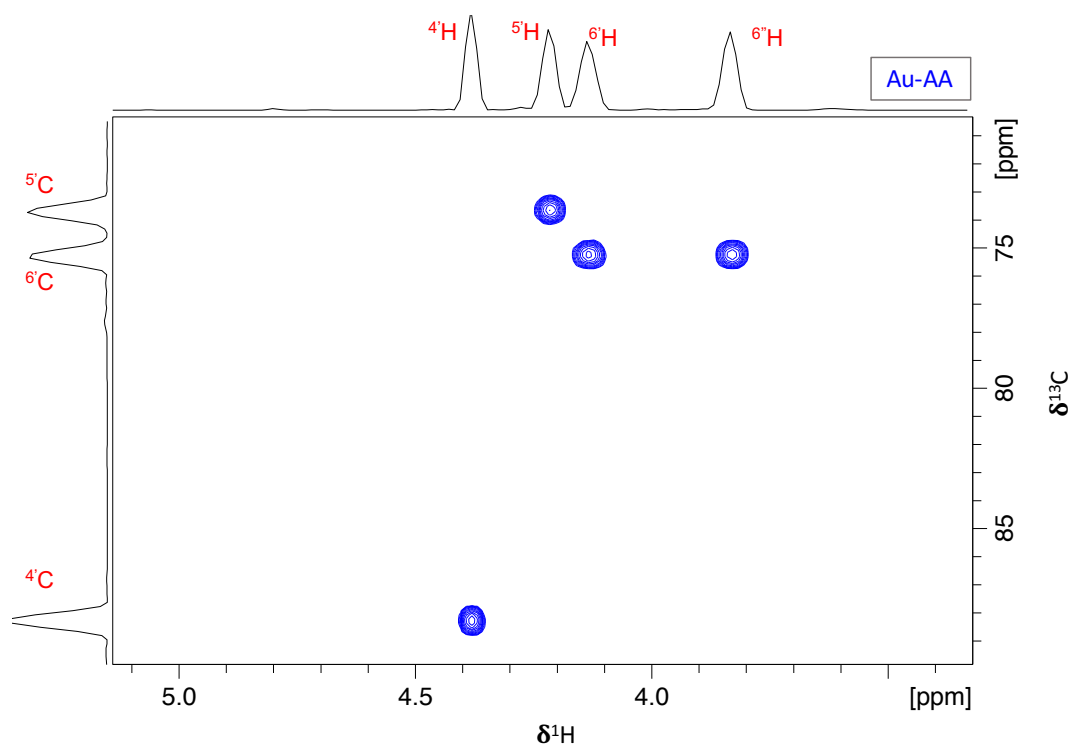


Figure 2-8. ^1H - ^{13}C HSQC spectrum of Au-AA showing the carbon signal correlation with proton signal. The spectrum indicates that carbon 6 has two protons with different chemical shifts.

2.3.4. Nucleation with Different Bases and Salts

In the one-pot synthesis of Au polyhedrons, nucleation is initiated by adding aqueous solution of NaOH into the (Au-CTAB)-AA solution. It was believed that the

addition of NaOH increases the pH of the solution and increases the reduction capability.¹²⁷⁻¹²⁹ To understand the role of NaOH, we evaluated the effect of different salts and bases as nucleation agent to produce NC seeds (Table 2-3). We found that nucleation only occurred when strong or medium bases such as NaOH, KOH, K₂CO₃ were used.

Table 2-3. List of nucleophile used to induce nucleation.

Nucleation Agent	pKa	Nucleation
OH ⁻	15.7	✓
CO ₃ ⁻²	10.2	✓
CN ⁻	9.1	✗
HCO ₃ ⁻¹	6.35	✗
CH ₃ CO ₂ ⁻	4.75	✗
Cl ⁻	-7	✗
I ⁻	-10	✗

KOH and NaOH triggers the occurrence or onset of nucleation within 30-60 seconds, while K₂CO₃ induce nucleation in 2 hours (i.e. solution turned from colorless to pink in color). Other bases like NaHCO₃, CH₃CO₂Na did not trigger nucleation at any point during the reaction. We believe that NaOH as strong Lewis Base can deprotonate Au-AA complex liberating Au in the form of Au(0) to form the first NC seeds.

Because nucleophilicity and basicity are correlated, we investigated the effect of OH⁻ as nucleophile by testing strong nucleophiles with low pK_a values such as NaCN, and NaI. When strong NaCN and NaI were used, no nucleation was observed. The results indicate that nucleation might be driven by pK_a value of the nucleation agent. Hydroxide ions are a stronger base than cyanide ions; therefore, hydroxide ions have a greater affinity to seek protons from the Au-AA complex thus inducing nucleation.

2.3.5. Au(I) Ions Incubation Time

In accordance with equation 2.1., supersaturation of Au (I) ions prior the nucleation is a key factor that affects the morphology of NCs. It was predicted that nucleation initiates when NaOH is added at the precise moment that Au-AA complex concentration has reached its critical threshold. Nucleation slows down or does not take place as (Au-CTAB)-AA solution incubation time is prolonged. In section 2.3.2, it was described that when the Au ion solution was incubated at 42 °C for 5 and 10 minutes, Au cuboctahedrons and cubes were produced, respectively. Their nucleation rate slowed down from 30 to 90 seconds. Further experiments show the same trend, when Au ion solution was incubated at 42 °C from 10 to 20 minutes, the nucleation rate changed from 60 to 120 seconds, respectively. Au cubes increased in size from 125.1 ± 6.3 to 140.7 ± 7.6 nm in diagonal length, respectively. However, the quality of the cubes decreased as the nucleation is slowed down. Finally, when Au ion solution was incubated for 30-35 minutes, nucleation is constrained, irregular Au nanostructures with a length of approximately 434.7 ± 84.3 nm were produced in lack of nucleation. (Figure 2-9).

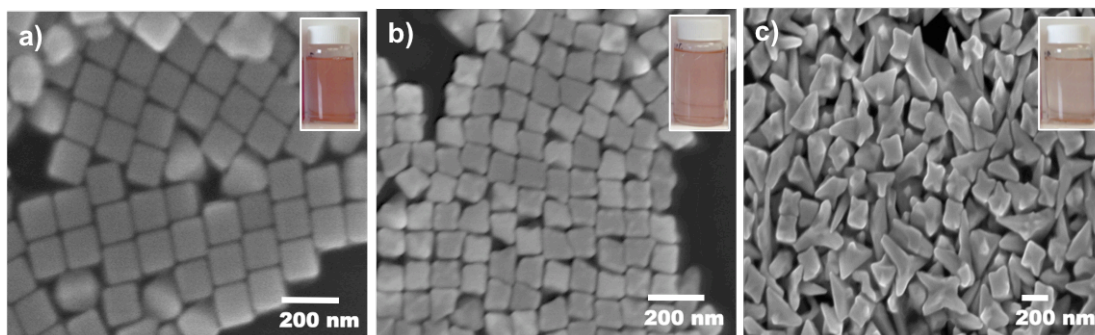


Figure 2-9. SEM images of nanostructures obtained in one-pot synthesis, when (Au-CTAB)-AA solution was incubated at different periods of time a) 10-15 minutes b) 20-25 minutes, and d) 30-35 minutes.

These results suggest that Au-AA complex could degrade over time decreasing the concentration of Au(I) and subsequently slowing down or inhibiting the nucleation. This prediction can be supported by LaMer nucleation theory which states that nucleation takes place when the concentration of the metal precursor reaches saturation point⁴³. The results indicate that in one pot synthesis of Au NCs, the two experimental parameters that affect the morphology of NCs are the reaction temperature and the incubation time of Au (I) ion solution.

2.4 Conclusion

The study of one- pot synthesis to fabricate Au polyhedral NCs indicates that the morphology of NCs is determined by the nucleation rate through the control of reaction temperature and the (Au-CTAB)-AA incubation time. The UV-Vis analysis of the reduction of $[\text{AuBr}_4]^-$ indicated that one mole of AA reduced $[\text{AuBr}_4]^-$ complex as the LMCT band from Au-Br bonds vanished. ^1H and ^{13}C NMR spectra of pristine AA and Au-AA solution provided insights of the possible formation of Au-AA intermediate complex during the reduction of $[\text{AuBr}_4]^-$ with AA. It is believed Au

forms a complex with two oxygen-donor ligand from AA, which minimizes Au(I) disproportionation. It is predicted that nucleation takes place when strong base such as NaOH deprotonates the Au-AA complex detaching Au from AA to form Au(0) seeds.

The nucleation can be altered when Au (I) solution incubation time is prolonged causing a degradation of the Au-AA complex and therefore decreasing the critical supersaturation concentration of Au (I) ions. Based on the UV-VIS analysis of $[\text{AuBr}_4]^-$ reduction in excess of AA, it was determined that three extra moles of unreacted AA had a positive effect in the production of high quality of Au cubic NCs. We presume that the excess of AA provides stability to Au-AA complex, as there is excess of Br^- ions from CTAB competing with AA to coordinate with Au.

For future work, it is important to analyze the effect of the Br^- ions in the Au reduction and nucleation stage of the synthesis. Any side reaction due to the excess of reactive species such as Br^- ions and AA, could be minimized or eliminated to increase the reproducibility of the synthesis and design optimal protocols to synthesis polyhedral NCs.

Chapter 3: Immobilized Seed-mediated Growth of Two Dimensional Array of Au Octahedrons with Defined Orientations

“ Our greatest weakness lies in giving up.
The most certain way to succeed is
always to try just one more time.:

Thomas Edison

3.1. Introduction

Noble metal NPs (e.g., Au, Ag, and Pd) exhibit fascinating optical, electronic, and catalytic properties that are strongly dependent on their size, shape, and composition.^{3, 50} Successful implementation of these NPs into functional devices usually requires effective control of their spatial arrangement and orientation on substrates.^{62, 74, 130-132} The organization of metallic NPs on substrates allows utilizing and modulating the collective optical and electronic properties of NP arrays, thus facilitating their applications in photovoltaic devices,¹⁶⁻¹⁷ data storage,^{61, 133} catalysis,¹³⁴⁻¹³⁵ and biological and chemical sensors.¹³⁶⁻¹³⁸ As an example, one- or two-dimensional (1D or 2D) arrays of plasmonic nanostructures (e.g., Au nanorods) can be used to manipulate or concentrate light with wavelength below the diffraction limit.¹³⁹⁻¹⁴¹ In this case, the energy transportation in the array is strongly dependent on the relatively position and orientation of plasmonic NPs.

Self-assembly of NPs has been widely studied for the fabrication of arrays of NPs with different shapes (e.g., spheres, cubes, and rods) on substrates.^{72, 88, 142-144} One common strategy is to use interfaces (e.g., air/liquid, liquid/liquid, liquid/solid) to guide the spontaneous organization of NPs into ordered structures directly or

indirectly on substrates.^{72, 88, 143-147} Unlike top-down approaches (e.g., electron beam lithography⁸³), self-assembly methods are simple, scalable, and do not require special instrumentation in the production of NP arrays. However, these bottom-up approaches usually offer limited control over the orientation of shaped NPs with respect to the substrate. One potential strategy to address this challenge is to grow arrays of oriented NPs directly from seeds immobilized on a substrate. Recently, Hajfathalian *et al.*¹⁴⁸⁻¹⁴⁹ reported the fabrication of 2D array of bimetallic core-shell nanostructures using seeds deposited by vapor phase assembly technique on substrates. In this work, the patterning of seed arrays requires the deposition of sacrificial layers and high temperature annealing (up to 1100 °C), which may limit the types of substrates and seed materials that can be used for the synthesis. Nevertheless, there is a need for a general approach to the fabrication of high quality substrate-supported arrays of shaped NPs.

I developed an immobilized seed-mediated growth method to fabricate 2D periodical arrays of Au NCs with defined shape and crystal orientations with respect to substrates. This method involves the self-assembly of polystyrene (PS)-grafted shaped Au NPs into 2D arrays on a substrate, oxygen plasma etching of polymer ligands to selectively expose the top surface of Au seeds, and subsequent deposition of Au ions onto the exposed Au surfaces through seed-mediated growth. The synthetic approach we developed presents an important addition to current tools for the fabrication of substrate-supported functional nanostructures as new materials and devices.

3.2. Experimental Methods

3.2.1. Materials

Gold (III) chloride trihydrate ($\text{HAuCl}_4 \cdot 3\text{H}_2\text{O}$, 99.99%+), Hexadecyltrimethylammonium bromide (CTAB, 99%+), L-ascorbic acid (AA, 99%+), tetrahydrofuran (THF) were purchased from Sigma-Aldrich. Thiol-terminated polystyrene (PS-SH, $M_n = 50,000$, PDI=1.09) was purchased from Polymer Source Inc. All the chemicals listed above were used as received without further processing. Deionized water (Millipore Milli-Q grade) with resistivity of 18.0 M Ω was used in all the experiments.

3.2.2. Surface Modification of Shaped Au Seeds

Using ligand exchange method,³⁹⁻⁴³ thiol-terminated polystyrene (PS-SH, $M_n = 50,000$) was grafted onto the surface of shaped Au NCs (Synthesis protocol for Au cuboctahedral, cubic, and octahedral seeds can be found in Chapter 2, section 2.2.2.). As-prepared shaped Au NCs were centrifuged twice at 2,500 - 3,000 rpm (1.5 mL centrifuge tubes are highly recommended). After the first and second centrifugation cycle, the NCs were redispersed and concentrated in 3 mL and in 200 μL of water, respectively. Then, 200 μL of shaped Au NCs were added dropwise into 10 mL of 0.075 mg/mL PS-SH solution in DMF under stirring. Subsequently, the solution was sonicated for 10 minutes and incubated for another 10 min at room temperature. The PS-grafted Au NCs solutions were centrifuged for ~3-4 cycles to remove excess PS. After each centrifugation cycle, the supernatant was discarded and PS-grafted NPs at the bottom were redispersed in 1.0 mL of THF. After the last centrifugation cycle,

PS-grafted Au shaped NCs were dispersed in 3 mL THF and stored at 4 °C for further use.

3.2.3. Self-assembly of Polystyrene-grafted Au Nanocrystals into 2D Arrays

Polystyrene-grafted Au NCs were directly assembled into 2D array onto Si wafer substrates. Square pieces of Si wafers ($\sim 2.5 \text{ cm}^2$ in size) were cleaned thoroughly with piranha solution, a mixture of 3:1 H_2SO_4 and 30% H_2O_2 (CAUTION: The mixing procedure is an exothermic reaction, which creates a highly CORROSIVE mixture. Refer to reliable SOP for piranha solution handling, and disposal procedures). The Si wafers were rinsed with copious amount of water and stored in water to avoid contamination from air. Si wafers were dried under Ar or N_2 gas and immediately used for self-assembly.

Monolayer arrays of Au NCs were fabricated by the self-assembly of PS-grafted Au NCs using method reported previously with appropriate modification.⁴⁴⁻⁴⁵ Briefly, clean Si wafers were placed on top of HPLC caps in a glass petri dish containing THF solvent. A 3 μL of PS-grafted Au shaped NCs solution in THF was quickly dropped on the surface of Si wafer. The petri dish was immediately covered with lid to create a close system saturated with THF vapor. The solution of PS-grafted Au seeds spread over the surface of the Si wafer. Upon the slow evaporation of THF solvent in the NC solution, the PS-grafted Au NCs self-organized into monolayer arrays with hexagonally packed NPs on the substrate.

3.2.4. Removal of Polystyrene from the Top Surface of Au Nanocrystals

The polystyrene on the top surface of Au NCs with arrays was removed with oxygen plasma etching. Prior oxygen plasma treatment, Si wafers with assembled NC arrays were rinsed with deionized water and dried by blowing air to remove contaminants. Afterwards, the arrays of shaped seeds were treated with oxygen plasma for three minutes under medium Radio Frequency power (RF) using Harrick Plasma Cleaner PDC-32 G (115V). The exposure time was adjusted according to the size of the Au NCs. PS-grafted Au cubes were etched between 3.5-4 minutes since their surface area was larger than cuboctahedrons surface area. The substrates with NC arrays were immediately rinsed with deionized water and stored in water for future use.

3.2.5. Au Deposition on Exposed Surface of Au Nanocrystals Arrays

The growth solution was first prepared as follows. In a 20 mL vial, specific quantity of 10 mM HAuCl_4 aqueous solution was added into a 19 ml of 10 mM CTAB solution. The solution was swirled for thorough mixing. *L*-Ascorbic acid was then added (1:1 Au to AA mole ratio) and mixed well until the color of solution turned from yellow to clear. Subsequently, the plasma-treated seed arrays on Si wafers were immersed in the Au growth solution and incubated in a water bath at different temperatures and specific periods of time. Tables A.8., A.9., and A.10. in Appendix show the detailed reaction conditions (e.g., temperature and quantities of HAuCl_4 and AA) to fabricate arrays composed of Au truncated octahedrons with $\langle 110 \rangle$, $\langle 100 \rangle$, and $\langle 111 \rangle$ orientation, respectively. After the completion of metal

deposition, the samples were removed from the growth solution and rinsed with deionized water.

3.2.6. Characterization

The morphologies of polyhedral NCs were imaged using a Hitachi SU-70 Schottky Field Emission Gun Scanning Electron Microscope (FEG-SEM). The side view SEM images of NC arrays were taken by placing the substrates on a 45° angle SEM stage and tilting the SEM stage as needed. Samples for bottom view SEM imaging were prepared as follows. A conductive tape was placed on the top of NC arrays on the substrate. A razorblade was used to gently and uniformly press the tape to stick onto the arrays. Subsequently, the tape was peeled off from the substrate and the NC arrays were transferred on the tape upside down. The arrays supported on the tape were transferred to a Si wafer and imaged normally under SEM.

3.3. Results and Discussion

The immobilized seed-mediated growth method for the fabrication of 2D arrays of polyhedral NCs with well-defined shapes and orientations on a substrate consisted of three main steps: 1) Self-assembly of polystyrene-grafted Au seeds to form highly ordered 2D arrays on a substrate, 2) Oxygen plasma etching of polystyrene from the top surface of Au seeds, and 3) Selective Au deposition on exposed surface of PS-grafted Au seed arrays (Figure 3-1). This method was used as a platform to systematically monitor and evaluate the shape evolution of Au seed NPs to final polyhedral NCs.

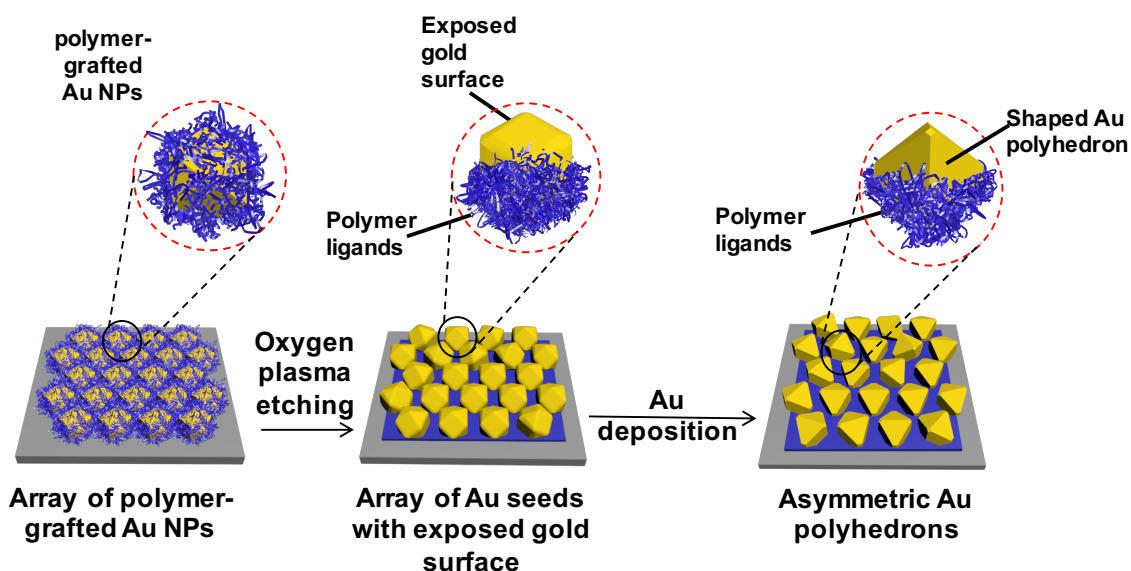


Figure 3-1. Schematic of immobilized seed-mediated growth method to fabricate 2D arrays of asymmetric NCs with specific orientation. This surface-initiated method includes the following steps: i) self-assembly of polymer-grafted Au NPs to form highly ordered arrays on a substrate. ii) selective removal of polymers on Au NPs to expose the top surface of NPs as seeds through oxygen plasma treatment. iii) selective growth of Au truncated octahedrons directly from the seed arrays on the substrate.

3.3.1. Self-assembly of Polystyrene-grafted Au Nanocrystals into 2D Arrays

Au seeds functionalized with PS-SH were assembled into a monolayer of hexagonal packing NP arrays driven by solvent-evaporation.¹⁵⁰ Briefly, a droplet of PS-grafted Au seeds in THF was deposited onto a clean silicon substrate (1.5 x 1.5 cm² in size). As the solution slowly evaporated, the PS-grafted Au seeds nucleated and self-organized into hexagonal packing monolayer arrays at the THF–air interface (Figure 3-2 & Appendix A.11.). The spacing between the Au seeds was controlled by the molecular weights (i.e. 5K, 12K, 50K) of PS-SH ligands functionalized on the surface of NPs. The average distance between the Au seeds increased from 8.3±4.2 to 21.8±5.1nm. The use of hydrophobic PS-SH allowed to: i) control the self-assembly of shaped Au seeds into 2D arrays, ii) modulate the distance between NPs within 2D

array, iii) immobilize the NPs on a substrate during the subsequent metal deposition, and iv) selectively protect the bottom-half surface of Au seeds for directional growth of metals.

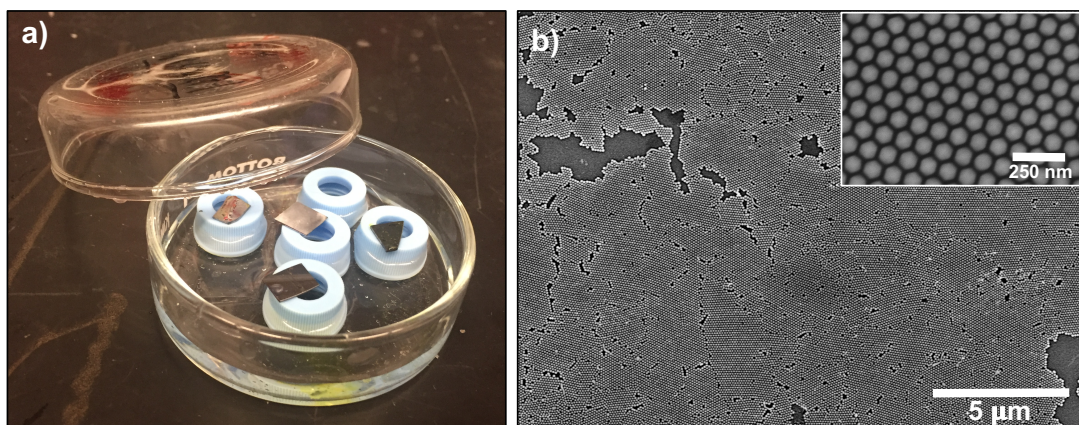


Figure 3-2. (a) Photo showing the set-up for the self-assembly of polystyrene-grafted Au seeds into 2D monolayer arrays. (b) Low magnification SEM image of 2D array of Au cuboctahedrons. Inset is the high magnification SEM image of 2D array of Au cuboctahedrons.

3.3.2. Removal of Polystyrene from the Top Surface of Au Nanocrystals

In order to use 2D array of shaped Au seeds for Au deposition, oxygen plasma was used to etch away polymer ligands on the top surface of the NP arrays. Oxygen plasma is a technique widely used for oxygen implantation, etching, and even for cleaning.¹⁵¹ When the monolayer array was treated with oxygen plasma, PS-grafted Au seeds were irradiated with atomic free oxygen radicals, which removed the polymer by oxidizing the polymer backbone and eventually the aromatic groups as well.¹⁵² To ensure the uniform deposition of metals to obtain NCs with well-defined shape, it was essential to control the oxygen plasma exposure time and power intensity. The oxygen plasma condition was optimized to remove the polymer just on the top surface of the NPs, while not deteriorating the monolayer film from the substrate. The required exposure time and power intensity were largely dependent on

the size of Au seeds and the molecular weight of PS-SH. For Au seed arrays without being treated with oxygen plasma, there is no uniform metal deposition, but only a small population of irregular metal islands on some of the seed NPs (Figure 3-3).

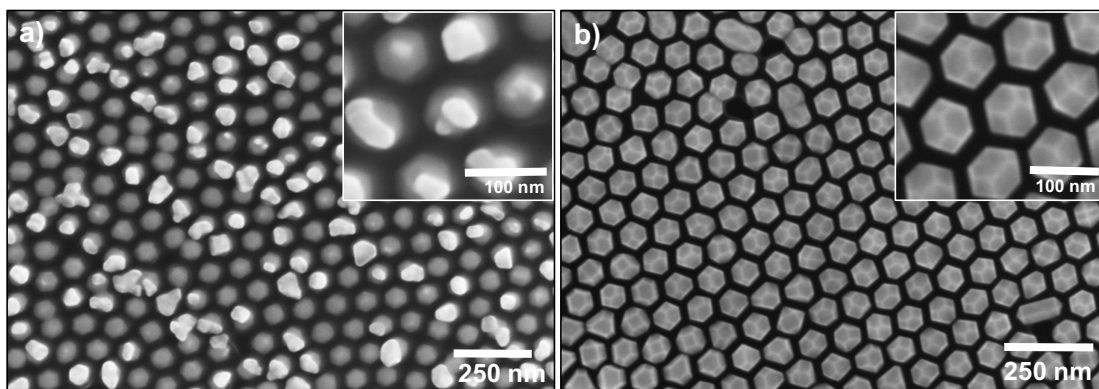


Figure 3-3. SEM image of 2D array of Au NPs after Au deposition using Au cuboctahedrons (a) without being treated with oxygen plasma and (b) being treated with oxygen plasma for 3 minutes. The Au deposition time is: 3 h for (a) and 10 h for (b).

3.3.3. Array of Truncated Octahedrons with $\langle 110 \rangle$ Orientation

The seed array of Au cuboctahedral seeds after plasma treatment was incubated in a growth solution containing Au precursor for metal deposition. After completion of the reaction, the NCs in the arrays transformed into monodispersed Au truncated octahedrons (Figure 3-4). With the successful shape transformation, the average diagonal length of NCs increased from 73.8 ± 3.9 nm to 92.1 ± 4.2 nm, while the average spacing between NPs decreased from 21.8 ± 5.0 nm to 16.7 ± 4.0 nm. The hexagonal packing of NCs was maintained after the metal deposition, which suggests that the seeds were immobilized on the substrate, owing to the residual hydrophobic PS collapsed on the bottom surface of NCs when the substrate was immersed in aqueous solutions.³⁶

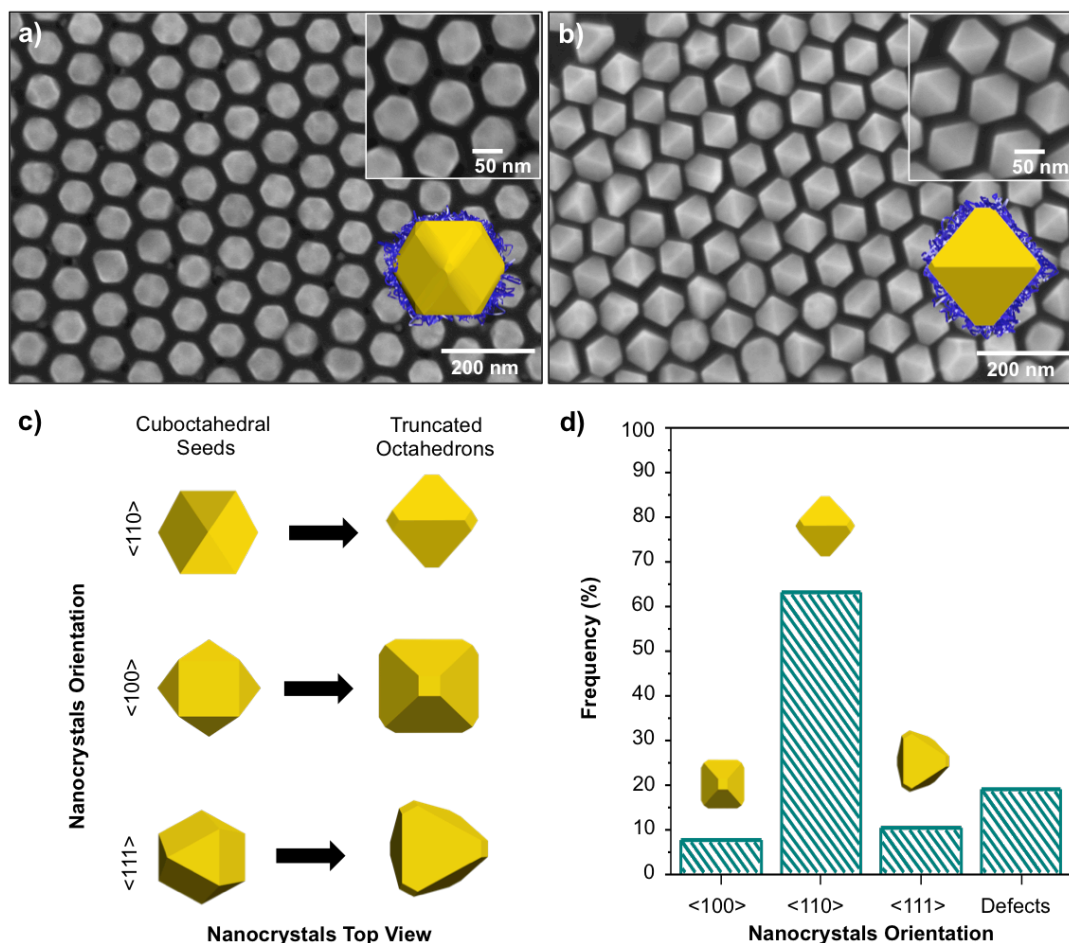


Figure 3-4. Top view SEM images of 2D array of (a) Au cuboctahedral seeds with $\langle 110 \rangle$ orientation with respect to the substrate (before Au deposition) and (b) Au truncated octahedrons with $\langle 110 \rangle$ orientation (after Au deposition). c) 3D models illustrating the shape transformation of Au cuboctahedral seeds with the $\langle 110 \rangle$, $\langle 100 \rangle$, $\langle 111 \rangle$ orientation. d) Histogram analysis of the orientation of resulting Au truncated octahedrons within the 2D array.

The uniform transformation of cuboctahedrons to truncated octahedrons can be attributed to the defined crystal facets and orientation of the Au cuboctahedral seeds on the substrate. Au cuboctahedrons had a preferential $\langle 110 \rangle$ orientation with respect to the substrate. At this orientation, four crystal facets (i.e., two $\{111\}$ and two $\{100\}$) at the top surface of NCs were exposed directly to oxygen plasma treatment, leading to the selective removal of PS ligands on the top surface of NCs. The efficient deposition of fresh Au on these four exposed crystal facets led to the

transformation of Au cuboctahedral seeds into truncated octahedrons with $\langle 110 \rangle$ orientation. Three dimensional (3D) models in Figure 3-4c illustrate the shape transformations of Au cuboctahedral seeds with different orientations (i.e., $\langle 110 \rangle$, $\langle 110 \rangle$, and $\langle 111 \rangle$ orientation) on the substrate. Quantitative analysis of NC orientation after growth indicates that 81% of the seeds transformed into truncated octahedrons, of which 63%, 7.6 %, and 10.4 % of the truncated octahedrons displays $\langle 110 \rangle$, $\langle 100 \rangle$, $\langle 111 \rangle$ orientation, respectively (Figure 3-4d). NPs with irregular shape represented 19% of total NPs within the array, which can be attributed to seed defects. It is worth noting that the formation of NCs with defined shapes did not occur using 15 nm seed NPs without defined crystal facets as shown in Figure 3-5.

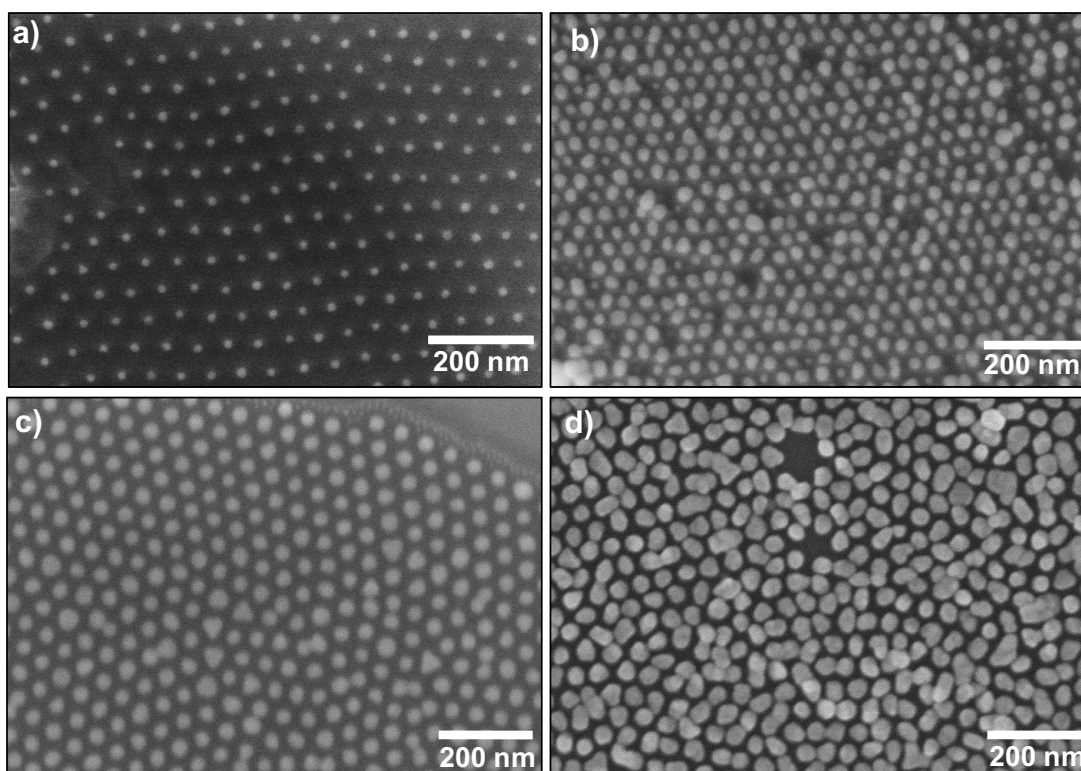


Figure 3-5. (a,b) Top view SEM image of 2D array of (a) 15 nm spherical Au seed NPs (before Au deposition) and (b) Au NPs with irregular shape (after Au deposition). (c,d) Top view SEM images of (c) 40 nm spherical Au seed NPs (before Au deposition) and (d) Au NPs with irregular shape (after Au deposition).

A close inspection of the side and bottom view of resulting truncated octahedron with $\langle 110 \rangle$ orientations indicates that the NCs acquire an asymmetric polyhedral geometry with respects to the top and bottom halves of NCs (Figure 3-6). While the top half of the NCs transformed into truncated octahedron shape, the bottom half retained their original cuboctahedral shape with a slight elongation of the two $\{111\}$ crystal facets. The NCs exhibit different appearances, depending on the rotation angle of the NPs (see 3D models of NCs viewed at different angles). As mentioned above, the presence of relatively low-density PS at the bottom surface of seeds helped to immobilize individual NCs and kept them fixed at their original position on the substrate, throughout the metal deposition process. More importantly, it significantly slowed down the deposition of metals at the bottom, while not affecting the growth from the top crystal facets. The differential growth rates on the top and bottom surfaces of seeds resulted in the formation of NCs with asymmetric shape.

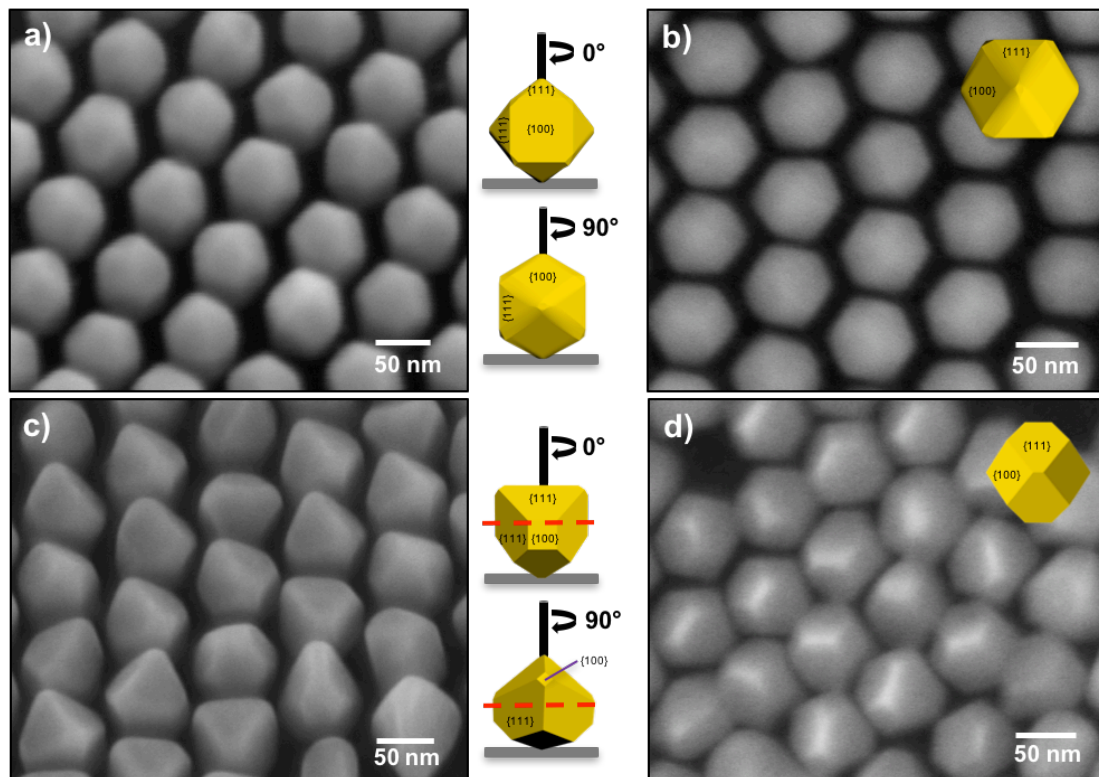


Figure 3-6. (a,c) Side view and (b,d) bottom view SEM images and their corresponding 3D models of (a,b) cuboctahedral seeds (before Au deposition) and (c,d) resulting asymmetrical truncated octahedron (after Au deposition).

The immobilized seed-mediated growth method offers us a simple way to systematically analyze the time-dependent shape evolution of NCs on the substrate. By imaging the NC arrays at different points in time of Au deposition, we witnessed the shape transformations of cuboctahedral seed arrays (Figure 3-7). Within ~2 hours of incubation, the Au cuboctahedral seeds preserved their original shape. After ~3-4 hours, the seeds transformed into truncated octahedrons in which the top {111} crystal facets increased in size while the {100} crystal facets decreased. With the extension of growth time, the {111} crystal facets continuously increased to dominate the top surface of NCs, while the size of {100} crystal facets kept reducing until they almost completely disappeared after ~8 hours of incubation. The controllable shape

transformation was further confirmed by the gradual increase in the diagonal length of NCs. The diagonal length of Au cuboctahedral seeds increased from 73.8 ± 3.9 nm, to 83.7 ± 5.6 nm, and eventually to 92.1 ± 4.2 nm at the aforementioned time points, respectively (Appendix A.12.).

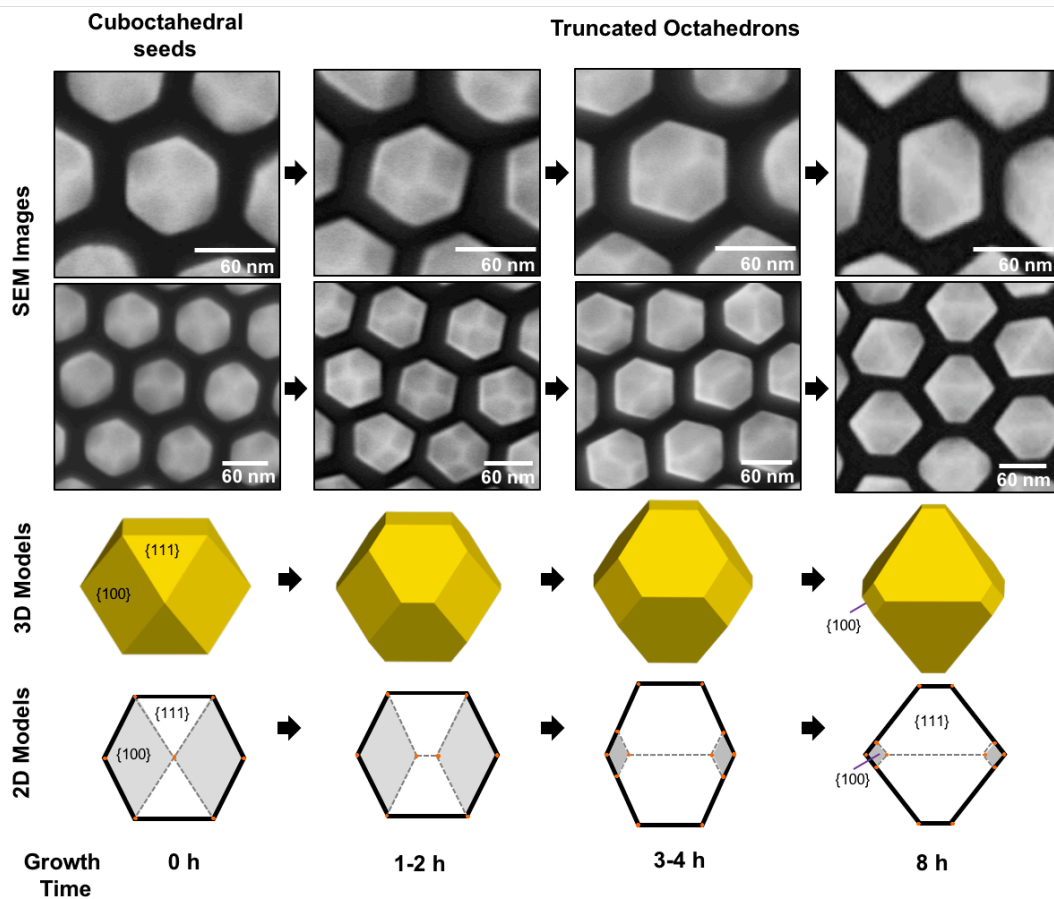


Figure 3-7. Top view SEM images, 3D, and 2D models illustrating the time-dependent shape evolution of Au cuboctahedral seeds along the $\langle 110 \rangle$ orientation.

3.3.4. Array of Au Octahedrons with $\langle 100 \rangle$ Orientation

Au cuboctahedrons and Au octahedrons with $\langle 100 \rangle$ orientation were synthesized by using monolayer array of assembled truncated Au cubes as seeds (Figure 3-8). Because of the preferential $\langle 100 \rangle$ orientation of cubes within arrays, plasma treatment caused the exposure of one $\{100\}$ and four $\{111\}$ crystal facets on the top half of the seeds (Figure 3-8a). The subsequent Au deposition selectively on the exposed crystal facets led to the formation of truncated octahedrons. About three quarters of all the resulting truncated octahedrons exhibited $\langle 100 \rangle$ orientation in the arrays (Figure 3-8 c,d). The rest existed either in other orientation modes (i.e., 8.7 % in $\langle 110 \rangle$ orientation and 10.5 % in $\langle 111 \rangle$ orientation) or presented as defects originated from the irregular shape of seeds. The relatively low percentage of $\langle 110 \rangle$ and $\langle 111 \rangle$ orientation modes might be a result of non-closely packed seeds. The average space between NCs decreased from 26.5 ± 4.3 nm to 20.1 ± 7.6 nm after Au deposition when truncated cubes transformed into truncated octahedrons.

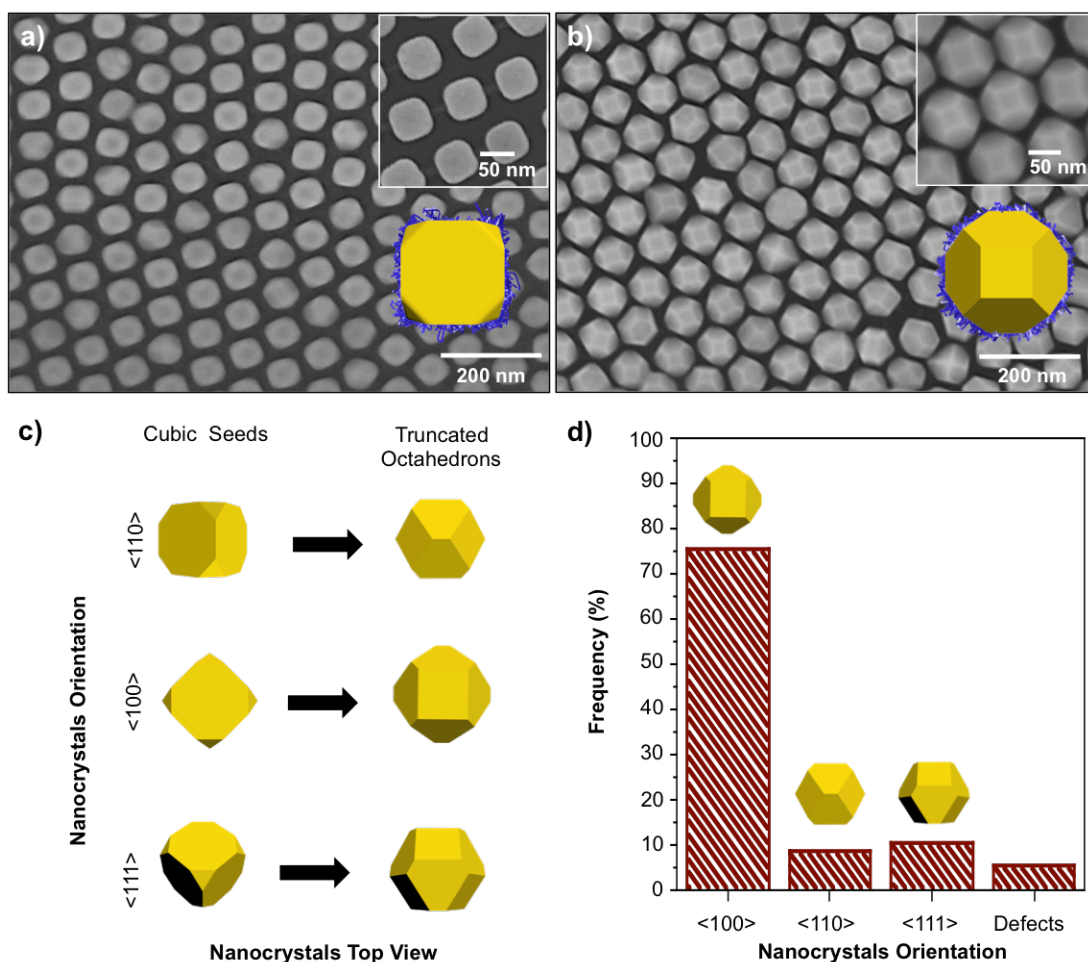


Figure 3-8. Top view SEM images of 2D array of (a) Au truncated cubic seeds with <100> orientation with respect to the substrate (before metal deposition) and (b) Au truncated octahedrons with <100> orientation (after metal deposition). c) 3D models illustrating the shape transformation of Au truncated cubic seeds with <110>, <100>, <111> orientation. d) Histogram analysis of the orientation of resulting Au truncated octahedrons within the 2D array.

The shape evolution of NCs was studied from cubic seeds to cuboctahedrons, truncated octahedrons and finally octahedrons, throughout the course of Au deposition (Figure 3-9). Au cuboctahedrons were obtained after incubating the seeds in the growth solution at 40 °C for 2 hours. At a 5-hour incubation time, the prolonged metal deposition produced truncated octahedrons. When the metal deposition occurred in growth solution with doubled concentration of gold precursor

at 60 °C for 10 hours, Au octahedrons were obtained. With the evolution of the NCs, the $\{100\}$ center crystal facet of cube seeds gradually decreased and eventually disappeared, while the four $\{111\}$ triangular crystal facets at the top corners elongated and merged at the time point when the $\{100\}$ crystal facet disappeared. With the transformation of NCs from cubes, to cuboctahedrons, and finally to octahedrons, the diagonal length of NCs increased from 71.5 ± 3.7 nm, to 77.8 ± 5.7 nm and eventually to 83.5 ± 5.0 nm (Appendix A.13).

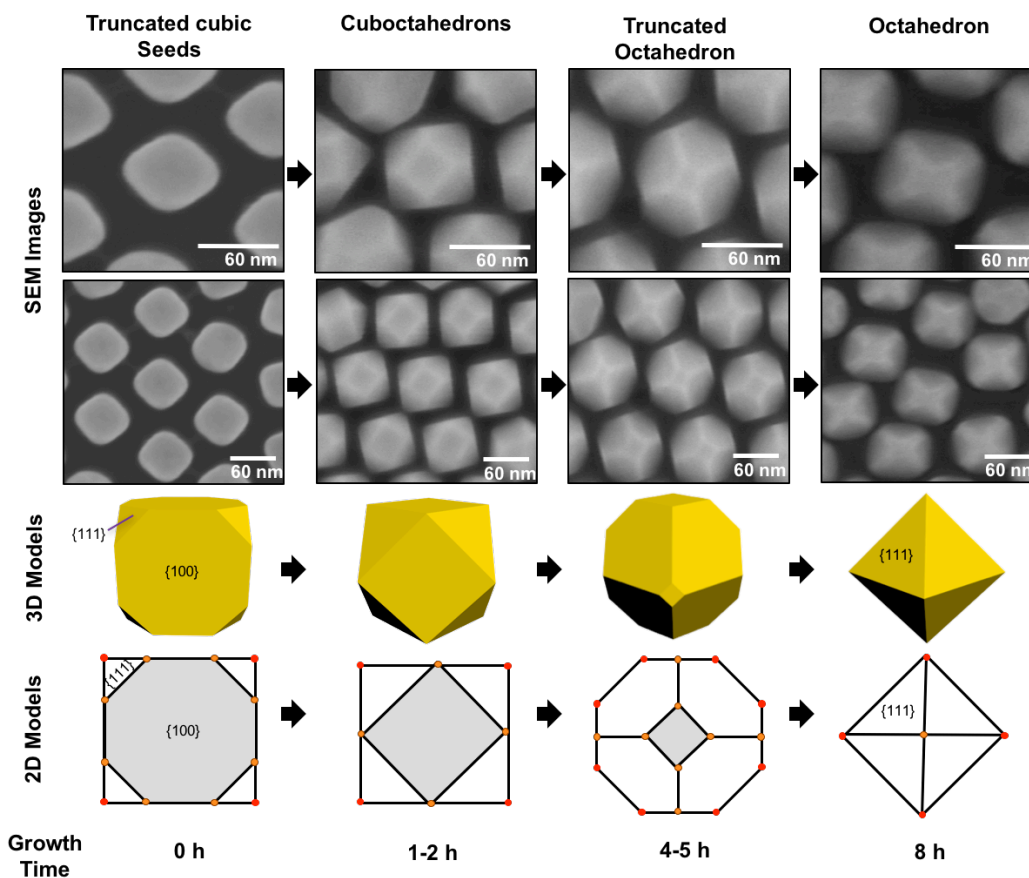


Figure 3-9. Top view SEM images, 3D, and 2D models illustrating the time-dependent shape evolution of Au truncated cubic seeds along the $\langle 100 \rangle$ orientation.

As a result of the different metal deposition rate on the top and bottom halves of the seed NPs, the final NCs were also asymmetric in shape with respect to their top and bottom halves (Figure 3-10). Such shape difference between the top and bottom

halves can be seen from the side view SEM images and 3D models of the asymmetric Au cuboctahedrons and octahedrons.

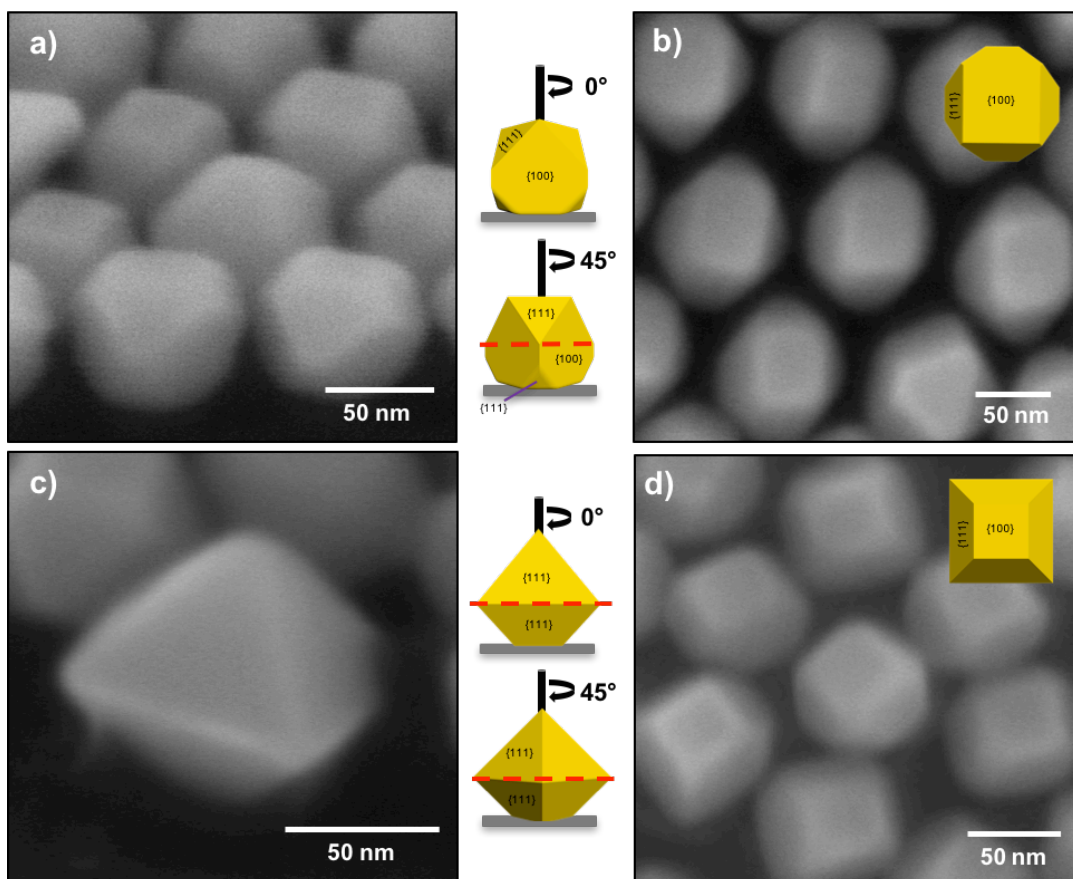


Figure 3-10. (a, c) Side view and (b, d) bottom view SEM images and 3D models of (a,b) asymmetric Au cuboctahedrons and (c,d) asymmetric Au octahedron obtained after the metal deposition on Au cubic seeds.

Furthermore, an examination of the bottom part of the Au cuboctahedrons and octahedrons indicates that the $\{100\}$ square facets located at the bottom of the Au still remained from the cubic seeds. Because of the presence of collapsed PS chains at the bottom surface of immobilized seeds, there was slower metal deposition rate on the bottom half of cubic seeds. The average diagonal lengths of the bottom $\{100\}$ crystal

facets of the Au cuboctahedrons and octahedrons were 59.8 ± 6.7 nm and 49.0 ± 4.7 nm, respectively (Figure 3-11)

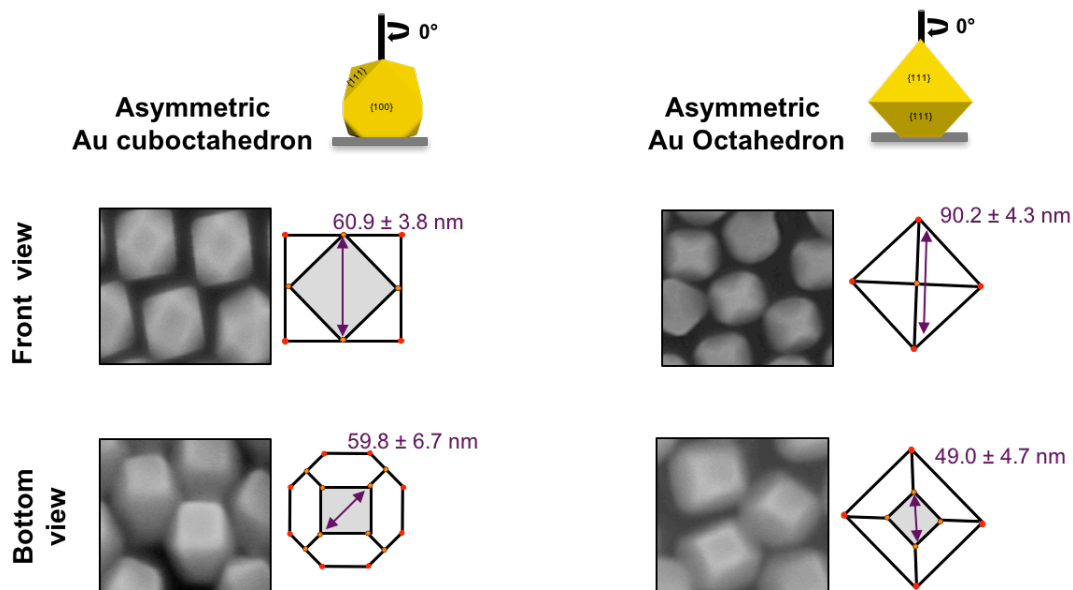


Figure 3-11. Front and bottom view SEM images and 2D projections of resulting asymmetric cuboctahedron and octahedrons showing the gradual decrease of diagonal length of the top and bottom $\{100\}$ crystal facet. The bottom $\{100\}$ crystal facet is preserved as the top $\{100\}$ facet vanishes.

3.3.5. Array of Au Octahedrons with $\langle 111 \rangle$ Orientation

Au octahedrons with $\langle 111 \rangle$ orientation were obtained using 2D arrays of Au octahedrons as seeds. When PS-tethered Au octahedrons assembled into 2D arrays, they acquired $\langle 111 \rangle$ orientation on the substrate (Figure 3-12a). With this orientation, the top view of seed NPs looks like that of Au triangles, as only one $\{111\}$ triangular crystal facet of the Au octahedral seeds can be observed in the SEM images. After treating the seed arrays with oxygen plasma and depositing Au at 40 °C for 5 hours, the top view triangular $\{111\}$ crystal facets were preserved and increased in size.

An analysis of crystal orientations shows that 80.9% of the NC exhibited triangle-like geometry due to the $\langle 111 \rangle$ orientation of seeds (Figure 3-12d & 3-13) Surface

growth defects such as merged particles or irregular shapes counted 17.3 %, while 1.9 % of the octahedrons adopted $\langle 110 \rangle$ orientation. There were no Au octahedrons with $\langle 100 \rangle$ orientation.

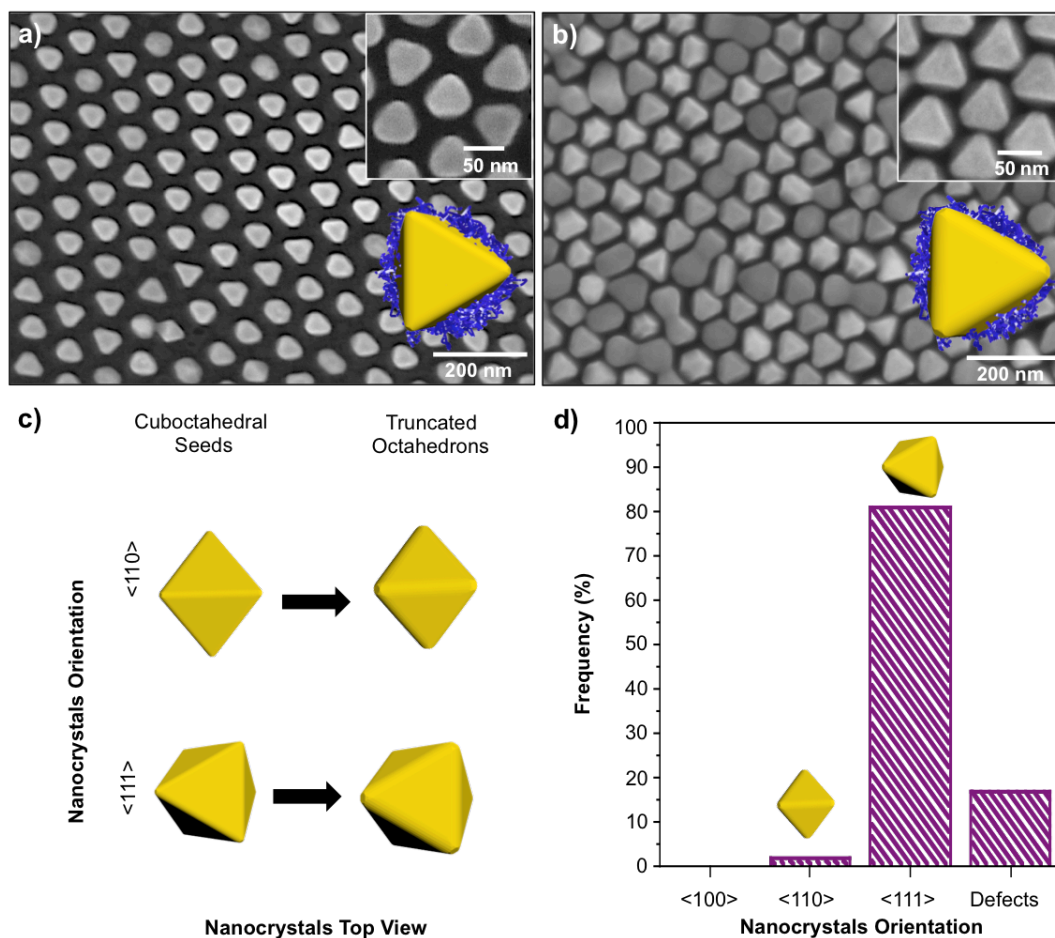


Figure 3-12. Top view SEM images of 2D array of (a) Au octahedron seeds (before Au deposition) and (b) Au truncated octahedrons (after Au deposition). c) 3D models showing the shape transformation of Au octahedral seeds with $\langle 110 \rangle$ and $\langle 111 \rangle$ orientation. d) Histogram analysis of the orientation of resulting Au truncated octahedrons within the 2D array.

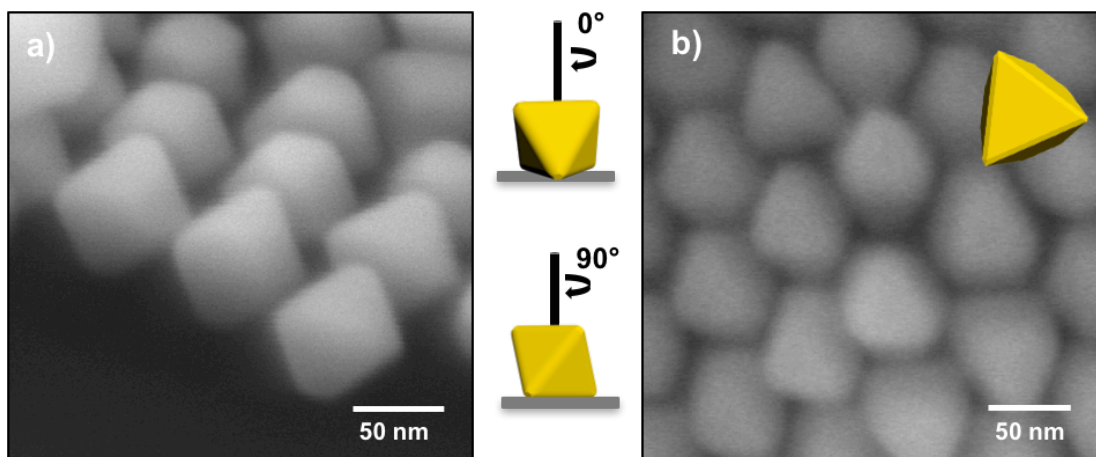


Figure 3-13. (a) Side view and (b) bottom view SEM images and corresponding 3D models of octahedrons with $\langle 111 \rangle$ orientation, after Au deposition.

Figure 3-14 illustrates the evolution of the top $\{111\}$ triangular crystal facet of the Au octahedrons. When the 2D array was incubated in the Au growth solution at 40 °C for 5 hours, the top crystal facet increased in size and became more truncated. By doubling the concentration of Au and incubating for 10 hours, the truncation decreased and the top $\{111\}$ crystal facet of the Au octahedrons increased in size. The length between one triangular vertex to the opposite side edge increased from 46.6 ± 4.9 nm to 58.8 ± 4.7 nm (see 2D models in Appendix A.14).

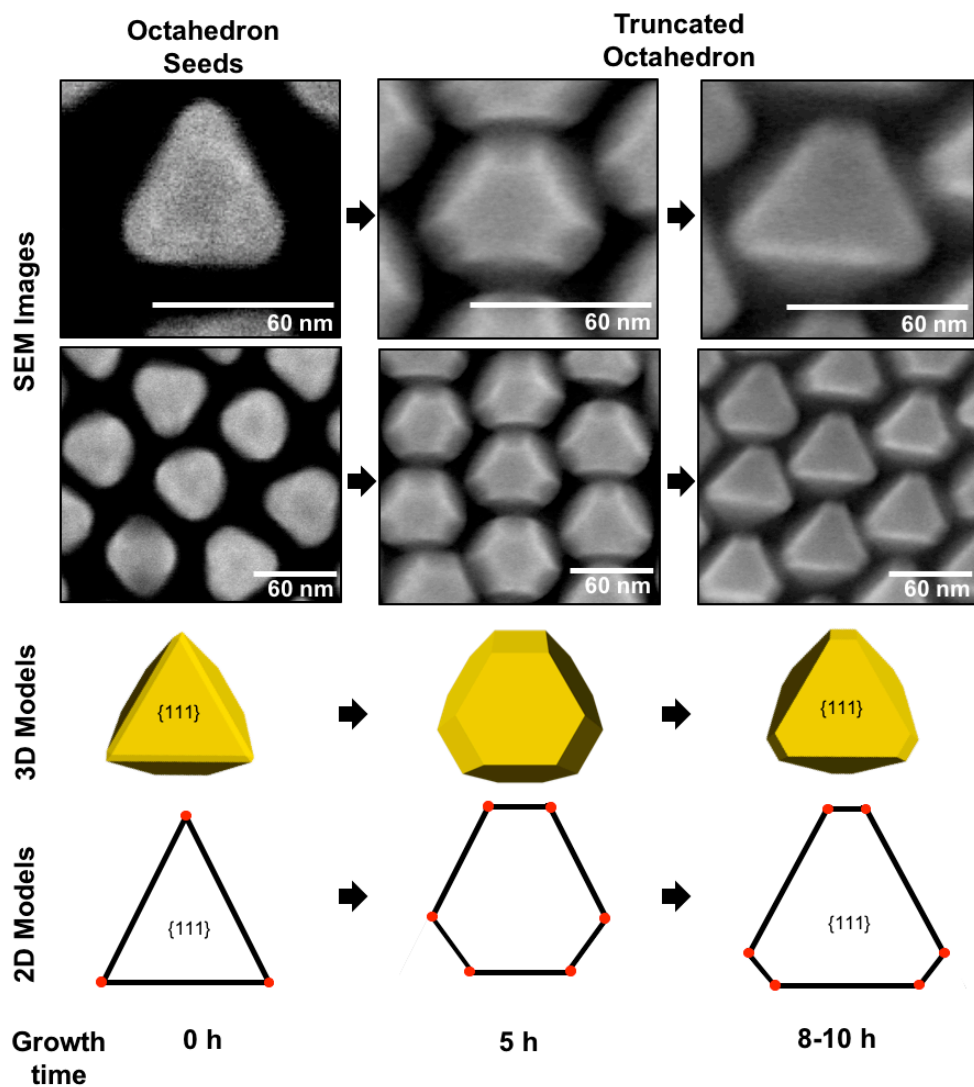


Figure 3-14 Top view SEM images, 3D, and 2D models illustrating the time-dependent shape evolution of Au octahedral seeds along the $\langle 111 \rangle$ orientation.

3.4. Conclusion

In summary, I developed an immobilized seed-mediated growth method for the fabrication of 2D arrays of asymmetric Au NCs with defined shapes and specific orientations on substrates. This method relies on the selective position of a second metal on the exposed surface of seed NPs immobilized on substrates. Au seeds with cuboctahedral, cubic, and octahedral shapes transformed into Au truncated

octahedrons preferentially oriented in the $\langle 110 \rangle$, $\langle 100 \rangle$ and $\langle 111 \rangle$ mode, respectively. The locally collapsed polymer at the bottom surface of the seeds fix the seed arrays on the substrate, and simultaneously confine the metal deposition on the top crystal facets of the seeds to produce asymmetric polyhedral NCs, which distinguishes this method from existing methodologies for the fabrication of shaped NPs arrays. Furthermore, this method provides a simple technique to acquire arrays of polyhedral NCs with specific orientation by selecting shaped seeds with predominant orientation. This synthetic method allows for easy monitoring the growth kinetics of NP arrays. The $\{111\}$ facets increased in size while the $\{100\}$ crystal facets decreased. With the prolongation of growth time, $\{111\}$ crystal facet dominated the top surface of the NCs and $\{100\}$ crystal facets disappeared. We expect that the library of substrate-supported NP arrays will find a broad range of applications in sensing, catalysis, optical and electronic devices.

Chapter 4: Growth of Two-dimensional Array of Au@Pd Asymmetrical Polyhedrons with Defined Orientations

Ideas do not always come in flash but by
diligent trial-and-error experiments
that take time and thought.”

Dr. Charles K. Kao
Nobel Prize in Physics
2009

4.1. Introduction

NCs composed of two metals provide a pathway to control their optical, electronic and catalytic properties¹⁵³⁻¹⁵⁴. These properties enables the broad applications of bimetallic NCs in photocatalysis, and sensing⁵⁰. Bimetallic NCs like core-shell exhibit optical properties that cannot be found in single component NCs¹⁵⁵, as a result of the synergetic effect between different components⁵⁰. Among other bimetallic NCs Au@Pd NCs are particularly attractive, because Au can serve as plasmonic antennae to enhance the electromagnetic field while Pd can serve as a good sensor through its high refractive index sensitivity. For instance, Au@Pd core-shell NCs have been demonstrated for fabricating sensitive and low-cost hydrogen gas sensors^{50, 156}. Pd has the capability to absorb hydrogen gas reversibly to form palladium hydride (PdH), while Au NCs have LSPR in the visible range. Additionally, the properties of bimetallic NCs can be adjusted by tuning the shape and spatial distribution of two constituent components. For instance, by adjusting the

Pd shell thickness of Au@Pd NCs, the LSPR band can be readily tuned in visible and near infrared region.¹⁵⁷

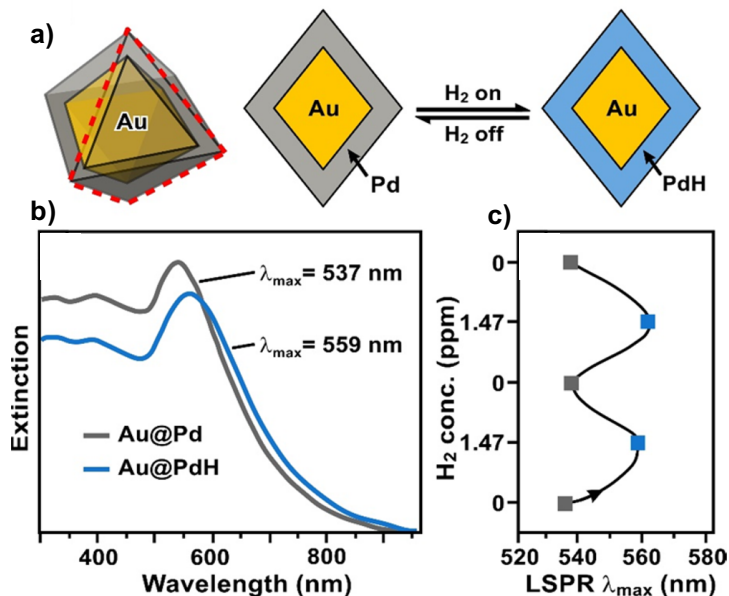


Figure 4-1. (a) Schematic showing Au@Pd core-shell NCs capability to detect H₂ and transform to Au@PdH. (b) Extinction spectra of Au@Pd octahedrons before and after exposure of H₂. (c) Plot showing that Au@Pd system to detect H₂ is reversible. Figures adapted with permission from American Chemical Society [REF 50], Copyright 2016.

To incorporate Au@Pd NCs in functional devices, the organization of Au@Pd NCs into 2D array is crucial for plasmonic sensing device. Lithography method (e.g., laser interference lithography¹⁵⁸) has been used to fabricate bimetallic arrays. Though this method can produce large array areas, approximately $5 \times 5 \text{ mm}^2$, this method is limited to spherical shapes and large distance between particles, $\sim 700 \text{ nm}$ apart from each other. Moreover, it requires high technology instrumentation such as electron beam evaporator to deposit the metal films, which makes the fabrication costly. In contrast, self-assembly method offers a simple and cost-effective method to fabricate bimetallic arrays with different shapes, specific orientation and narrow distance

between NCs.

As described in the last Chapter, an immobilized seed-mediated growth method to fabricate 2D array of polyhedral NCs was successfully developed. In this Chapter, the concept is extended by fabricating 2D arrays of bimetallic NCs. Using the method of immobilization of shaped seeds (Chapter 3), I fabricated 2D arrays of Au core Pd cubic shell (Au@Pd) polyhedral NCs with defined shapes, controlled spacing, and specific orientation. 2D arrays of Au@Pd cubic shell were created by local deposition of Pd on 2D arrays of Au cuboctahedral and cubic seeds. Remarkably, the individual bimetallic polyhedral NCs within the arrays have asymmetric geometry, that is, the top half part of the NCs were different in shape from their bottom half part. Additionally, the particle distance of the resulting array can be modulated by tuning the deposition time of the second metal precursor or by controlling the length of polymer tethers on Au seeds. The individual polyhedral NCs within the 2D arrays can be released from the substrate by adding water and carefully scraping the substrate.

4.2. Experimental Methods

4.2.1. Materials

Palladium(II) chloride (PdCl_2 , 99%+), Gold (III) chloride trihydrate ($\text{HAuCl}_4 \cdot 3\text{H}_2\text{O}$, 99.99%+), Hexadecyltrimethylammonium bromide (CTAB, 99%+), L-ascorbic acid (AA, 99%+), tetrahydrofuran (THF) were purchased from Sigma-Aldrich. Thiol-terminated polystyrene (PS-SH, $M_n = 50,000$, PDI=1.09) was purchased from Polymer Source Inc. All the chemicals listed above were used as

received without further processing. Deionized water (Millipore Milli-Q grade) with resistivity of 18.0 M Ω was used in all the experiments.

4.2.2. Pd Deposition on Exposed Surface of Au Nanocrystal Arrays

Assembly of shaped seed arrays are the same as described in Chapter 3, Section 3.2.2 - 3.2.4. The array of Au seed were placed in the Pd growth solution. The Pd growth solutions were prepared in 20 mL vials containing 19 ml of 10 mM CTAB solution. The CTAB solution was placed in a water bath at 30 °C. After the temperature was stabilized, specific quantities of 10 mM H₂PdCl₄ (H₂PdCl₄ was prepared in the lab using PdCl₂ and HCl) and 100 mM AA were added to the CTAB solution. Subsequently, the plasma-treated seed arrays on Si wafers were immersed into the Pd growth and incubated for 8-12 hours. After the completion of metal deposition, the samples were removed from the growth solution and rinsed with deionized water. The detailed reaction conditions are given in Appendix A.15. Similarly, Au cubic core @ Pd cubic shell were synthesized by incubating the substrates of Au cubic arrays in Pd growth solution in a water bath at 30 °C for 12 h. The Pd growth solution contained 19 ml of 10 mM CTAB solution 500 μ L of 10mM H₂PdCl₄ and 250 μ L of 100mM AA.

4.2.3. Characterization and Sample Preparation

Pd deposition on Au shaped NCs arrays were analyzed by elemental analysis using JEM 2100 FEG Transmission Electron Microscope (FEG-TEM) Samples for elemental analysis were prepared on 300 mesh carbon-coated copper grid. A 5-10 μ L of water was dropped on the array of Au@Pd NCs. A toothpick was then used to

gently scratch the sample off the Si wafer. A Cu grid was placed on top of the water droplet on the Si wafer and let dry. Additionally, the morphologies of polyhedral NCs were imaged using a Hitachi SU-70 Schottky Field Emission Gun Scanning Electron Microscope (FEG-SEM) and JEOL JEM 2100 Field-Emission Gun Transmission Electron Microscope (JEM 2100 FEG).

4.3. Results and Discussion

Using the immobilized seed-mediated growth strategy described in Chapter 3, it was possible to tune the growth condition to fabricate 2D arrays composed of Au@Pd asymmetric NCs with controlled size, shape, and orientation. This method relies on the controlled solution-phase deposition of Pd ions on selectively exposed surface of self-assembled Au seed NPs that are immobilized on a substrate through collapsed polymer brushes (Figure 4-2).

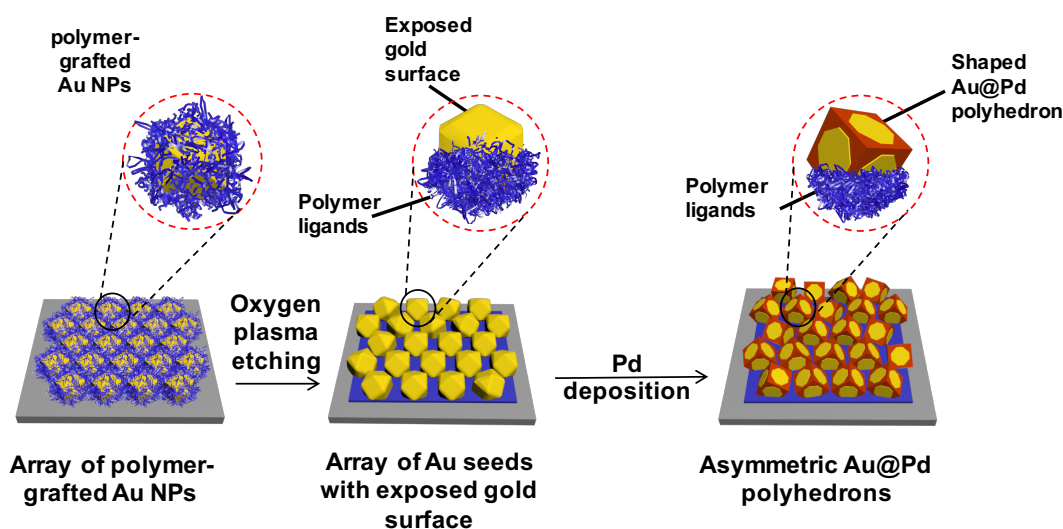


Figure 4-2. Schematic illustration of immobilized seed-mediated growth of 2D array of asymmetric Au@Pd polyhedral NCs. The process involves the self-assembly of polymer-grafted Au NPs into 2D arrays on the substrate, selective removal of polymer ligands from the top surface of NPs by oxygen plasma treatment, and deposition of a Pd metal selectively on the exposed surface of Au seed NP arrays.

4.3.1. Array of Asymmetric Nanocrystals with Au Cuboctahedral Core and Pd Cubic Shell Nanocrystals

Well-controlled Pd reduction and deposition on the Au cuboctahedral seed array led to the formation of asymmetric polyhedral NCs with Au core and Pd cubic shell (Figure 4-3 a-d). Similar to the surface-growth case of Au truncated octahedron, the presence of the polystyrene in the half-bottom part of the seeds anchor them to the substrate, and hindered or limited the Pd deposition. The asymmetric geometry of these NCs was confirmed by elemental analysis of NCs released from the substrate-supported arrays. The elemental line scan shows that the concentration of Pd was higher at the edges than at the middle of the NCs. This is also the case for almost all the core-shell type NPs, because of the edge effect. The elemental line scan of Au cuboctahedron core @ Pd cubic shell suggests that the deposition of Pd occurred largely at the top half, while Pd is deprived at the bottom half of the Au core @ Pd NCs (Figure 4-3e).

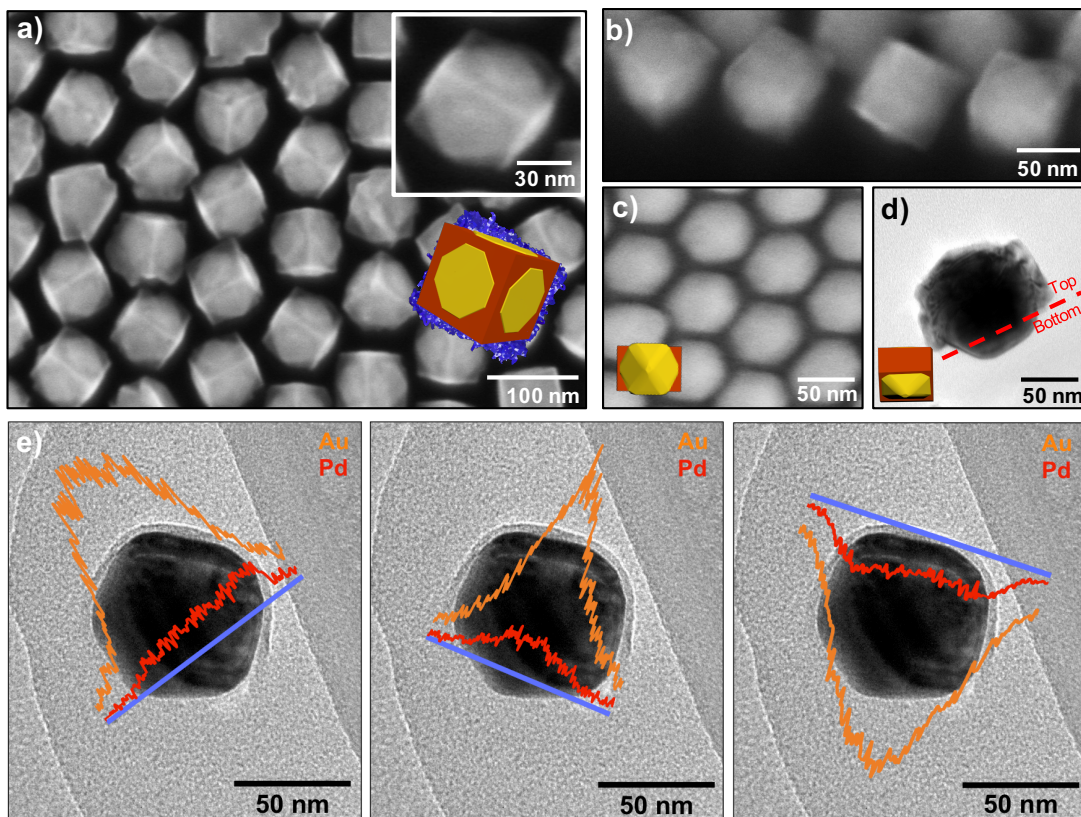


Figure 4-3. (a-c) Top view (a), side view (b) and bottom view (c) SEM images of 2D array of asymmetrical Au cuboctahedral core@Pd cubic shell NCs. d) Side view TEM image of a single NC released from the substrate. The red dashed line indicates the boundary between the top and bottom half of the resulting NCs. (e) TEM images and energy-dispersive X-ray spectrometer line scans of a single Au cuboctahedral core @ Pd cubic shell NC showing the formation of asymmetric NCs (i.e., the top and bottom of the NC has different content of Pd deposition).

This method produced arrays of 82.8 % Au cuboctahedral core with Pd cubic shell. Figure 4-4 shows that ~64.0% of the Au@Pd NCs showed a $\langle 110 \rangle$ orientation in the array, while the population of $\langle 100 \rangle$ and $\langle 111 \rangle$ orientation were 7.3% and 11.5%, respectively. Defects in the surface growth or seeds counted for another 17.2%. The Au@Pd NCs had $\langle 110 \rangle$, $\langle 100 \rangle$, $\langle 111 \rangle$ orientations because the seeds acquired that orientation when assembled into 2D array and the Pd deposition occurred on the seed top crystal facets.

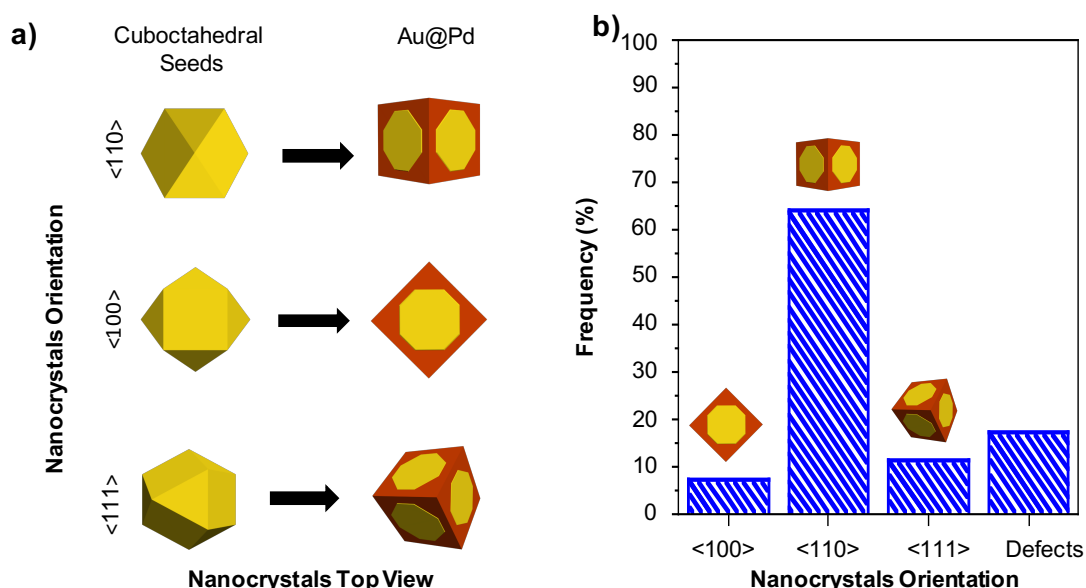


Figure 4-4. (a) 3D models showing the shape transformation of Au cuboctahedral seeds with <110> <100> <111> orientation with the deposition of Pd. b) Histogram analysis of the orientation of resulting Au cuboctahedral core@Pd cubic shell in the 2D array.

The evolution of the Au@Pd NCs was studied by adjusting the incubation time and concentration of Pd and AA. At a relatively low concentration of Pd precursor and 5h incubation, Pd deposition occurred only on the {111} crystal facet of the Au cuboctahedrons (Figure 4-5). When more Pd was deposited on the {111} crystal facets, Pd surrounded the Au cuboctahedron {100} crystal facets producing Au@Pd cubic frames (i.e Au cuboctahedron enclosed within cubic frame of Pd). This occurred when the array of Au cuboctahedral seeds were incubated for 12 hours in a Pd growth solution. The formation of Pd shell led to an increase in the diagonal length of NCs from 73.8 ± 3.9 nm to 82.0 ± 3.0 nm. The complete engulf of Au seeds in Pd cubic shell was achieved with the further increase in the concentration of Pd and the diagonal length of NC increased to 95.3 ± 6.3 nm (Appendix A.16.).

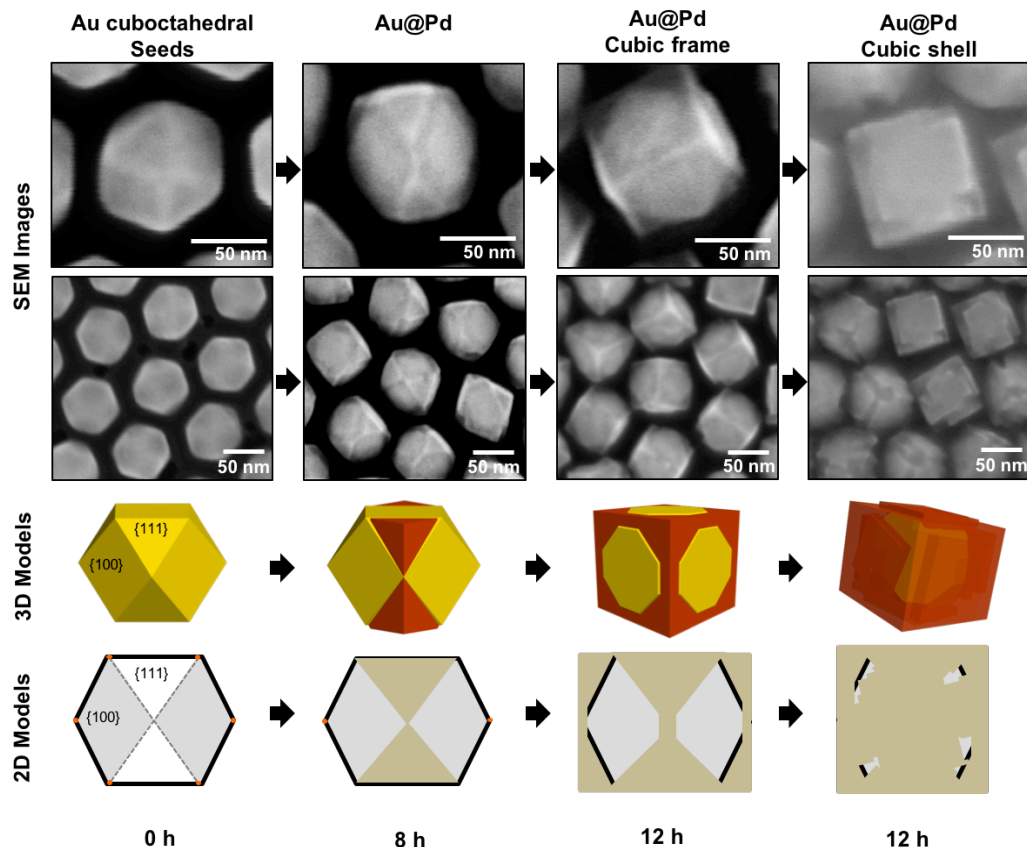


Figure 4-5. Top view SEM images, 3D, and 2D models illustrating the shape transformation of Au cuboctahedral seeds into Au@Pd core-cubic shell with $\langle 110 \rangle$ orientation.

4.3.2. Array of Asymmetric Au Cubic Core and Pd Cubic Shell Nanocrystals

Au cubic shapes were preserved after deposition of Pd resulting in the formation of Au cubic core with Pd cubic shell (Figure 4-6). Au cube seeds lost their truncation feature after Pd deposition. The vertices of the Au cubic seeds became sharper. This is consistent with previous reports where it has been indicated that Pd atoms deposit on the edges of the Au cores areas of higher energy¹⁵⁹.

The elemental line scan in Figure 4-7 shows that Pd cover the surface of the core, with a slightly higher Pd deposition at the edges than at the middle of the NCs. We believe, that Pd is deposited first at the edges and corners; then as the

concentration of Pd is increased, Pd atoms diffuse to the center of the Au seeds. Pd cubic shell are presumed to be form because CTAB served as a capping agent for the Pd {100} surface promoting the formation of Pd NCs enclosed by {100} facets¹⁶⁰.

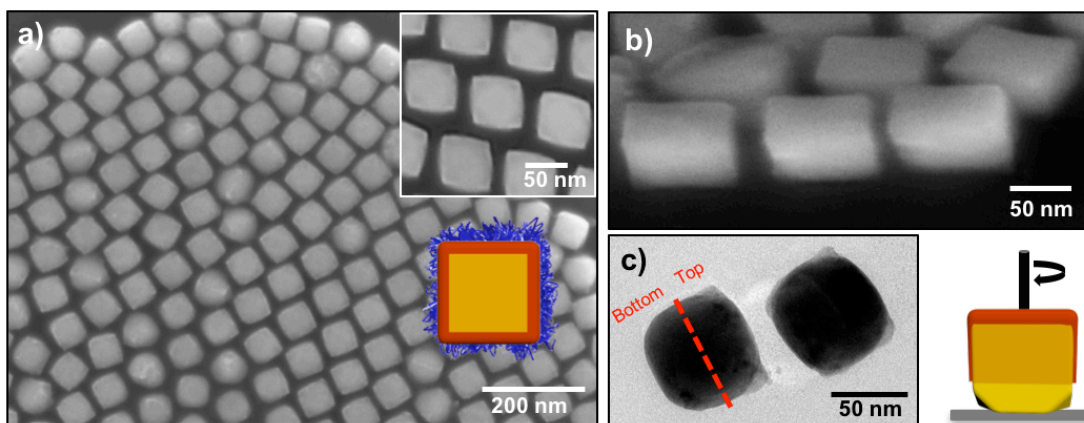


Figure 4-6. (a) Top view and (b) side view SEM images of 2D array Au cubic core cube@Pd cubic shell NCs. Inset in (a) is the high magnification SEM image of the NC array. c) TEM image and 3D NC model of these NC released from the substrate.

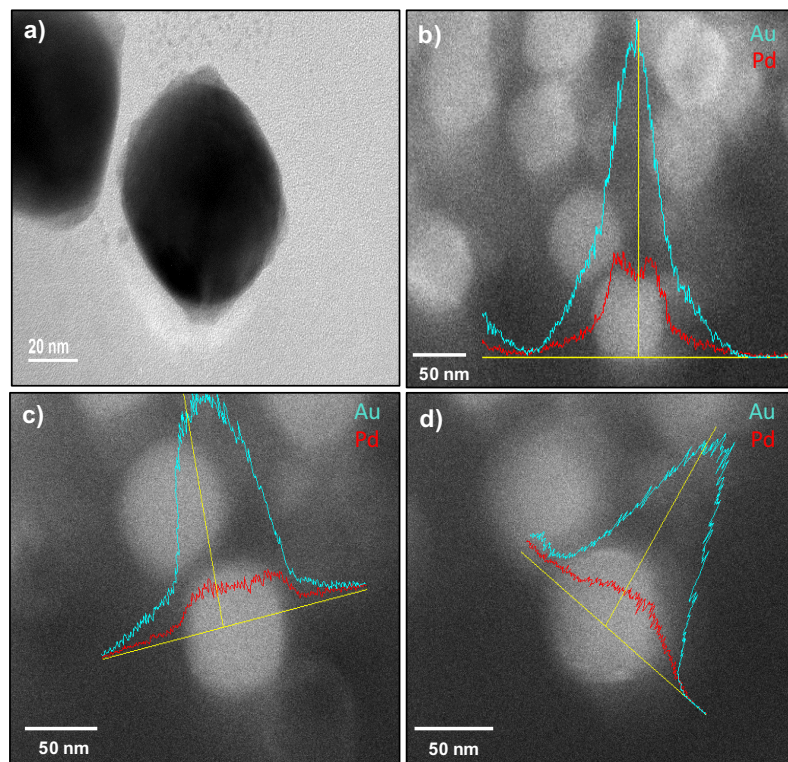


Figure 4-7 (a) TEM images and (b-d) energy-dispersive X-ray spectrometer line

scans of a single Au cubic core @ Pd cubic shell NC showing the composition of asymmetric NCs.

4.4. Conclusion

Substrate-based growth method shows to be a practical technique to fabricate bimetallic NCs. The preferential orientation of the Au seeds and the well control of the reduction of Pd precursor enable the enable the production of high quality of Au@Pd NCs. This method can be potentially extended to the synthesis of NPs with other compositions such as metal oxides. It opens up a new venue for fabricating functional plasmonic NCs directly on a substrate, with potential applications in technologies such as photovoltaic devices, biological and chemical sensors. Additionally, this substrate-based NC growth method shows the following features over existing approaches: i) it is cost efficient, as it does not require any lithography ; iii) it can potentially be adapted to fabricate, directly on a substrate, functional NCs with potential applications in such as photovoltaic devices, biological and chemical sensors.

Chapter 5: Conclusion and Future Work

“ Be the change that you wish
to see in the world.”

Mahatma Gandhi

For the last decade, researchers in the field of plasmonic nanomaterials have extensively used plasmonic nanospheres as primary building blocks to design materials with applications in such as photovoltaic devices⁷⁻⁸, catalysis,⁹⁻¹⁰ sensors¹¹⁻¹², and imaging contrasting agents for medical diagnosis⁶⁹.

To facilitate the application of shaped NCs in different fields, it is essential to improve our existing understanding on solution-based synthesis of polyhedral NCs and develop techniques to assemble shaped NCs in a better controlled manner.

With the vision of reducing chemical waste accumulation from failed attempts to obtain high-quality polyhedral NCs, we investigated the reaction mechanism that underlines the growth Au polyhedral NCs in solution prior nucleation. We also developed a methodology to fabricate 2D arrays of mono- and bi- metallic NC directly on a substrate without using complex and expensive instrumentation such as lithography.

In chapter 2 we presented the results of a comprehensive study for the three phases involved in a one-pot nanocrystal synthetic method. We propose that during the reduction of $[\text{AuBr}_4]^-$ with AA, a possible complex is formed between Au and AA. During the nucleation, NaOH as strong base possibly deprotonates the Au-AA complex and induces a complete transfer of electron from AA to Au, resulting in the

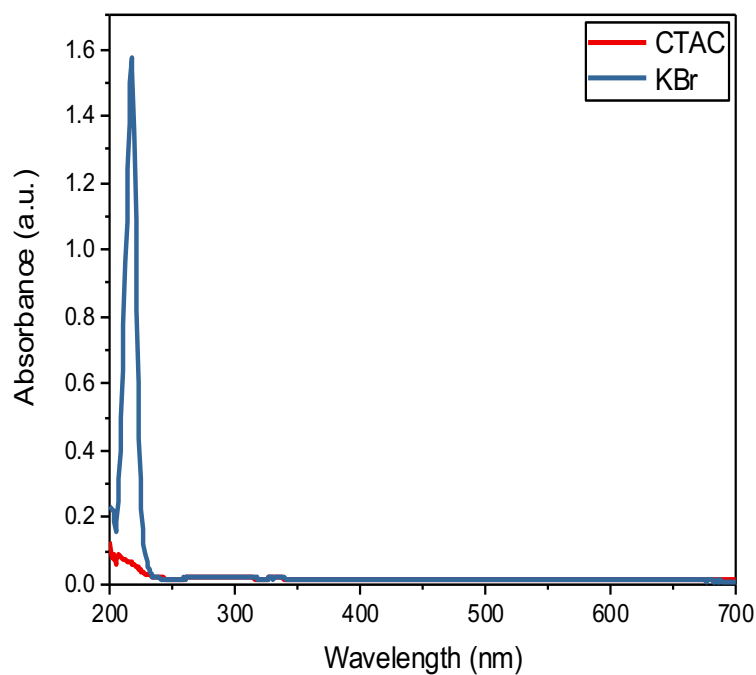
formation of Au(0) nuclei. Based on the proposed Au-AA complex structure, it is expected that Au has an oxidation state of Au(I). The intrinsic characteristic of Au(I) to disproportionate makes the Au-AA susceptible to degenerate over time. As Au-AA complex degenerates, the concentration of A(I) decreases altering the critical concentration of Au(I) needed for nucleation. This was the case of the Au cubes and Au cuboctahedron synthesis. Both NCs were obtained at 42 °C under different (Au-CTAB)-AA incubation time. This is a possible factor that can negatively impact the reproducibility of Au cube synthesis. Additionally, despite that 1:1 mole ratio Au and AA leads to complete reduction of Au, we found that excess of AA was necessary for the production Au cubes with monodisperse size and shape. We believe that the excess of AA is necessary to prevent Br⁻ ions binding to Au, as CTAB is present in excess and carries out the Br⁻ ions. For future work, we suggest elucidating the effect of Br⁻ ions during the reduction of Au ions with AA. To start, it is important to find out if the excess of Br⁻ ions are reacting with AA and through what mechanism it does. The answer to this question could result in a holistic understanding of the reaction mechanism that lead to nucleation. The modification and improvement in the traditional nanocrystal synthetic method could help to minimize the usage of CTAB surfactant, a toxic chemical for marine environment, and also reduce the accumulation of chemical waste that arise from polydispersity Au NCs that have to be discarded since they cannot be used for assembly due to their bad quality.

In chapter 3 and 4, we described techniques to develop a 2D array of seeds that enable the fabrication of mono- and bi- metallic polyhedral NCs directly on a substrate with controlled orientation, shape, and particle distance. This method relies

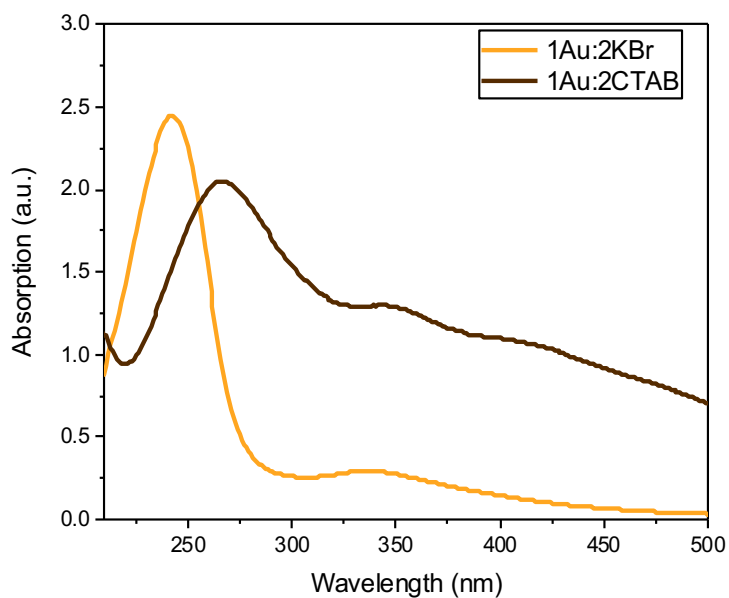
on the controlled solution-phase deposition of metals (e.g., Au and Pd) on selectively exposed surface of self-assembled seed nanoparticles that are immobilized on a substrate through collapsed polymer brushes. Specifically, in chapter 3 we demonstrated that 2D array of Au truncated octahedrons with $\langle 110 \rangle$, $\langle 100 \rangle$, and $\langle 111 \rangle$ orientation along the substrate, resulted from using Au seeds with cuboctahedral, cubic, and octahedral shapes respectively. In chapter 4, we demonstrated that our substrate-based method could be used to fabricate Au@Pd NCs with Au cuboctahedral or cubic core and Pd cubic shell. Our method presents the potential to be adapted to fabricate photovoltaic devices, biological and chemical sensors. For future work, we propose to work on the scalability of the method to produce 2D array areas of tens of cm^2 . Beyond application purposes, our substrate-based growth method serves as a tool to investigate NCs shape evolution of different compositions. For future work, we suggest using the 2D array of seeds to investigate the shape evolution of NCs through metal deposition without CTAB, or any surfactant. The role of CTAB is to disperse the NCs in solution phase to avoid their aggregation and modulate the shape of NCs. Since the NCs are attached to the substrate, solution dispersion is not necessary. In a proof of concept, Au octahedron NCs were obtained without CTAB, which is consistent with the Wulff construction Theory. In absence of CTAB, octahedrons are obtained because they are thermodynamically stable structures. Though the quality of octahedrons were not good. We believe that with an adjustment of reaction temperature it might be possible to improve the quality of Au octahedrons without CTAB. Our substrate-based growth

method could serve as a platform to try different growth conditions to design techniques that eliminate the usage of CTAB.

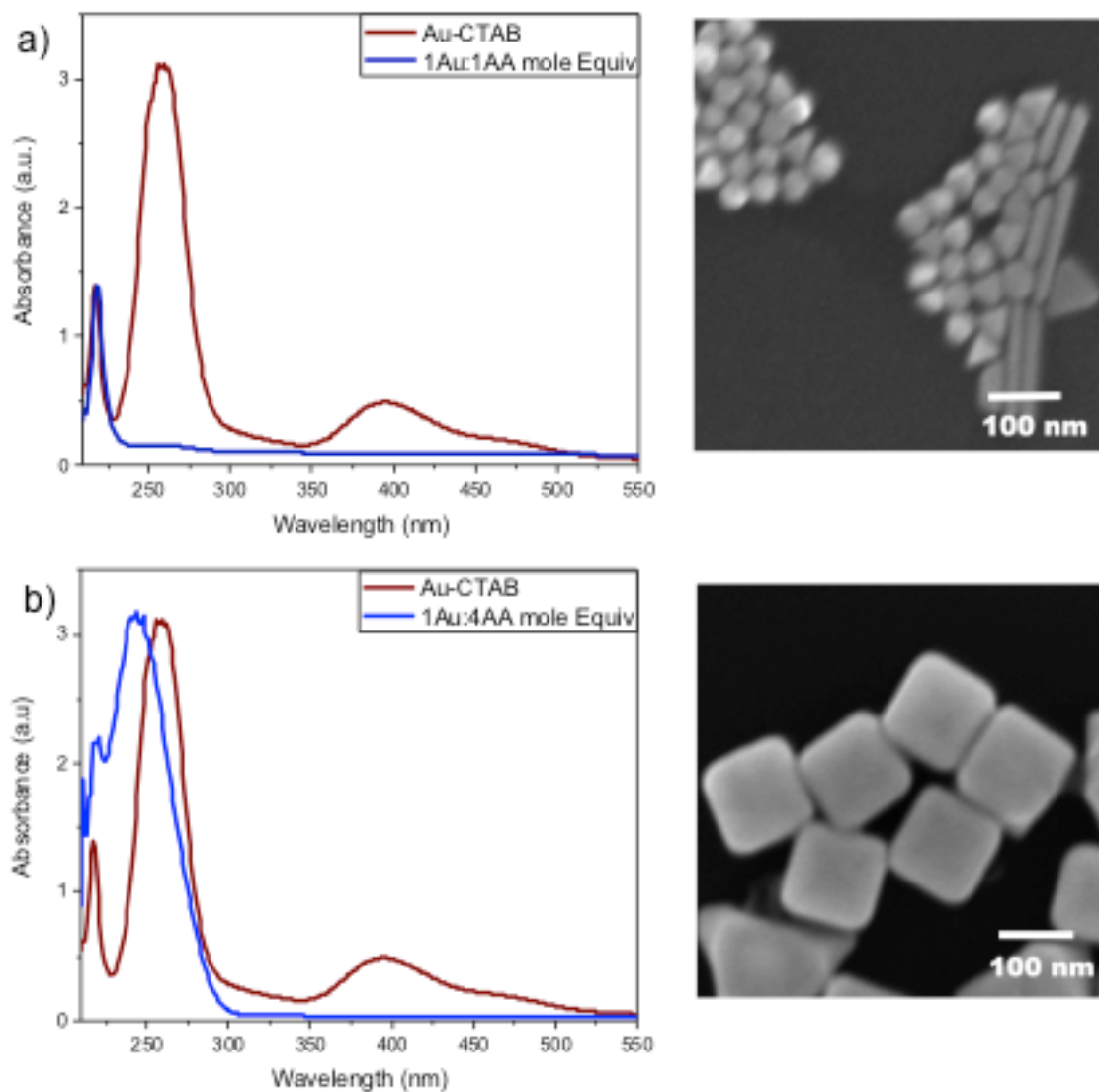
Appendix



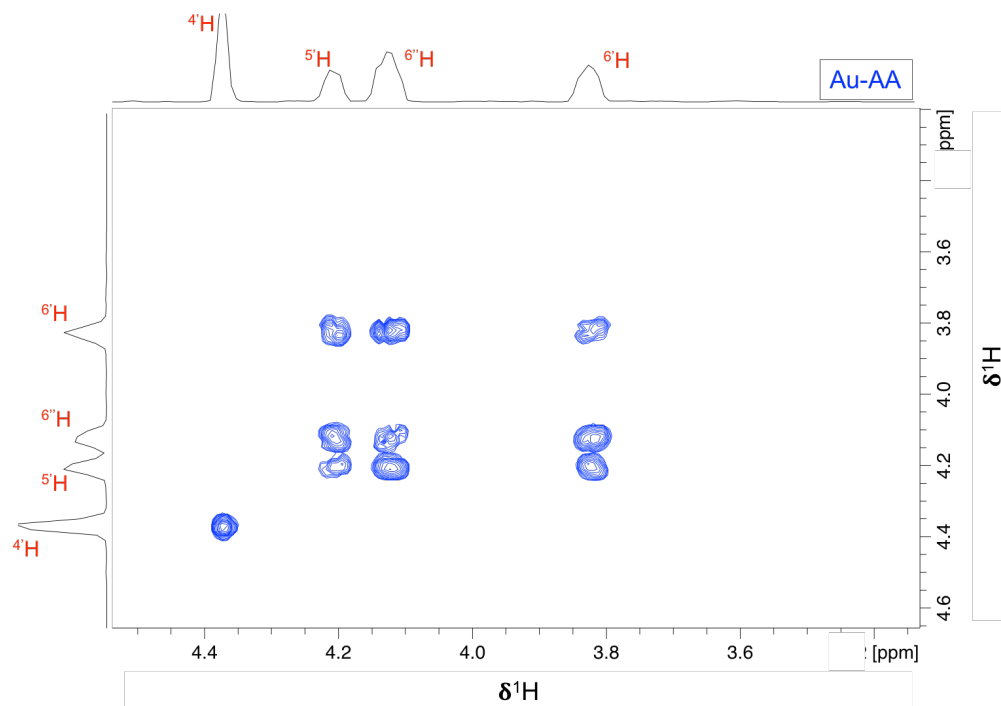
A.1. UV-VIS spectrum of CTAC surfactant and KBr showing that Br is not present in CTAC surfactant.



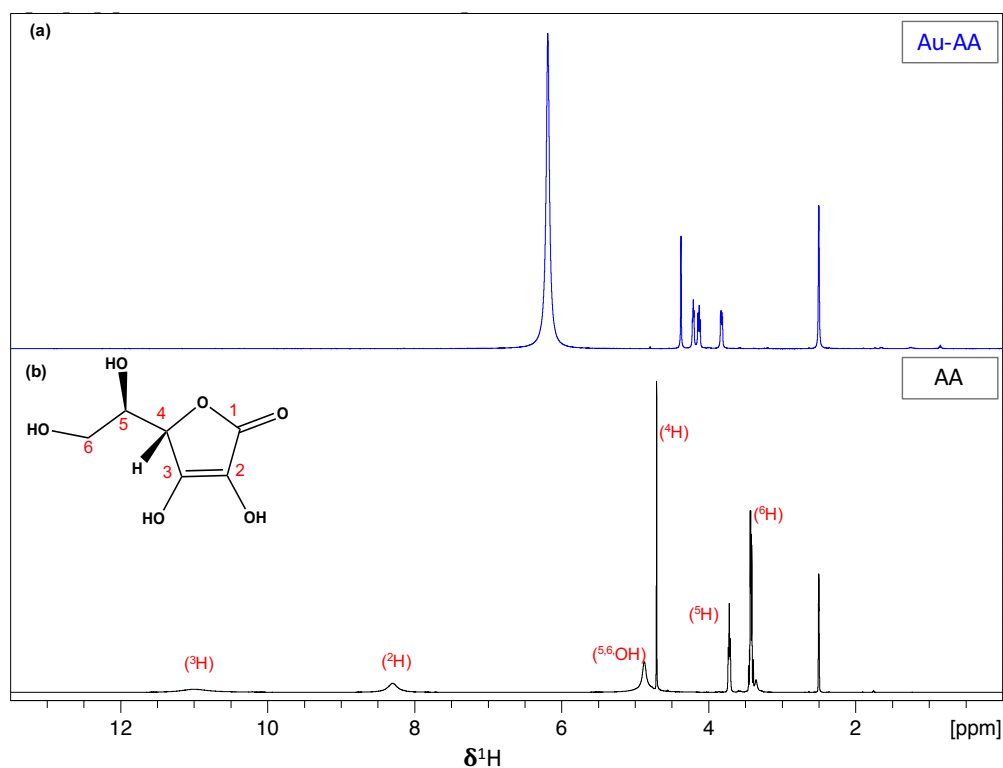
A.2. UV-VIS absorption of 1:2 mole equivalent of Au and Br- sources (i.e. CTAB and KBr) showing a high energy band at 260 nm expected from low oxidation state, Au(I).



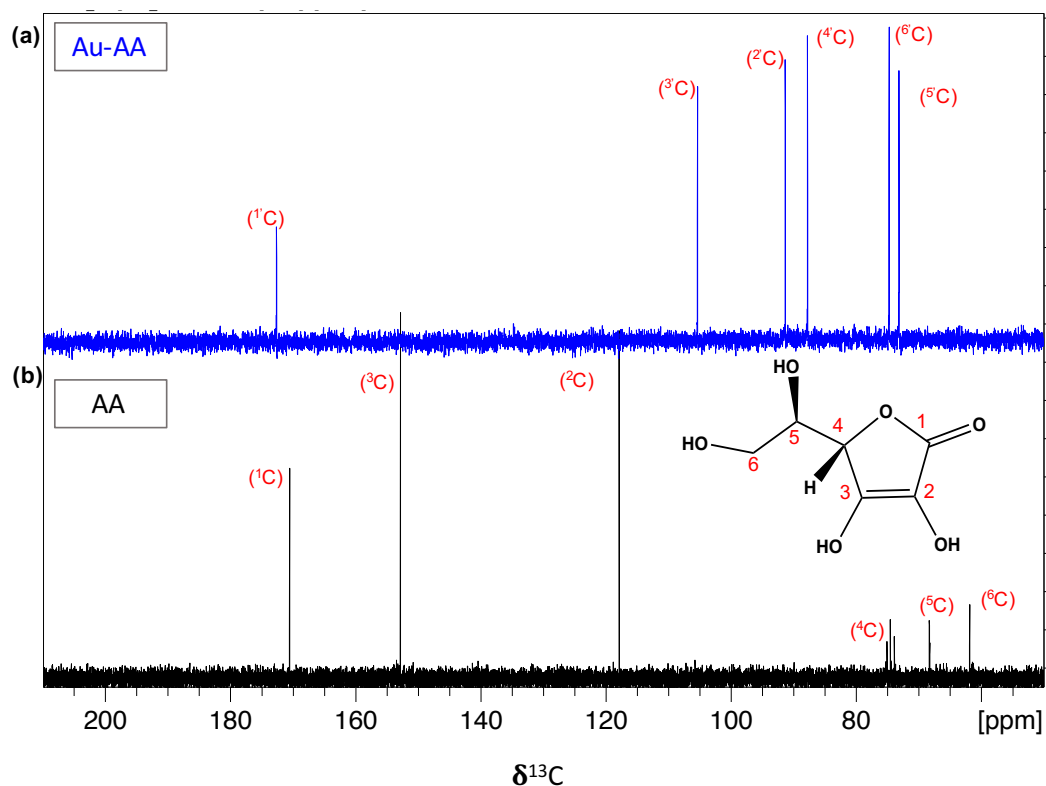
A.3. NCs with significantly improved quality were obtained at 1Au:4AA mole equivalent. UV-Vis spectra showing the [AuBr₄]⁻ complex reduction with a) 1Au:1 AA mole equivalent and b) 1Au:4 AA mole equivalent and their corresponding SEM images of synthesized NCs under both conditions.



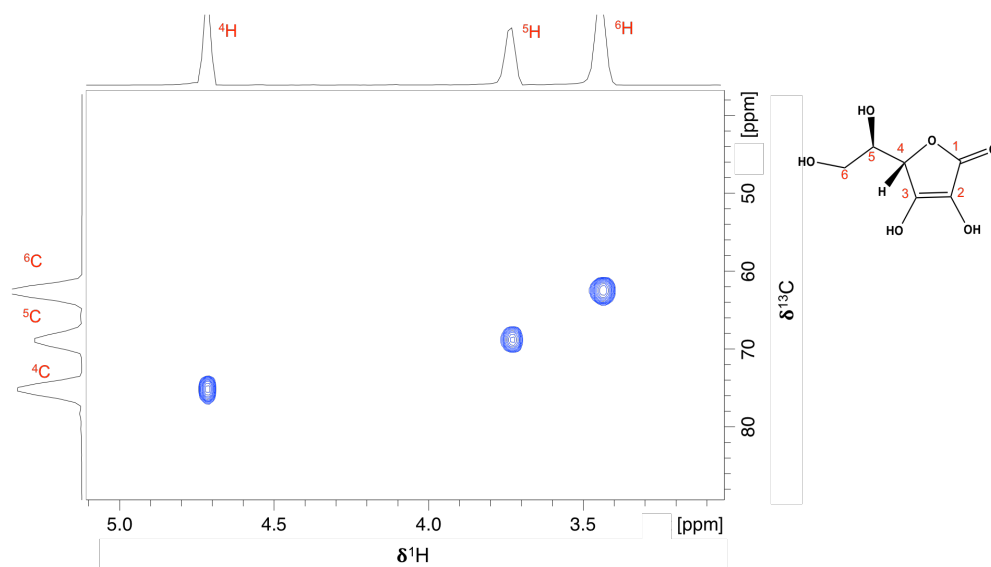
A.4 ^1H - ^1H COSY of Au-AA complex showing proton coupling. ^6H and ^5H couple with each other, while ^4H does not couple with any proton.



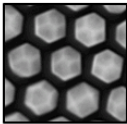
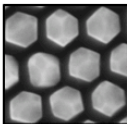
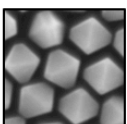
A.5. ^1H NMR full spectrum of a) gold and ascorbic acid 1:1 mole equivalent and b) pristine L-ascorbic acid (AA) showing the difference in chemical shifts.



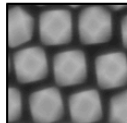
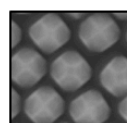
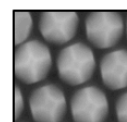
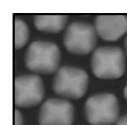
A.6. ^{13}C NMR of (a) Au-AA complex and (b) AA showing the difference in carbon chemical shift in presence of Au. The ^{13}C NMR spectrum of that Au-AA shows that there is only one carbonyl group confirming that dehydroascorbic acid is not present.



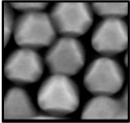
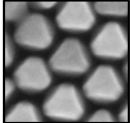
A.7. HSQC of AA showing that carbon 4,5,6 correlate with only one ^1H signal.

Polyhedral Nanocrystal	10 mM H _{AuCl} ₄	100 mM AA	Temperature	Incubation time
	100 μ L	12.5 μ L	40 $^{\circ}$ C	1-2 h
	100 μ L	12.5 μ L	40 $^{\circ}$ C	3-4 h
	200 μ L	25 μ L	40 $^{\circ}$ C	8 h

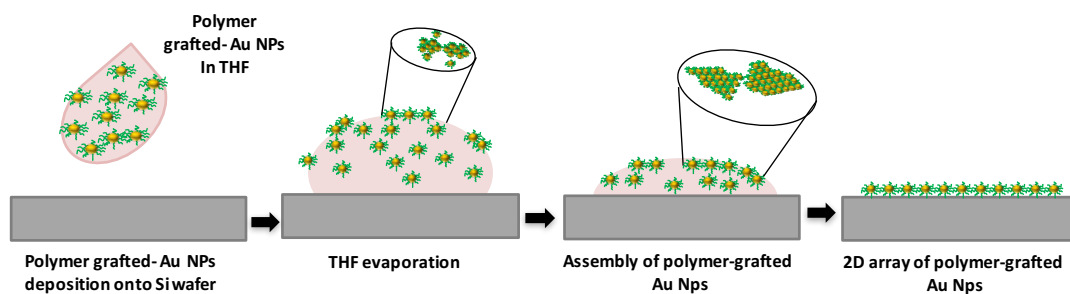
A.8. Reaction temperature, incubation time, and quantities of H_{AuCl}₄ and AA for the shape transformation of Au cuboctahedral seeds into truncated octahedrons with <110> orientation.

Polyhedral Nanocrystal	10 mM H _{AuCl} ₄	100 mM AA	Temperature	Incubation time
	100 μ L	12.5 μ L	40 $^{\circ}$ C	1-2 h
	100 μ L	12.5 μ L	40 $^{\circ}$ C	3-4 h
	200 μ L	25 μ L	60 $^{\circ}$ C	5 h
	200 μ L	25 μ L	60 $^{\circ}$ C	8 h

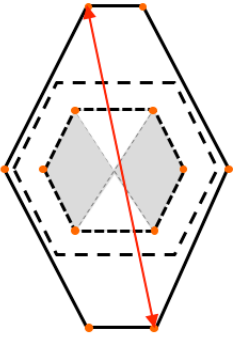
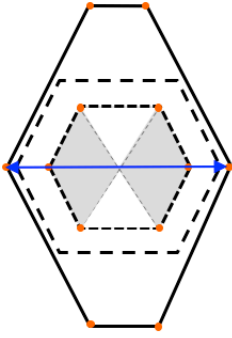
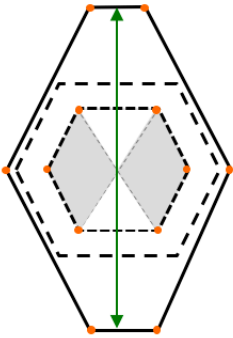
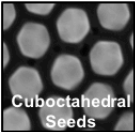

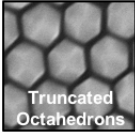

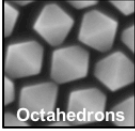
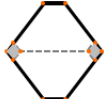
A.9. Reaction temperature, incubation time, and quantities of H_{AuCl}₄ and AA for shape transformation of truncated cubic seeds into cuboctahedrons, truncated octahedrons, and octahedrons with <100> orientation.

Polyhedral Nanocrystal	10 mM HAuCl ₄	100 mM AA	Temperature	Incubation time
	100 μ L	12.5 μ L	40 $^{\circ}$ C	5 h
	200 μ L	25 μ L	40 $^{\circ}$ C	8-10 h

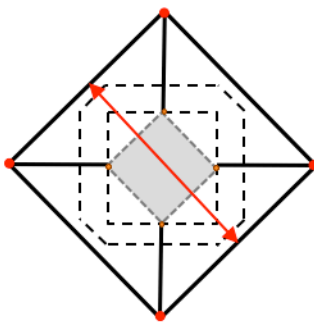
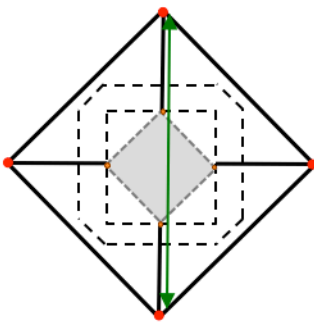
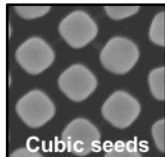
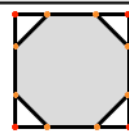
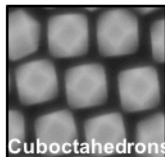
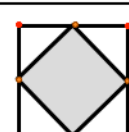

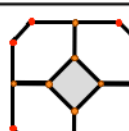
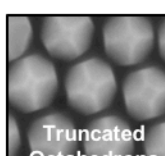
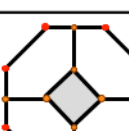
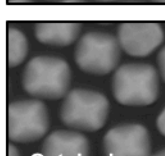

A.10. Reaction temperature, incubation time, and quantities of HAuCl₄ and AA for growth of Au octahedral seeds with <111> orientation.



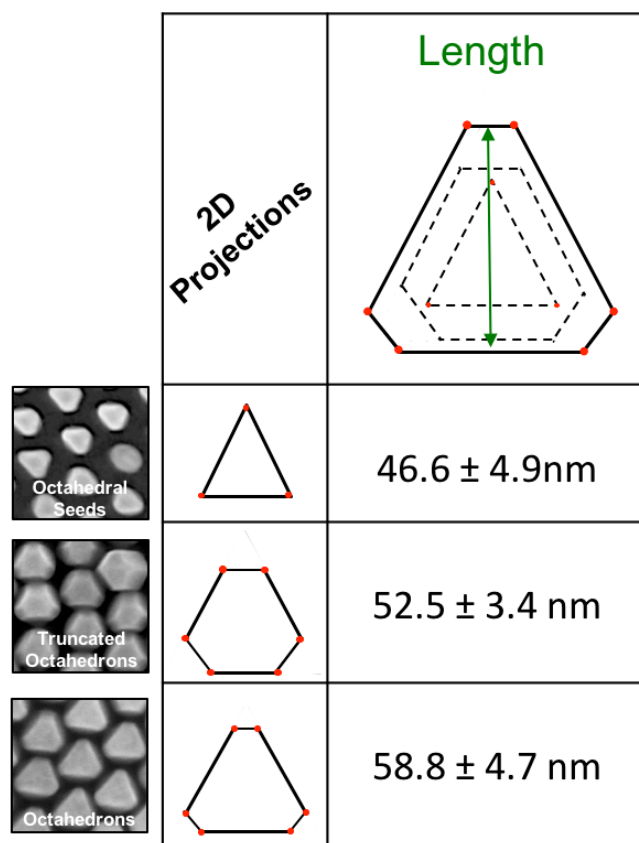
A.11. Schematics illustrating drop casting method to fabricate 2D array of shaped Au NPs seeds.

2D Projections		Diagonal	Width	Length
				
 Cuboctahedral Seeds		$73.8 \pm 3.9 \text{ nm}$	$76.7 \pm 3.9 \text{ nm}$	$68.6 \pm 2.9 \text{ nm}$
 Truncated Octahedrons		$83.7 \pm 5.6 \text{ nm}$	$83.7 \pm 5.3 \text{ nm}$	$78.8 \pm 5.12 \text{ nm}$
 Octahedrons		$92.1 \pm 4.2 \text{ nm}$	$80.8 \pm 4.9 \text{ nm}$	$90.6 \pm 5.0 \text{ nm}$

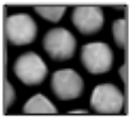
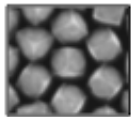
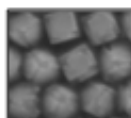
A.12. Schematic illustration and analysis of the diagonal distance, width and length of the Au NCs in the course of shape evolution from Au cuboctahedrons to truncated octahedrons, and finally to octahedrons within arrays.

	2D Projections	Diagonal	Length
			
 Cubic seeds		$71.5 \pm 3.7 \text{ nm}$	$55.0 \pm 5.8 \text{ nm}$
 Cuboctahedrons		$77.8 \pm 5.7 \text{ nm}$	$60.9 \pm 3.8 \text{ nm}$
 Truncated Octahedrons		$82.5 \pm 3.0 \text{ nm}$	$72.7 \pm 2.9 \text{ nm}$
 Truncated Octahedrons		$83.5 \pm 5.0 \text{ nm}$	$77.1 \pm 3.9 \text{ nm}$
 Octahedrons		$83.0 \pm 3.2 \text{ nm}$	$90.2 \pm 4.3 \text{ nm}$

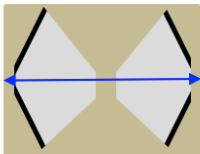
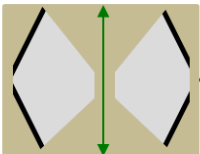
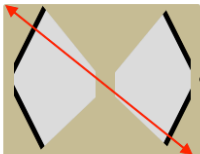


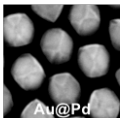

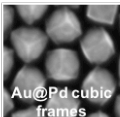

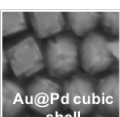

A.13. Schematic illustration and analysis of the diagonal distance and length of the NCs in the course of shape evolution from Au truncated cubes to cuboctahedrons, to truncated octahedrons, and finally to octahedrons within arrays.



A.14. Schematic illustration and analysis of NC length in the course of Au deposition on Au seed octahedrons within arrays.

Polyhedral Nanocrystal	10 mM H ₂ PdCl ₄	100 mM AA	Temperature	Incubation time
	100 μL	50 μL	30 °C	8 h
	200 μL	100 μL	30 °C	12 h
	1000 μL	500 μL	30 °C	12 h

A.15. Reaction temperature, incubation time, and quantities of H₂PdCl₄ and AA for shape transformation of Au cuboctahedral seeds into Au@Pd cubic polyhedrons with <100> orientation.

		Width	Length	Diagonal
	2D Projections			
 Cuboctahedral Seeds		$76.7 \pm 3.9 \text{ nm}$	$68.6 \pm 2.9 \text{ nm}$	$73.8 \pm 3.9 \text{ nm}$
 Au@Pd		$79.5 \pm 4.1 \text{ nm}$	$68.3 \pm 4.2 \text{ nm}$	$79.2 \pm 4.6 \text{ nm}$
 Au@Pd cubic frames		$76.5 \pm 3.4 \text{ nm}$	$65.6 \pm 3.0 \text{ nm}$	$82.0 \pm 3.0 \text{ nm}$
 Au@Pd cubic shell		$70.1 \pm 5.1 \text{ nm}$	$70.1 \pm 5.08 \text{ nm}$	$95.3 \pm 6.3 \text{ nm}$

A.16 . Schematic illustration and analysis of the diagonal distance and length of the NCs in the course of shape evolution from Au cuboctahedrons to Au@Pd core-cubic frame, and finally to core-cubic shell within arrays.

Bibliography

- (1) Noguez, C., *The Journal of Physical Chemistry C* **2007**, *111* (10), 3806-3819.
- (2) Xia, Y.; Xiong, Y.; Lim, B.; Skrabalak, S. E., *Angew. Chem., Int. Ed.* **2009**, *48* (1), 60-103.
- (3) Nie, Z.; Petukhova, A.; Kumacheva, E., *Nat. Nano* **2010**, *5* (1), 15-25.
- (4) Rycenga, M.; Cobley, C. M.; Zeng, J.; Li, W.; Moran, C. H.; Zhang, Q.; Qin, D.; Xia, Y., *Chem. Rev.* **2011**, *111* (6), 3669-3712.
- (5) Hu, M.; Chen, J.; Li, Z.-Y.; Au, L.; Hartland, G. V.; Li, X.; Marquez, M.; Xia, Y., *Chem. Soc. Rev.* **2006**, *35* (11), 1084-1094.
- (6) Willets, K. A.; Duyne, R. P. V., *Annu. Rev. Phys. Chem.* **2007**, *58* (1), 267-297.
- (7) Li, Q.; Wang, F.; Bai, Y.; Xu, L.; Yang, Y.; Yan, L.; Hu, S.; Zhang, B.; Dai, S.; Tan, Z. a., *Organic Electronics* **2017**, *43*, 33-40.
- (8) Ng, A.; Yiu, W. K.; Foo, Y.; Shen, Q.; Bejaoui, A.; Zhao, Y.; Gokkaya, H. C.; Djurišić, A. B.; Zapfen, J. A.; Chan, W. K.; Surya, C., *ACS Appl. Mater. Interfaces* **2014**, *6* (23), 20676-20684.
- (9) Rodal-Cedeira, S.; Montes-García, V.; Polavarapu, L.; Solís, D. M.; Heidari, H.; La Porta, A.; Angiola, M.; Martucci, A.; Taboada, J. M.; Obelleiro, F.; Bals, S.; Pérez-Juste, J.; Pastoriza-Santos, I., *Chem. Mater.* **2016**, *28* (24), 9169-9180.
- (10) Li, X.; Zhu, J.; Wei, B., *Chem. Soc. Rev.* **2016**, *45* (11), 3145-3187.
- (11) Lal, S.; Link, S.; Halas, N. J., *Nat. Photon.* **2007**, *1* (11), 641-648.
- (12) Yang, A.; Hryn, A. J.; Bourgeois, M. R.; Lee, W.-K.; Hu, J.; Schatz, G. C.; Odom, T. W., *Proc. Natl. Acad. Sci.* **2016**, *113* (50), 14201-14206.
- (13) Liu, Y.; He, J.; Yang, K.; Yi, C.; Liu, Y.; Nie, L.; Khashab, N. M.; Chen, X.; Nie, Z., *Angew. Chem.* **2015**, *127* (52), 16035-16038.
- (14) Thakor, A. S.; Jokerst, J.; Zavaleta, C.; Massoud, T. F.; Gambhir, S. S., *Nano Lett.* **2011**, *11* (10), 4029-4036.
- (15) Gobin, A. M.; Lee, M. H.; Halas, N. J.; James, W. D.; Drezek, R. A.; West, J. L., *Nano Lett.* **2007**, *7* (7), 1929-1934.
- (16) Spinelli, P.; Hebbink, M.; de Waele, R.; Black, L.; Lenzmann, F.; Polman, A., *Nano Lett.* **2011**, *11* (4), 1760-1765.
- (17) Atwater, H. A.; Polman, A., *Nat. Mater.* **2010**, *9* (3), 205-213.
- (18) Stuart, H. R.; Hall, D. G., *Appl. Phys. Lett.* **1996**, *69* (16), 2327-2329.
- (19) Stuart, H. R.; Hall, D. G., *Appl. Phys. Lett.* **1998**, *73* (26), 3815-3817.
- (20) Lozano, G.; Rodriguez, S. R. K.; Verschuuren, M. A.; Gomez Rivas, J., *Light Sci Appl.* **2016**, *5*, e16080.
- (21) Sankar, M.; Dimitratos, N.; Miedziak, P. J.; Wells, P. P.; Kiely, C. J.; Hutchings, G. J., *Chem. Soc. Rev.* **2012**, *41* (24), 8099-8139.
- (22) Niu, W.; Zhang, L.; Xu, G., *ACS Nano* **2010**, *4* (4), 1987-1996.
- (23) Tao, A. R.; Habas, S.; Yang, P., *Small* **2008**, *4* (3), 310-325.
- (24) Bratlie, K. M.; Lee, H.; Komvopoulos, K.; Yang, P.; Somorjai, G. A., *Nano Lett.* **2007**, *7* (10), 3097-3101.
- (25) Wu, J.; Qi, L.; You, H.; Gross, A.; Li, J.; Yang, H., *J. Am. Chem. Soc.* **2012**, *134* (29), 11880-11883.

- (26) Personick, M. L.; Langille, M. R.; Zhang, J.; Wu, J.; Li, S.; Mirkin, C. A., *Small* **2013**, 9 (11), 1947-1953.
- (27) Xia, Y.; Xia, X.; Peng, H.-C., *J. Am. Chem. Soc.* **2015**, 137 (25), 7947-7966.
- (28) Mullin, J. W., *Crystallization*. Butterworths: London, 1961.
- (29) Sunagawa, I., *Crystals : growth, morphology, and perfection*. Cambridge University Press: Cambridge :, 2005.
- (30) International Conference on Crystal Growth Cooperstown, N. Y.; Doremus, R. H., *Growth and perfection of crystals; proceedings*. Wiley: New York, 1958.
- (31) Deeb, C.; Zhou, X.; Miller, R.; Gray, S. K.; Marguet, S.; Plain, J.; Wiederrecht, G. P.; Bachelot, R., *The Journal of Physical Chemistry C* **2012**, 116 (46), 24734-24740.
- (32) Chen, H.-Y.; He, C.-L.; Wang, C.-Y.; Lin, M.-H.; Mitsui, D.; Eguchi, M.; Teranishi, T.; Gwo, S., *ACS Nano* **2011**, 5 (10), 8223-8229.
- (33) Lee, D.; Yoon, S., *The Journal of Physical Chemistry C* **2015**, 119 (14), 7873-7882.
- (34) Sivapalan, S. T.; DeVetter, B. M.; Yang, T. K.; Schulmerich, M. V.; Bhargava, R.; Murphy, C. J., *The Journal of Physical Chemistry C* **2013**, 117 (20), 10677-10682.
- (35) Su, D.; Dou, S.; Wang, G., *NPG Asia Mater* **2015**, 7, e155.
- (36) Jana, N. R.; Gearheart, L.; Murphy, C. J., *J. Phys. Chem. B* **2001**, 105 (19), 4065-4067.
- (37) Murphy, C. J.; Sau, T. K.; Gole, A. M.; Orendorff, C. J.; Gao, J.; Gou, L.; Hunyadi, S. E.; Li, T., *J. Phys. Chem. B* **2005**, 109 (29), 13857-13870.
- (38) Jana, N. R.; Gearheart, L.; Murphy, C. J., *Adv. Mater.* **2001**, 13 (18), 1389-1393.
- (39) Xia, Y.; Gilroy, K. D.; Peng, H.-C.; Xia, X., *Angew. Chem., Int. Ed.* **2017**, 56 (1), 60-95.
- (40) Nikoobakht, B.; El-Sayed, M. A., *Chem. Mater.* **2003**, 15 (10), 1957-1962.
- (41) Zhang, J.; Xi, C.; Feng, C.; Xia, H.; Wang, D.; Tao, X., *Langmuir* **2014**, 30 (9), 2480-2489.
- (42) Zijlstra, P.; Bullen, C.; Chon, J. W. M.; Gu, M., *J. Phys. Chem. B* **2006**, 110 (39), 19315-19318.
- (43) LaMer, V. K.; Dinegar, R. H., *J. Am. Chem. Soc.* **1950**, 72 (11), 4847-4854.
- (44) Polte, J., *CrystEngComm* **2015**, 17 (36), 6809-6830.
- (45) Zhu, T.; Vasilev, K.; Kreiter, M.; Mittler, S.; Knoll, W., *Langmuir* **2003**, 19 (22), 9518-9525.
- (46) Kumar, S.; Gandhi, K. S.; Kumar, R., *Ind. Eng. Chem. Res.* **2007**, 46 (10), 3128-3136.
- (47) Su, Y.-H.; Ke, Y.-F.; Cai, S.-L.; Yao, Q.-Y., *Light Sci Appl* **2012**, 1, e14.
- (48) Tseng, W.-H.; Chiu, C.-Y.; Chou, S.-W.; Chen, H.-C.; Tsai, M.-L.; Kuo, Y.-C.; Lien, D.-H.; Tsao, Y.-C.; Huang, K.-Y.; Yeh, C.-T.; He, J.-H.; Wu, C.-I.; Huang, M. H.; Chou, P.-T., *The Journal of Physical Chemistry C* **2015**, 119 (14), 7554-7564.
- (49) Lee, Y. H.; Chen, H.; Xu, Q.-H.; Wang, J., *The Journal of Physical Chemistry C* **2011**, 115 (16), 7997-8004.

- (50) Gilroy, K. D.; Ruditskiy, A.; Peng, H.-C.; Qin, D.; Xia, Y., *Chem. Rev.* **2016**, *116* (18), 10414-10472.
- (51) DeSantis, C. J.; Weiner, R. G.; Radmilovic, A.; Bower, M. M.; Skrabalak, S. E., *The Journal of Physical Chemistry Letters* **2013**, *4* (18), 3072-3082.
- (52) Gu, J.; Zhang, Y.-W.; Tao, F., *Chem. Soc. Rev.* **2012**, *41* (24), 8050-8065.
- (53) DeSantis, C. J.; Skrabalak, S. E., *Chem. Commun.* **2014**, *50* (40), 5367-5369.
- (54) Wen, M.; Mori, K.; Kuwahara, Y.; Yamashita, H., *ACS Energy Letters* **2017**, *2* (1), 1-7.
- (55) Scarabelli, L.; Coronado-Puchau, M.; Giner-Casares, J. J.; Langer, J.; Liz-Marzán, L. M., *ACS Nano* **2014**, *8* (6), 5833-5842.
- (56) Yoo, H.; Jang, M. H., *Nanoscale* **2013**, *5* (15), 6708-6712.
- (57) Usher, A.; McPhail, D. C.; Brugger, J., *Geochim. Cosmochim. Acta* **2009**, *73* (11), 3359-3380.
- (58) Eguchi, M.; Mitsui, D.; Wu, H.-L.; Sato, R.; Teranishi, T., *Langmuir* **2012**, *28* (24), 9021-9026.
- (59) Li, C.; Shuford, K. L.; Chen, M.; Lee, E. J.; Cho, S. O., *ACS Nano* **2008**, *2* (9), 1760-1769.
- (60) Li, C.; Shuford, K. L.; Park, Q. H.; Cai, W.; Li, Y.; Lee, E. J.; Cho, S. O., *Angew. Chem.* **2007**, *119* (18), 3328-3332.
- (61) Zijlstra, P.; Chon, J. W. M.; Gu, M., *Nature* **2009**, *459* (7245), 410-413.
- (62) Nathan, C. L.; Prashant, N.; Kevin, M. M.; David, J. N.; Sang-Hyun, O., *Rep. Prog. Phys.* **2012**, *75* (3), 036501.
- (63) Pellarin, M.; Ramade, J.; Rye, J. M.; Bonnet, C.; Broyer, M.; Lebeault, M.-A.; Lermé, J.; Marguet, S.; Navarro, J. R. G.; Cottancin, E., *ACS Nano* **2016**, *10* (12), 11266-11279.
- (64) Lyvers, D. P.; Moon, J.-M.; Kildishev, A. V.; Shalae, V. M.; Wei, A., *ACS Nano* **2008**, *2* (12), 2569-2576.
- (65) Ozin, G. A.; Arsenault, A. C.; Cademartiri, L.; Royal Society of, C., *Nanochemistry : a chemical approach to nanomaterials*. 2nd ed. ed.; Royal Society of Chemistry: Cambridge :, 2009.
- (66) von Maltzahn, G.; Park, J.-H.; Agrawal, A.; Bandaru, N. K.; Das, S. K.; Sailor, M. J.; Bhatia, S. N., *Cancer Res.* **2009**, *69* (9), 3892-3900.
- (67) Song, J.; Zhou, J.; Duan, H., *J. Am. Chem. Soc.* **2012**, *134* (32), 13458-13469.
- (68) Mukherjee, P.; Bhattacharya, R.; Wang, P.; Wang, L.; Basu, S.; Nagy, J. A.; Atala, A.; Mukhopadhyay, D.; Soker, S., *Clin. Cancer Res.* **2005**, *11* (9), 3530-3534.
- (69) Lin, J.; Wang, S.; Huang, P.; Wang, Z.; Chen, S.; Niu, G.; Li, W.; He, J.; Cui, D.; Lu, G.; Chen, X.; Nie, Z., *ACS Nano* **2013**, *7* (6), 5320-5329.
- (70) Mahdy, M. R. C.; Zhang, T.; Danesh, M.; Ding, W., *Scientific Reports* **2017**, *7* (1), 6938.
- (71) Anker, J. N.; Hall, W. P.; Lyandres, O.; Shah, N. C.; Zhao, J.; Van Duyne, R. P., *Nat. Mater.* **2008**, *7* (6), 442-453.
- (72) Martín, A.; Schopf, C.; Pescaglini, A.; Wang, J. J.; Iacopino, D., *Langmuir* **2014**, *30* (34), 10206-10212.
- (73) Sheng Yang, Y.; Liao, L. D.; Thakor, N. V.; Tan, M. C., *J. Biomed. Nanotechnol.* **2010**, *10* (10), 2641-2676.

- (74) Kim, S.; Jin, J.; Kim, Y.-J.; Park, I.-Y.; Kim, Y.; Kim, S.-W., *Nature* **2008**, 453 (7196), 757-760.
- (75) Lee, J.; Mubeen, S.; Ji, X.; Stucky, G. D.; Moskovits, M., *Nano Lett.* **2012**, 12 (9), 5014-5019.
- (76) Liu, M.; Ji, Z.; Shang, L. Top-Down Fabrication of Nanostructures. In *Nanotechnology: Nanostructured Surfaces*; Chi, L., Ed.; WILEY-VCH: Weinheim, Germany, 2010; Vol. 8, pp 3-47.
- (77) Xia, Y.; Rogers, J. A.; Paul, K. E.; Whitesides, G. M., *Chem. Rev.* **1999**, 99 (7), 1823-1848.
- (78) Xie, Q.; Hong, M. H.; Tan, H. L.; Chen, G. X.; Shi, L. P.; Chong, T. C., *J. Alloys Compd.* **2008**, 449 (1), 261-264.
- (79) Tseng, A. A.; Kuan, C.; Chen, C. D.; Ma, K. J., *IEEE Transactions on Electronics Packaging Manufacturing* **2003**, 26 (2), 141-149.
- (80) Leggett, G. J., *ACS Nano* **2011**, 5 (3), 1575-1579.
- (81) and, Y. X.; Whitesides, G. M., *Annual Review of Materials Science* **1998**, 28 (1), 153-184.
- (82) Li, Z.; Gu, Y.; Wang, L.; Ge, H.; Wu, W.; Xia, Q.; Yuan, C.; Chen, Y.; Cui, B.; Williams, R. S., *Nano Lett.* **2009**, 9 (6), 2306-2310.
- (83) Vieu, C.; Carcenac, F.; Pepin, A.; Chen, Y.; Mejias, M.; Lebib, A.; Manin-Ferlazzo, L.; Couraud, L.; Launois, H., *Applied Surface Science* **2000**, 164, 111-117.
- (84) Odom, T. W.; Love, J. C.; Wolfe, D. B.; Paul, K. E.; Whitesides, G. M., *Langmuir* **2002**, 18 (13), 5314-5320.
- (85) Fredriksson, H.; Alaverdyan, Y.; Dmitriev, A.; Langhammer, C.; Sutherland, D. S.; Zäch, M.; Kasemo, B., *Adv. Mater.* **2007**, 19 (23), 4297-4302.
- (86) Yang, S.-M.; Jang, S. G.; Choi, D.-G.; Kim, S.; Yu, H. K., *Small* **2006**, 2 (4), 458-475.
- (87) Fleck, N. A.; McMeeking, R. M.; Kraus, T., *Langmuir* **2015**, 31 (51), 13655-13663.
- (88) Ng, K. C.; Udagedara, I. B.; Rukhlenko, I. D.; Chen, Y.; Tang, Y.; Premaratne, M.; Cheng, W., *ACS Nano* **2012**, 6 (1), 925-934.
- (89) Wen, T.; Majetich, S. A., *ACS Nano* **2011**, 5 (11), 8868-8876.
- (90) Nie, H.-L.; Dou, X.; Tang, Z.; Jang, H. D.; Huang, J., *J. Am. Chem. Soc.* **2015**, 137 (33), 10683-10688.
- (91) Fendler, J. H., *Chem. Mater.* **1996**, 8 (8), 1616-1624.
- (92) Ho, C.-C.; Chen, P.-Y.; Lin, K.-H.; Juan, W.-T.; Lee, W.-L., *ACS Appl. Mater. Interfaces* **2011**, 3 (2), 204-208.
- (93) Bigioni, T. P.; Lin, X.-M.; Nguyen, T. T.; Corwin, E. I.; Witten, T. A.; Jaeger, H. M., *Nat. Mater.* **2006**, 5 (4), 265-270.
- (94) Rao, S.; Si, K. J.; Yap, L. W.; Xiang, Y.; Cheng, W., *ACS Nano* **2015**, 9 (11), 11218-11224.
- (95) Bhunia, S. K.; Zeiri, L.; Manna, J.; Nandi, S.; Jelinek, R., *ACS Appl. Mater. Interfaces* **2016**, 8 (38), 25637-25643.
- (96) Zheng, Y.; Thai, T.; Reineck, P.; Qiu, L.; Guo, Y.; Bach, U., *Adv. Funct. Mater.* **2013**, 23 (12), 1519-1526.

- (97) Kinkhabwala, A.; Yu, Z.; Fan, S.; Avlasevich, Y.; Mullen, K.; Moerner, W. E., *Nat. Photon.* **2009**, *3* (11), 654-657.
- (98) Liu, Y.; Li, Y.; He, J.; Duelge, K. J.; Lu, Z.; Nie, Z., *J. Am. Chem. Soc.* **2014**, *136* (6), 2602-2610.
- (99) Wadams, R. C.; Fabris, L.; Vaia, R. A.; Park, K., *Chem. Mater.* **2013**, *25* (23), 4772-4780.
- (100) Murphy, C. J.; Thompson, L. B.; Chernak, D. J.; Yang, J. A.; Sivapalan, S. T.; Boulos, S. P.; Huang, J.; Alkilany, A. M.; Sisco, P. N., *Curr. Opin. Colloid Interface Sci.* **2011**, *16* (2), 128-134.
- (101) Scarabelli, L.; Grzelczak, M.; Liz-Marzán, L. M., *Chem. Mater.* **2013**, *25* (21), 4232-4238.
- (102) Ye, X.; Zheng, C.; Chen, J.; Gao, Y.; Murray, C. B., *Nano Lett.* **2013**, *13* (2), 765-771.
- (103) Personick, M. L.; Mirkin, C. A., *J. Am. Chem. Soc.* **2013**, *135* (49), 18238-18247.
- (104) Sau, T. K.; Murphy, C. J., *J. Am. Chem. Soc.* **2004**, *126* (28), 8648-8649.
- (105) Wu, H.-L.; Kuo, C.-H.; Huang, M. H., *Langmuir* **2010**, *26* (14), 12307-12313.
- (106) Sohn, K.; Kim, F.; Pradel, K. C.; Wu, J.; Peng, Y.; Zhou, F.; Huang, J., *ACS Nano* **2009**, *3* (8), 2191-2198.
- (107) Smith, D. K.; Korgel, B. A., *Langmuir* **2008**, *24* (3), 644-649.
- (108) Smith, D. K.; Miller, N. R.; Korgel, B. A., *Langmuir* **2009**, *25* (16), 9518-9524.
- (109) Kim, M. P.; Hyung; Han, Sang; Park, Jimin; Yun, Wan, *Bull. Korean Chem. Soc.* **2013**, *34* (8), 2243-2244.
- (110) Sepulveda, L.; Cortes, J., *The Journal of Physical Chemistry* **1985**, *89* (24), 5322-5324.
- (111) Placido, T.; Comparelli, R.; Giannici, F.; Cozzoli, P. D.; Capitani, G.; Striccoli, M.; Agostiano, A.; Curri, M. L., *Chem. Mater.* **2009**, *21* (18), 4192-4202.
- (112) Edgar, J. A.; McDonagh, A. M.; Cortie, M. B., *ACS Nano* **2012**, *6* (2), 1116-1125.
- (113) Chen, H. M.; Liu, R.-S.; Asakura, K.; Jang, L.-Y.; Lee, J.-F., *The Journal of Physical Chemistry C* **2007**, *111* (50), 18550-18557.
- (114) Miessler, G. L.; Tarr, D. A., *Inorganic chemistry*. 3rd ed. ed.; Pearson Education: Upper Saddle River, N.J. ;, 2004.
- (115) Schmidbaur, H., *Gold : progress in chemistry, biochemistry, and technology*. Wiley: Chichester ;, 1999.
- (116) Puddephatt, R. J., *The chemistry of gold*. Elsevier Scientific Pub. Co. ; Distributors for the U.S. and Canada, Elsevier/North-Holland: Amsterdam ; New York ;, 1978.
- (117) Ünaleroğlu, C.; Mert, Y.; Zümreoğlu-Karan, B., *Synth. React. Inorg. Met.-Org. Chem.* **2001**, *31* (9), 1531-1543.
- (118) Ogata, Y. Y.; Kosugi, Y., *Tetrahedron*. *26* (20), 4711-4716.
- (119) Zümreoğlu-Karan, B., *Coord. Chem. Rev.* **2006**, *250* (17), 2295-2307.

- (120) Martell, A. E. Chelates of Ascorbic Acid. In *Ascorbic Acid: Chemistry, Metabolism, and Uses*; AMERICAN CHEMICAL SOCIETY: 1982; Vol. 200, pp 153-178.
- (121) Yuge, H.; Miyamoto, T. K., *Inorg. Chim. Acta* **2002**, 329 (1), 66-70.
- (122) Hollis, L. S.; Stern, E. W.; Amundsen, A. R.; Miller, A. V.; Doran, S. L., *J. Am. Chem. Soc.* **1987**, 109 (12), 3596-3602.
- (123) Arendse, M. J.; Anderson, G. K.; Rath, N. P., *Inorg. Chem.* **1999**, 38 (25), 5864-5869.
- (124) Khan, M. M. T.; Shukla, R. S.; Rao, A. P., *Inorg. Chem.* **1989**, 28 (3), 452-458.
- (125) Cotton, A.; Wilkinson, G.; Murillo, C.; Bochmann, M., *Advanced Inorganic Chemistry* 6th ed.; John Wiley & Sons, Inc.: New York 1999; p 1355.
- (126) Huheey, J.; Keiter, E.; Keiter, R., *Inorganic Chemistry: Principles of Structure and Reactivity* 4th ed.; Harper Collins College Publishers New York, 1993; p 964.
- (127) Zhong, Z.; Patskovskyy, S.; Bouvrette, P.; Luong, J. H. T.; Gedanken, A., *J. Phys. Chem. B* **2004**, 108 (13), 4046-4052.
- (128) Acar, H.; Genc, R.; Urel, M.; Erkal, T. S.; Dana, A.; Guler, M. O., *Langmuir* **2012**, 28 (47), 16347-16354.
- (129) Huang, C.-C.; Yang, Z.; Chang, H.-T., *Langmuir* **2004**, 20 (15), 6089-6092.
- (130) Rozin, M. J.; Rosen, D. A.; Dill, T. J.; Tao, A. R., *Nat. Commun.* **2015**, 6, 7325.
- (131) Liu, Y.; Cheng, R.; Liao, L.; Zhou, H.; Bai, J.; Liu, G.; Liu, L.; Huang, Y.; Duan, X., *Nat. Commun.* **2011**, 2, 579.
- (132) Toma, M.; Loget, G.; Corn, R. M., *Nano Letters* **2013**, 13 (12), 6164-6169.
- (133) Terris, B. D., *J. Magn. Magn. Mater.* **2009**, 321 (6), 512-517.
- (134) Ma, Z.; Dai, S., *Nano Res.* **2011**, 4 (1), 3-32.
- (135) Contreras, A. M.; Grunes, J.; Yan, X.-M.; Liddle, A.; Somorjai, G. A., *Top. Catal.* **2006**, 39 (3), 123-129.
- (136) Anker, J. N.; Hall, W. P.; Lyandres, O.; Shah, N. C.; Zhao, J.; Van Duyne, R. P., *Nature Materials* **2008**, 7 (6), 442-453.
- (137) Lee, W.; Lee, S. Y.; Briber, R. M.; Rabin, O., *Adv. Funct. Mater.* **2011**, 21 (18), 3424-3429.
- (138) Lal, S.; Link, S.; Halas, N. J., *Nature Photonics* **2007**, 1 (11), 641-648.
- (139) Schuller, J. A.; Barnard, E. S.; Cai, W.; Jun, Y. C.; White, J. S.; Brongersma, M. L., *Nat. Mater.* **2010**, 9 (3), 193-204.
- (140) Huang, L.; Chen, X.; Mühlenbernd, H.; Li, G.; Bai, B.; Tan, Q.; Jin, G.; Zentgraf, T.; Zhang, S., *Nano letters* **2012**, 12 (11), 5750-5755.
- (141) Yu, N.; Genevet, P.; Kats, M. A.; Aieta, F.; Tetienne, J.-P.; Capasso, F.; Gaburro, Z., *science* **2011**, 334 (6054), 333-337.
- (142) Gong, J.; Li, G.; Tang, Z., *Nano Today* **2012**, 7 (6), 564-585.
- (143) Nepal, D.; Onses, M. S.; Park, K.; Jespersen, M.; Thode, C. J.; Nealey, P. F.; Vaia, R. A., *ACS Nano* **2012**, 6 (6), 5693-5701.
- (144) Petukhova, A.; Greener, J.; Liu, K.; Nykypanchuk, D.; Nicolaÿ, R.; Matyjaszewski, K.; Kumacheva, E., *Small* **2012**, 8 (5), 731-737.

- (145) Huang, J.; Kim, F.; Tao, A. R.; Connor, S.; Yang, P., *Nature materials* **2005**, 4 (12), 896.
- (146) Gao, B.; Arya, G.; Tao, A. R., *Nature Nanotechnology* **2012**, 7 (7), 433-437.
- (147) Peng, B.; Li, G.; Li, D.; Dodson, S.; Zhang, Q.; Zhang, J.; Lee, Y. H.; Demir, H. V.; Yi Ling, X.; Xiong, Q., *ACS Nano* **2013**, 7 (7), 5993-6000.
- (148) Hajfathalian, M.; Gilroy, K. D.; Hughes, R. A.; Neretina, S., *Small* **2016**, 12 (25), 3444-3452.
- (149) Gilroy, K. D.; Hughes, R. A.; Neretina, S., *J. Am. Chem. Soc.* **2014**, 136 (43), 15337-15345.
- (150) Sajanlal, P. R.; Sreeprasad, T. S.; Samal, A. K.; Pradeep, T., *Nano Reviews* **2011**, 2, 10.3402/nano.v3402i3400.5883.
- (151) Wu, L. Y.; Ross, B. M.; Hong, S.; Lee, L. P., *Small* **2010**, 6 (4), 503-507.
- (152) Hsieh, H.-Y.; Xiao, J.-L.; Lee, C.-H.; Huang, T.-W.; Yang, C.-S.; Wang, P.-C.; Tseng, F.-G., *The Journal of Physical Chemistry C* **2011**, 115 (33), 16258-16267.
- (153) Lu, C.-L.; Prasad, K. S.; Wu, H.-L.; Ho, J.-a. A.; Huang, M. H., *J. Am. Chem. Soc.* **2010**, 132 (41), 14546-14553.
- (154) Wang, F.; Li, C.; Chen, H.; Jiang, R.; Sun, L.-D.; Li, Q.; Wang, J.; Yu, J. C.; Yan, C.-H., *J. Am. Chem. Soc.* **2013**, 135 (15), 5588-5601.
- (155) Wang, F.; Sun, L.-D.; Feng, W.; Chen, H.; Yeung, M. H.; Wang, J.; Yan, C.-H., *Small* **2010**, 6 (22), 2566-2575.
- (156) Chiu, C.-Y.; Huang, M. H., *Angewandte Chemie International Edition* **2013**, 52 (48), 12709-12713.
- (157) Lim, B.; Kobayashi, H.; Yu, T.; Wang, J.; Kim, M. J.; Li, Z.-Y.; Rycenga, M.; Xia, Y., *J. Am. Chem. Soc.* **2010**, 132 (8), 2506-2507.
- (158) Liu, C. H.; Hong, M. H.; Cheung, H. W.; Zhang, F.; Huang, Z. Q.; Tan, L. S.; Hor, T. S. A., *Opt. Express* **2008**, 16 (14), 10701-10709.
- (159) Laskar, M.; Zhong, X.; Li, Z.-Y.; Skrabalak, S. E., *ChemSusChem* **2013**, 6 (10), 1959-1965.
- (160) Peng, H.-C.; Xie, S.; Park, J.; Xia, X.; Xia, Y., *J. Am. Chem. Soc.* **2013**, 135 (10), 3780-3783.